UNIVERSITÀ DEGLI STUDI DI MILANO

SCUOLA DI DOTTORATO
FISICA, ASTROFISICA E FISICA APPLICATA

DIPARTIMENTO DI FISICA

CORSO DI DOTTORATO DI RICERCA IN
FISICA, ASTROFISICA E FISICA APPLICATA
CICLO XXIII

MISSING TRANSVERSE ENERGY MEASUREMENT IN ATLAS DETECTOR: FIRST LHC DATA RESULTS AND IMPORTANCE FOR PHYSICS STUDY

Settore Scientifico Disciplinare FIS/04

Tesi di Dottorato di:
Caterina Pizio
Matr. R07880

Supervisore: Dott. Donatella Cavalli
Coordinatore: Prof. Marco Bersanelli

Anno Accademico 2009-2010

Abstract

The Large Hadron Collider (LHC) at CERN started its operation at the end of November 2009, first at a centre-of-mass energy of 900 GeV, then, since March 2010, at 7 TeV. During this period the ATLAS experiment has collected a large number of proton-proton collision events, resulting up to now in an integrated luminosity of about 45 pb^{-1}.

A very good measurement of the missing transverse energy, E_T^{miss}, is essential for many physics studies in ATLAS both for Standard Model channels, as W, Z bosons decaying to τ leptons or top quark decays, and for discovering channels. Events with large E_T^{miss} are expected to be the key signature for new physics such as supersymmetry and extra dimensions. A good E_T^{miss} measurement in terms of linearity and resolution is crucial for the efficient and accurate reconstruction of the Higgs boson mass when the Higgs boson decays to a pair of τ-leptons.

This thesis describes the first measurement of E_T^{miss} in ATLAS with real data.

The performance of the algorithm for E_T^{miss} reconstruction has been widely tested in minimum bias and di-jet events that are not expected to have genuine E_T^{miss}. In ATLAS E_T^{miss} is calculated from the calorimeter cell energies, from reconstructed muons energy and from an estimation of the energy lost in dead materials. Since it is reconstructed from everything seen in the detector, E_T^{miss} is a complex quantity: particles escaping because of the limited coverage of the detector, presence of dead regions and different sources of noise can produce fake E_T^{miss} . A lot of effort has been dedicated to understand well the tails in the E_T^{miss} distribution and to apply selection cuts to remove fake E_T^{miss} signals.

As the ATLAS calorimeters are not compensating, that is the response to hadronic and electromagnetic particles is different, the calibration of the calorimeter cell energies is crucial. With 900 GeV data the E_T^{miss} performance has been studied and it has been found as expected from simulation at the EM scale.With 7 TeV data the E_T^{miss} calibration has been validated. E_T^{miss} performance using different calibrations algorithms has been tested, confirming the good agreement between data and simulation found at the EM scale.

The effect of pileup has also been studied in details.

To complete the E_T^{miss} commissioning the absolute scale determination is needed. This will be possible only when enough statistics of events with genuine E_T^{miss} will be available.

First, with the already available statistics, using the standard ATLAS $W \to l\nu$ selection, the E_T^{miss} scale can be checked from the shape of the W transverse mass distribution that is calculated from the lepton and E_T^{miss} and

has only a few percent of background contamination. This method allows to set the E_T^{miss} scale with a precision of 3% considering only statistical errors and using less than 50 pb^{-1} of data at 7 TeV.

Then $Z \to \tau\tau$ events will be used where a Z boson decays into a couple of τ leptons, then a τ decays into a lepton and neutrinos and the other one into hadrons and a neutrino. It is possible to reconstruct the invariant mass of the two taus using the reconstructed lepton, the hadronic part of the τ (τ-jet) and E_T^{miss} in the so-called *collinear approximation*. From the invariant mass peak position it is possible to determine the E_T^{miss} scale. A detailed study has been done on simulated data to collect a very pure signal sample with low backgorund contamination. With this method the E_T^{miss} scale can be fixed with a precision of 6% with an integrated luminosity of about 100 pb^{-1} at 10 TeV.

The first chapter of this thesis is dedicated to the physics at LHC: the theoretical motivation is briefly described. The importance of a very good E_T^{miss} measurement is shown for the study of many physics channels, with particular attention to the Standard Model $Z \to \tau\tau$ channel, the search for supersymmetry and the discovery channel $A/H \to \tau\tau$ in the Minimal Supersymmetric Standard Model.

The second chapter describes LHC and the ATLAS experiment focusing on the detector commissioning done with the first data at LHC.

In the third chapter I document the results of E_T^{miss} measurement with first ATLAS data. The description of E_T^{miss} calculation in ATLAS is given detailing the different algorithms available, from the most basic to the most refined one. The different E_T^{miss} calibrations are also described. The performance of E_T^{miss} in data is compared to the simulation with careful understanding of the events in tails.

The last chapter describes the preliminary results obtained with ATLAS data to determine the E_T^{miss} scale from $W \to l\nu$ events and also a detailed Monte Carlo based study to set the E_T^{miss} scale from $Z \to \tau\tau$ events that will be used when at least 100 pb^{-1} of data will be available.

Contents

List of Figures

List of Tables

Chapter 1

Physics at the LHC and E_T^{miss} importance

The CERN Large Hadron Collider is the largest hadronic collider in the world. It has a circumference of about 27 km and provides proton-proton collisions at a centre-of-mass energy never reached in the past. Since the end of November 2009 it started to operate first at a centre-of-mass energy of 900 GeV, then in the end of March 2010 it set a record for high-energy collisions reaching a centre-of-mass energy of 7 TeV.

Nevertheless the designed centre-of-mass energy is of 14 TeV and the luminosity $10^{34}\text{cm}^{-2}\text{s}^{-1}$, that will allow searches for new particles to be performed up to masses of ~ 5 TeV.

To define the missing transverse energy, that is the physics event quantity being the core of this dissertation, it is necessary to introduce the proton-proton interaction phenomenology and the hadronic colliders physics theoretical background.

1.1 Phenomenology of proton-proton collision

The total inelastic proton-proton cross-section is about 80 mb at a centre-of-mass energy $\sqrt{s} = 14$ TeV [1]. Therefore, the event rate R, defined as the number of events produced per second by the pp interactions, is expected to be

$$R = \sigma \times L = 80\,\text{mb} \times 10^{34}\text{cm}^{-2}\text{s}^{-1} \simeq 10^{9}/\text{s} \tag{1.1}$$

when running at the nominal luminosity. These events belong to two classes:

- *Minimum bias events*

Most events are due to large distance collisions between the two incoming protons. In this case the momentum transfer of the interaction is small (*soft collisions*) and therefore particle scattering at large angle is suppressed. The particles produced in the final state of such interactions have large longitudinal momentum, but small transverse momentum (p_T) relative to the beam line ($< p_T > \simeq 500$ MeV). Most of the collision energy escapes down the beam pipe. The final states arising from these soft interactions are called minimum bias events [2]. They represent by far the majority of the pp collisions and, although they are not interesting for discovery analyses, they can be used for performance studies (see Chapter 3).

- *Hard scattering events.*

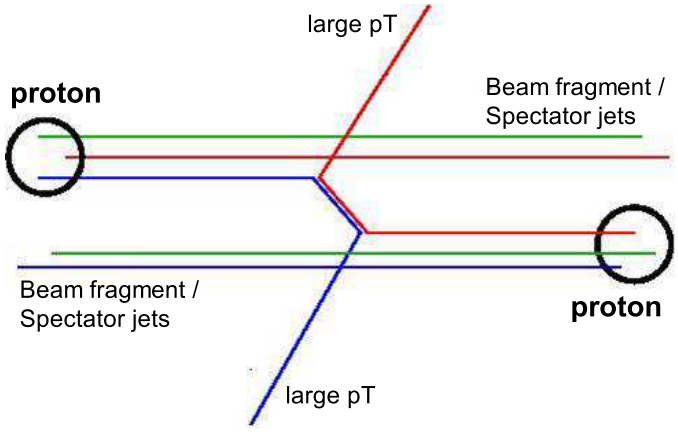

Figure 1.1: *Schematic representation of a high-p_T pp interaction.*

Monochromatic proton beams can be seen as beams of partons (that are quarks and gluons, the constituents of the proton, described in detail in Section 1.2.1) with a wide band of energy, as illustrated in Figure 1.1. Occasionally, head-on collisions occur between two partons of the incoming protons. These are interactions at small distances, and therefore are characterised by large momentum transfers (hard scattering). In this case, particles in the final state can be produced at large angles with respect to the beam line (*high* p_T) and massive particles can be created. These are the interesting physics events, but they are rare compared to the soft interactions. For instance, the production of a W boson through the annihilation of a quark-antiquark pair has a cross-section of 150 nb, i.e. > 100 times smaller than the total inelastic pp cross-section.

In both cases the energy of the interacting quarks and gluons is not

known (only the proton energy is known) and therefore the missing energy in the final state cannot be determined. However, since the transverse momentum (perpendicular to the beam axis) of the incident quarks and gluons is negligible, the total transverse momentum in the initial state is close to zero, and so has to be the total transverse energy in the final state.

But the presence of

- non (or weakly) interacting particles,
- limited acceptance of the detector,
- dead regions and other detector problems
- particles not coming from the primary collision

lead to a *missing* transverse energy (momentum), E_T^{miss}.

1.2 E_T^{miss} and Standard Model channels

It is easy to imagine that, being the most important signature of non interacting particles, E_T^{miss} is a very important event quantity that needs a lot of effort to be evaluated with the highest possible precision. Events with large E_T^{miss} are expected to be the key signature for new physics such as supersymmetry and extra dimensions. A good E_T^{miss} measurement in terms of linearity and resolution is also important for the reconstruction of the top-quark mass from $t\bar{t}$ events with one top quark decaying semi-leptonically. Furthermore, it is crucial for the efficient and accurate reconstruction of the Higgs boson mass when the Higgs boson decays to a pair of τ-leptons. To fully understand how many physics channels need a good measurement of this quantity a brief description of the phenomenology is presented.

1.2.1 Standard Model, a brief overview

The Standard Model is a successful theory incorporating the present understanding of fundamental particles and their interactions. It is based on a spontaneously broken local $SU(3) \otimes SU(2) \otimes U(1)$ gauge theory describing the strong, weak and electromagnetic interactions.

In the Standard Model (SM), two types of fundamental particles are distinguished according to their spin:

- *Fermions with spin* 1/2.

  The fermions are the matter constituents and are grouped further into doublets of leptons and quarks (already introduced as proton constituents in 1.1) listed in Table 1.1. Both lepton and quark doublets exist in three generations with increasing masses.

In the lepton family, electron, muon and τ lepton have electric charge -1, while the neutrinos are neutral. The SM assumes that the neutrino masses are 0.

In the quark family, the u (up), c (charm) and t (top) quarks have electric charge $+\frac{2}{3}e$, while the d (down), (strange) and b (bottom) quarks have charge $-\frac{1}{3}e$. The quarks carry a colour charge that is related to the strong interaction. They can not be found isolated, since they have to form bound states so that the resulting state is *colourless*.

Since the existence of states with more than three quarks is generally not considered to be proven, there are two possible combinations: either a quark is bound with an anti-quark forming a meson or three (anti-)quarks are forming a (anti-)baryon. These two particle types are grouped under the name *hadrons*.

As mentioned above, the particles of the first generation are the lightest ones. Except for the neutrinos the particles of the 2nd and 3rd generations are unstable, thus giving the first generation the privilege to form all ordinary matter.

Fermions	Generation			Charge	Interactions
	I	II	III	(e)	
Quarks	u	c	t	$+\frac{2}{3}$	Strong
					Weak
	d	s	b	$-\frac{1}{3}$	EM
Leptons	ν_e	ν_μ	ν_τ	0	Weak
	e^-	μ^-	τ^-	-1	Weak and EM

Table 1.1: *Elementary fermionic particles in the SM.*

- *Bosons with spin 1.*

  They are the vector bosons of the gauge fields mediating the three fundamental forces: the electromagnetic, the weak and the strong interaction. In more details:

  - The electromagnetic interaction affects all particles of non-zero electric charge. Its associated gauge boson is the photon (γ). The associated charge is the electric charge. The coupling constant is the fine structure constant

$$\alpha_{em}(m_e) = \frac{e^2}{4\pi\epsilon_0\hbar c} = 7.2973525376(50) \times 10^{-3} \tag{1.2}$$

where e is the absolute value of the electron charge, ϵ_0 is the dielectric constant of the vacuum, $\hbar$ is the Planck constant and c is the speed of light in vacuum. The fine structure constant is the best measured parameter in the SM.

– The weak interaction affects all fundamental fermions. It has three associated vector bosons, W^+ , W^-, and Z. The associated charge is the weak charge. The coupling constant is

$$\frac{G_F}{(\hbar c)^3} = 1.16637(1) \times 10^{-5}\,\mathrm{GeV}^{-2} \tag{1.3}$$

– The strong interaction affects only the quarks and is carried by eight gluons (g). The associated charge is called *colour*. At first order in perturbation theory the QCD coupling constant takes the form

$$\alpha_s(\mu^2) = \frac{12\pi}{(33 - 2n_f) \cdot \ln(\frac{\mu^2}{\Lambda^2})} \tag{1.4}$$

where n_f is the number of fermions, μ is the scale of the interaction (usually the squared transferred four-momentum is taken), and Λ is an energy scale parameter, that is measured by experiments to be $\Lambda \sim 250$ MeV. This value corresponds roughly to the scale of the nucleon radius.

Interactions	Bosons	Electric Charge	Mass (GeV)
Electromagnetic	Photon (γ)	0	0
Weak	$W^{\pm}$	±1	80.403 ± 0.029
	Z	0	91.1876 ± 0.0021
Strong	Gluons (g)	0	0

Table 1.2: *Gauge bosons.*

The properties of the vector bosons are summarised in Table 1.2.

The Higgs boson with spin 0 is associated with the spontaneous breaking of the electroweak (EW) gauge symmetry. It has not yet been observed experimentally.

1.2.2 Channels involving neutrinos

As shown in Table 1.1, the neutrinos are massless particles interacting only through weak interactions. Therefore their detection is possible only using dedicated massive experiments [3] and they cannot be detected in experiments at hadronic colliders which are designed to study massive particles.

Neutrinos are involved in the decays of many particles that can be produced at the LHC and thus they are the physics objects that are mainly responsible for non-zero E_T^{miss} values in a physics event.

A brief summary of SM processes involving neutrinos is presented in the following.

W boson decays

W bosons decay either hadronically ($\mathrm{B}(W \to q\bar{q}) = 67\%$) or leptonically ($\mathrm{B}(W \to l\nu) = 33\%$). In this second case the neutrino has an average energy of about 40 GeV, a half of the W mass value and therefore a significant amount of E_T^{miss} is an important signature of such a decay.

The W mass is a fundamental parameter for the Standard Model, related to other parameters of the theory, such as the electromagnetic coupling constant α_{EM}, the Fermi constant G_F and the sine of the Weinberg angle θ_W, through the relation:

$$m_W = \sqrt{\frac{\pi\alpha_{EM}}{\sqrt{2}G_F}}\frac{1}{\sin\theta_W\sqrt{1-\Delta r}} \tag{1.5}$$

where Δr accounts for radiative corrections, which amount to $\sim 4\%$ and depend on the top quark mass as $\sim m_{top}^2$ and on the Higgs mass as $\sim \ln m_H$. Thus the W boson mass is a crucial ingredient of the Standard Model global fit: a precise measurement allows consistency checks of the model, insights at new physics and constraints of the Higgs boson mass.

At hadron colliders the measurement of the W mass is performed in $W \to e\nu$ and $W \to \mu\nu$ channels. In the context of Tevatron experiments providing more and more precise results (the world average is now 80.399 ± 0.023 GeV [4]), the LHC experiments can contribute thanks to the high cross section of W and Z productions, Z events being used to calibrate the detector and constrain the systematics uncertainties. The LHC will produce around 20×10^6 W bosons and 2×10^6 Z bosons per leptonic decay channel and per fb^{-1} at a centre-of-mass energy of 14 TeV, thus statistical uncertainties will become negligible very fast and the real challenge will be to control the systematic uncertainties. To improve the Tevatron ultimate accuracy, LHC experiments have to achieve a precision of ~ 20 MeV on the W mass, i.e. $\sim 1‰$.

The invariant mass of the lepton-neutrino system can not be reconstructed because the longitudinal momentum of the neutrino is not known. Therefore the transverse mass m_T is used instead. The transverse mass is the mass obtained from the lepton transverse momentum and E_T^{miss} as in Equation 1.6:

$$m_T = \sqrt{2p_T^l E_T^{miss}(1 - \cos(\phi^l - \phi^{E_T^{miss}}))}. \tag{1.6}$$

Here ϕ is the azimuthal angle between the lepton and E_T^{miss} directions .

A very good measurement of the missing transverse energy in $W \to l\nu$ events is mandatory to measure the transverse mass distribution of the W boson that is then fitted with Monte Carlo samples generated with different values of m_W to find the mass which best fits the data.

Figure 1.2 shows the lepton-E_T^{miss} transverse mass distribution at the LHC with the requirement of $E_T^{miss} > 25$ GeV obtained with the first ~ 300 nb^{-1} of data taken at $\sqrt{s} = 7$ TeV [5]. Requiring events with $m_T > 40$ GeV a sample with less than 10% of background contamination can be collected.

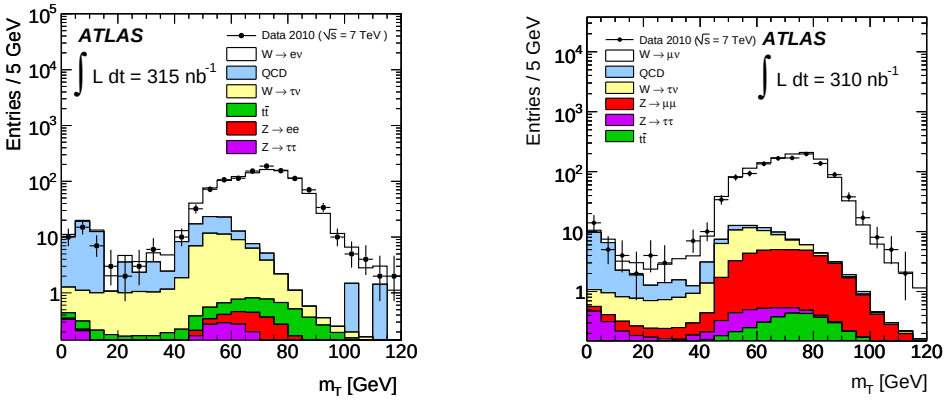

Figure 1.2: *Distributions of the transverse mass, m_T, of the electron-E_T^{miss} system (left) and muon-E_T^{miss} system (right) with a requirement of $E_T^{miss} > 25$ GeV. The ATLAS at 7 TeV data are compared to Monte Carlo simulation, broken down into the signal and various background components [5].*

Top quark decays

Within the Standard Model the top quark almost always decays in the mode $t \to Wb$. Then, as described above, when the W decays to leptons, the production of a neutrino occurs. In addition the particles resulting from the

hadronisation of the b quark can decay producing a charged lepton and the correspondent neutrino.

Because of its large mass, its large width (which makes it decay before hadronising) and its importance in the radiative corrections to the W mass value, precision measurements in the top sector can be important to get more clues on the origin of the fermion mass hierarchy.

The best channel to measure the top mass at hadron colliders is $t\bar{t}$ production where one top decays semileptonically ($\mathrm{t} \rightarrow W\mathrm{b} \rightarrow l\nu\mathrm{b}$, where $l = e, \mu$) and the other one hadronically ($\mathrm{t} \rightarrow W\mathrm{b} \rightarrow jj\mathrm{b}$). These events can be selected requiring high p_T lepton and high E_T^{miss} values and possibly b-jets.

Furthermore E_T^{miss} is one of the most important quantities for discriminating $t\bar{t}$ events in the dilepton and lepton+jets channels from backgrounds which do not contain genuine E_T^{miss} such as Drell-Yan processes and QCD multi-jets. Figure 1.3 shows the E_T^{miss} distribution in the dilepton channel from ATLAS top analysis. Requiring $E_T^{miss} > 40$ GeV (30 GeV) in ee ($\mu\mu$) channel removes Drell-Yan and QCD background component. Both the magnitude of E_T^{miss} and the correlation between the direction of E_T^{miss} and other objects in the events (e.g. leptons or jets) can be used as rejection criteria. The degree of separation depends on the E_T^{miss} resolution, which is therefore of great importance.

Additionally, many theories beyond the Standard Model predict signatures with large E_T^{miss}, where $t\bar{t}$ is the dominant background. Therefore, a good understanding of this kinematic variable, and notably the tails of E_T^{miss} distribution, is very important in this context.

τ lepton decays

Taus are unstable particles with a lifetime of $c\tau = 87.11$ μm, and will decay before reaching any of the ATLAS detectors. Therefore, they must be reconstructed from the detection of their decay products. Tau decays are categorised into leptonic (35.2%) and hadronic (64.8%) modes, each one containing at least one neutrino. Feynman diagrams of the decay modes are given in Figure 1.4.

Invariant $\tau\tau$ mass reconstruction

A very good E_T^{miss} measurement is fundamental to reconstruct the invariant mass of the couple of τ leptons in case of $Z \rightarrow \tau\tau$ decays and also for Higgs bosons decays to τ (see Sections 1.3.2 and 1.4.3).

The invariant mass of the τ-pair in events

$$Z \rightarrow \tau^+\tau^- \rightarrow \tau - jet\ \overline{\nu_\tau}\ l\ \overline{\nu_l}\nu_\tau$$

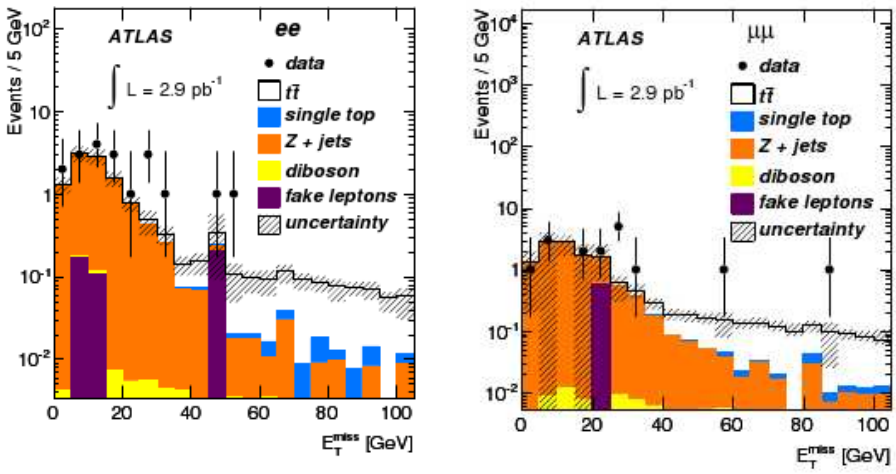

Figure 1.3: *Distributions of E_T^{miss} in the dilepton channel for top analysis: ee channel (left) and μμ channel. Data taken 7 TeV data with ATLAS are compared to Monte Carlo simulation, broken down into the signal and various background components [6].*

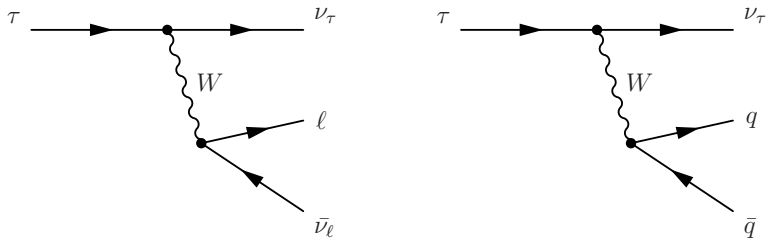

(a) leptonic (35.2%) (b) hadronic (64.8%)

Figure 1.4: *Tau-Lepton decay modes. In the leptonic mode, only the lepton is visible in the detector, and the decay cannot be distinguished from a prompt lepton (e.g. $W \rightarrow e\nu$). In the hadronic mode the quarks fragment into a number of charged and neutral hadrons that provide a unique signature in the detector. In both cases neutrinos are created.*

can be reconstructed under the assumptions that $m_\tau = 0$, that the directions of the two neutrino systems from each τ-decay ($\nu_1 = \overline{\nu_\tau}$, $\nu_2 = \overline{\nu_l}\nu_\tau$) are coincident with those of the measured τ-decay products (*collinear approximation*) and under the condition that the τ-decay products are not back-to-back:

$$m_{\tau\tau} = \sqrt{2(E_1 + E_{\nu_1})(E_2 + E_{\nu_2})(1 - \cos\theta)} \tag{1.7}$$

where

- E_1, E_2 are the energies of the measured τ-decay products
- E_{ν_1}, E_{ν_2} are the energies of the two neutrino systems ($\nu_1 = \overline{\nu_\tau},\ \nu_2 = \overline{\nu_l}\nu_\tau$) from τ-decay
- θ is the angle between the directions of the measured τ-decay products.

E_{ν_1} and E_{ν_2} are obtained by resolving a system containing the two E_T^{miss} components:

$$E_{x,y}^{miss} = (E_{\nu_1} * \overline{u_1})_{x,y} + (E_{\nu_2} * \overline{u_2})_{x,y} \tag{1.8}$$

where $\overline{u_1}$, $\overline{u_2}$ are the directions of the measured τ-decay products and $E_{x,y}^{miss}$ are the two components of the E_T^{miss} vector.

This system can be solved if the determinant, $\sin\Delta\phi$, is not zero, where $\Delta\phi$ is the azimuthal angle between the jet and the lepton produced in the τ decay.

An accurate measurement of E_T^{miss} is very important because poor measurements of $E_{x,y}^{miss}$ together with errors in the assumption made on the particle directions contribute to the width of the reconstructed mass and can result in unphysical negative solutions for E_{ν_1} and E_{ν_2}. In this case the Z mass can not be reconstructed.

The invariant mass reconstruction is a crucial point in the context of the $Z \rightarrow \tau\tau$ and Higgs to τ pairs analyses as it has a strong background suppression power due to the fact that for most background events $m_{\tau\tau}$ can not be reconstructed. Therefore it allows to collect a very pure signal sample with a very low background contamination that can be used also to measure the $Z \rightarrow \tau\tau$ cross section.

Furthermore the E_T^{miss} resolution is the dominant factor for the $m_{\tau\tau}$ resolution and the peak position of $m_{\tau\tau}$ distribution depends on the E_T^{miss} scale as discussed in Chapter 4.

1.3 E_T^{miss} and Standard Model Higgs

Despite the success of the Standard Model, whose predictions have been verified at the level of 0.1% [7] or better by the LEP, SLC and Tevatron experiments, some aspects of the model are still obscure. In particular the origin of the particle masses is unknown.

The Higgs mechanism provides a way to break the electroweak symmetry and to provide masses to particles. As a consequence of this mechanism a scalar particle, the Higgs boson, is predicted whose mass is not specified by the theory but which should not exceed 1 TeV to preserve unitarity at high energy. Such a particle has not been found yet.

A lower bound on the Higgs boson mass comes from direct Higgs boson searches at the Large Electron Positron Collider (LEP) at CERN. The combined results of LEP experiments (ALEPH, DELPHI, L3 and OPAL) on the direct searches for the Higgs boson conclude that the SM Higgs boson must be heavier than $m_H \geq 114.4$ GeV at 95% confidence level (C.L.) [8].

LHC experiments are thus designed to be able to explore the Higgs mass range from ~ 120 GeV up to the theoretical upper bound of 1 TeV.

1.3.1 Higgs mechanism

The EW gauge bosons, W and Z are heavy, having masses of 80 GeV and 91 GeV respectively, however, gauge theories predict massless gauge bosons. The inclusion of such fields into a gauge theory is nontrivial, as gauge boson mass terms of the form $M^2 V_\mu V^\mu$ (introduced by hand) break the local gauge invariance. To solve this problem, the gauge theory must be spontaneously broken. This is achieved in the SM through the Higgs mechanism, where a new complex scalar field (ϕ) is introduced. The Lagrangian for the simple case of a single massless gauge field A_μ is given here for example:

$$\mathcal{L} = -\frac{1}{4} F^{\mu\nu} F_{\mu\nu} + |D_\mu \phi|^2 - V(\phi), \tag{1.9}$$

where $V(\phi)$ is the scalar potential defined as:

$$V(\phi) = -\mu^2 |\phi|^2 + \frac{\lambda}{2} |\phi|^4. \tag{1.10}$$

The field ϕ is designed in such a way that the minimum of the scalar potential $V(\phi)$ occurs at a non-zero field value ($|\phi| = \frac{v}{\sqrt{2}} = \sqrt{\frac{\mu^2}{2\lambda}}$) as shown in Figure 1.5.

If a change of state occurs, causing a transition from high energy density to low energy density (such as in the early universe), the field will spontaneously fall into a minimum of the potential. As the field at the minima has non-zero expectation values ($\langle \phi \rangle = \pm v$), the original symmetry is broken. At its minimum, the field can be written as:

$$\phi = v + \frac{1}{\sqrt{2}} (\phi_1 + i\phi_2). \tag{1.11}$$

Upon substitution of Equation 1.11 into Equation 1.9, one finds a mass term for the gauge boson of the form $g^2 v^2 A_\mu A^\mu$, and a single physical scalar field ϕ_1 with mass $m_{\phi_1} = \sqrt{\lambda v^2}$.

The mass term for the gauge boson completely defines v, however due to the remaining unknown parameter λ, the mass of ϕ_1 is unpredicted.

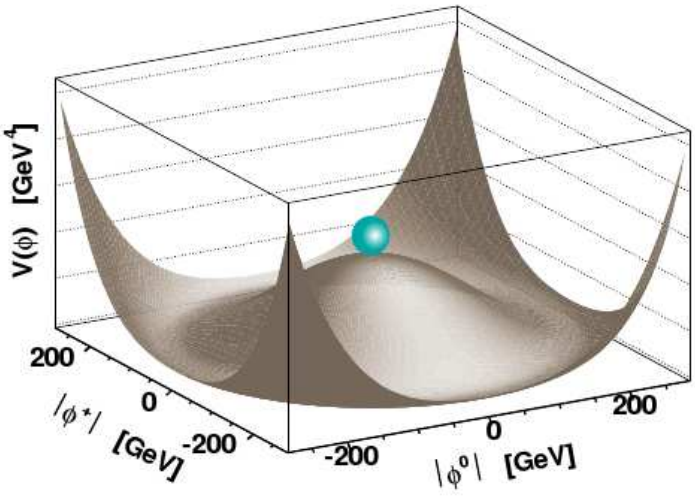

Figure 1.5: *Spontaneously broken Higgs potential. The minimum occurs not at zero but at* $-\mu^2/(2\lambda)$ *[9].*

Self-coupling terms of the scalar also arise, but depend on λ, so they are unpredictable. On the other hand, gauge coupling terms of the form $vg^2\phi_i A_\mu A^\mu$ and $g^2\phi_i^2 A_\mu A^\mu$ appear, and since they depend only on g and v, their strengths are completely predicted.

The prediction of the coupling strength of the scalar to a pair of gauge bosons is extremely important, as it allows strong statements regarding the existence of such a particle to be made, from experimental observation of the particle in production and decay via pairs of gauge bosons.

Finally, the field ϕ_2 remains massless, and as it can be removed by a gauge transformation is considered unphysical. The field ϕ_2 is referred to as a Goldstone boson, and its original degree of freedom manifests as the longitudinal polarisation state of the gauge boson. In the SM, ϕ is required to be an $SU(2)$ doublet $\binom{\phi^+}{\phi^0}$, containing four real fields. Spontaneous symmetry breaking (SSB) results in one physical Higgs boson and three massive gauge bosons ($W^\pm$ and Z). Despite the added complexity, the basic mechanics of the Higgs mechanism remains unchanged.

The vacuum expectation value, v, in the SM is then given by:

$$v = 2m_W/g_W = \left(\frac{1}{\sqrt{2}G_F}\right)^{\frac{1}{2}} = 246\text{GeV}, \tag{1.12}$$

where g_W is the dimensionless weak coupling constant, and G_F is the Fermi

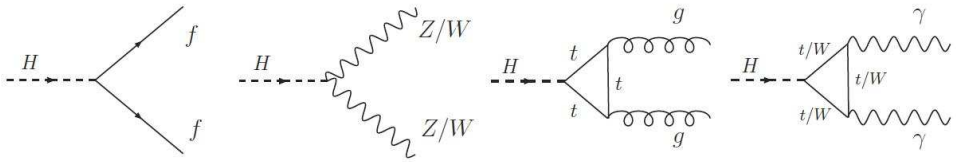

Figure 1.6: *Tree-level Feynman diagrams of the Higgs boson decay processes in pp collisions at the LHC.*

coupling constant.

The inclusion of mass terms for the chiral fermion fields in the SM is also problematic because left handed fermions (f_L) are in $SU(2)$ doublets, while right-handed fermions (f_R) are in $SU(2)$ singlets. Terms of the form $m\bar{f}f = m(\bar{f}_L f_R + \bar{f}_R f_L)$ include products of doublets and singlets, and therefore break $SU(2)$ invariance. However, inclusion of the SM Higgs into the fermion sector results in terms of the form:

$$g_f[(\bar{f}_L\phi)f_R + h.c.] \tag{1.13}$$

where the product $\bar{f}_L\phi$ is an $SU(2)$ singlet. After acquiring a vacuum expectation value the fermions obtain mass terms of the form:

$$\sqrt{\frac{1}{2}}g_f v(\bar{f}_L f_R + \bar{f}_R f_L) \tag{1.14}$$

where g_f is a Yukawa coupling constant that is proportional to the fermion mass. The Yukawa couplings are determined by the measured masses of the fermions, therefore the production and decay rates of the Higgs boson through fermion pairs are predicted in the SM.

Thus, the Higgs mechanism that was originally introduced as a method to spontaneously break electroweak symmetry is also able to generate gauge invariant mass terms for chiral fermions. With the inclusion of fermion mass terms, couplings of the Higgs boson to both fermions and gauge bosons is completely defined, which maps out a large fraction of phase space that can be experimentally probed.

1.3.2 VBF Higgs decay to a pair of τ leptons

The branching ratios of the Standard Model Higgs boson decays depend on m_H as unknown parameter. Since the Higgs boson couples to other particles proportional to their masses, it decays dominantly into the most massive accessible particles. Feynman diagrams of the SM Higgs boson decays are shown in Figure 1.6: the tree-level decays into a fermion pair

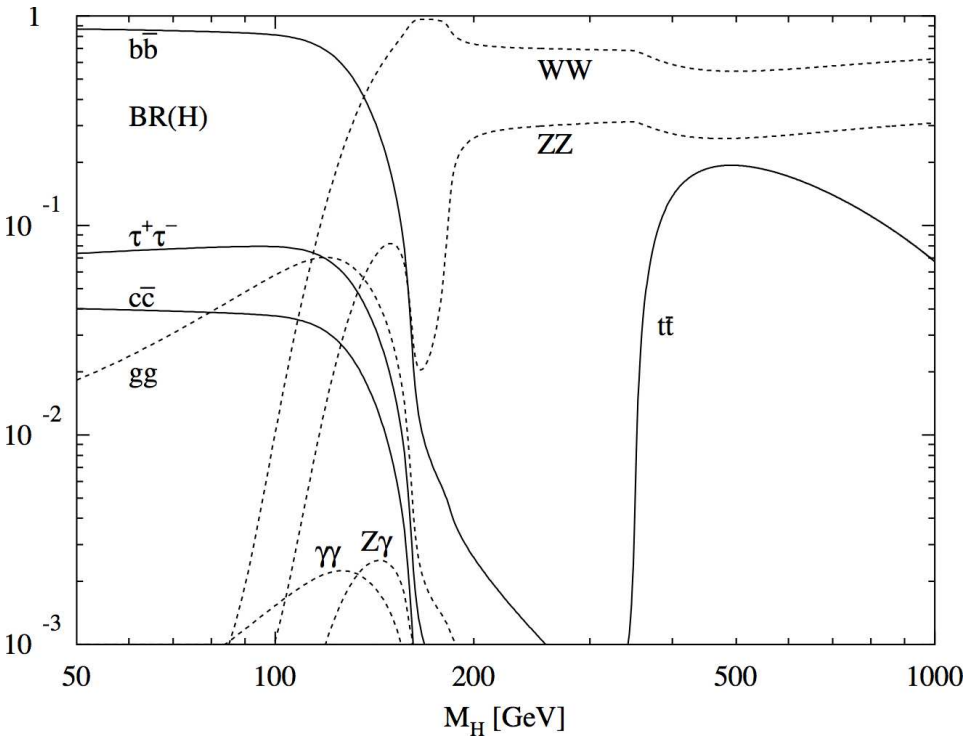

Figure 1.7: *Branching ratios of the Standard Model Higgs boson decays as a function of the Higgs boson mass M_H [9].*

or a real or weak gauge boson pair and, via loops, into massless photons or gluons. The branching-ratios of the most important decay channels are illustrated in Figure 1.7. For Higgs masses up to 150 GeV fermionic decay modes are dominant, in particular the decays to a couple of b or to a couple of τ.

In case of Higgs boson produced via Vector Boson Fusion, whose Feynman diagrams shown in Figure 1.8, the $H \rightarrow \tau^+\tau^-$ decay is a very interesting discovery channel. In fact although it suffers from high background mainly from $Z \rightarrow \tau\tau$ decays, if one exploits the signatures of vector-boson fusion Higgs production, this decay channel is one of the most promising ones for $m_H \leq 140$ GeV.

The VBF $H \rightarrow \tau^+\tau^-$ is characterised by two leptons (e or μ) or τ-jets in the central region of the detector, missing transverse energy from neutrinos and two jets in the forward region of the detector.

The performance of the E_T^{miss} algorithm plays a central role in this analysis because E_T^{miss} is used in the mass reconstruction of the tau pair, as for the $Z \rightarrow \tau\tau$ events. As introduced in Section 1.2.2 a good E_T^{miss} measurement

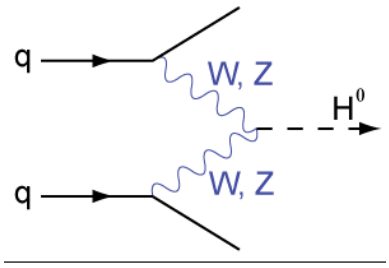

Figure 1.8: *Feynman diagram of Higgs production via Vector Boson Fusion.*

allows to reconstruct the invariant $m_{\tau\tau}$ and its resolution is dominated by the E_T^{miss} resolution. The invariant mass cannot be reconstructed for most background events thus it is very helpful in background suppression. Furthermore, the absolute scale of E_T^{miss} must be well calibrated to correctly reconstruct the Higgs boson mass.

1.4 E_T^{miss} and physics beyond the Standard Model

There are both conceptual reasons and phenomenological indications for physics beyond the SM. On the conceptual side the most obvious problems are that quantum gravity is not included in the SM and the related hierarchy problem. Among the main phenomenological hints for new physics there is coupling unification, dark matter, neutrino masses, baryogenesis and the cosmological vacuum energy [7].

Although the Higgs mass range 114 GeV $\leq m_H \leq$ 180 GeV seems to allow the Standard Model to survive up to the Planck scale this hypothesis is considered to be unlikely: this conclusion is based on the *naturalness* argument. In an effective field theory the masses can be calculated in terms of parameters of a more fundamental renormalizable theory that describes physics at the energy scale Λ. In the SM the Higgs boson mass is quadratically sensitive to the scale Λ, at one loop:

$$m_H^2 = (m_H^2)_0 + cg^2\Lambda^2 \tag{1.15}$$

where $(m_H^2)_0$ is a parameter of the more fundamental theory and c is a constant O(1). Therefore, assuming an upper limit to the Higgs mass of 1 TeV one can obtain a *natural* value for $\Lambda \simeq m_H/g \sim O(1)$. If Λ is significantly larger than 1 TeV (hierarchy problem) only an *unnatural* cancellation (fine tuning) between the two terms in Equation 1.15 could explain a Higgs mass at the order of the electroweak symmetry breaking.

The impressive success of the SM sets strong limits on models for new physics: in general, models that preserve the SM structure and introduce soft improvements are clearly preferred.

1.4.1 Supersymmetry

SuperSymmetric (*SUSY*) models are the most developed and widely accepted theories to solve the SM problems: the supersymmetric extension of the SM is a well defined and computable model which also preserves all features of the SM. Supersymmetry is a theory that postulates a symmetry connecting fermions and bosons.

In fact the Supersymmetry operator Q is designed to transform fermionic and bosonic states as such:

$$Q \mid \text{fermion} \rangle = \mid \text{boson} \rangle, \qquad Q \mid \text{boson} \rangle = \mid \text{fermion} \rangle. \quad (1.16)$$

Each SM particle is put in a *supermultiplet* paired with its own *superpartner*. The superpartner lays in the same gauge group representation, and the supermultiplet must have equal fermionic and bosonic degrees of freedom.

If the symmetry exists at high energies, then additional fermionic loops would cancel the quadratic divergences of bosons solving the hierarchy problem. In addition, supersymmetric theories require two Higgs doublets.

The fact that no supersymmetric particles have yet been observed means that supersymmetry is not an unbroken symmetry of nature. In the Minimal Supersymmetric extension to the Standard Model (MSSM) there are no assumptions made to the SUSY−breaking mechanism. Instead, all possible SUSY−breaking terms are considered, giving rise to more than 100 new, fundamental parameters. Models exist in which the low-energy parameters are determined from only a few parameters, which live at a much higher scale, by assuming a specific SUSY-breaking mechanism. These models include minimal-Supergravity (mSUGRA), minimal Gauge Mediated SUSY Breaking (mGMSB) and minimal Anomaly Mediated SUSY Breaking (mAMSB) [10].

No signal of new physics has been found experimentally yet. However, to make a light Higgs natural in presence of quantum fluctuations new physics should not be so far. This is encouraging for the LHC that should experimentally clarify the problem of the electroweak symmetry breaking sector and probably find new physics signatures at the TeV scale.

1.4.2 Minimal Supersymmetric Standard Model

The MSSM is minimal in the sense that it contains the smallest possible field content necessary to give rise to all the fields of the Standard Model. This can be done as follows:

- Associating fermionic superpartners to all gauge fields. Gluons, $W^{\pm}$ and Z bosons, obtaining fermionic partners called *gluinos* ($\tilde{g}$), *winos* ($\tilde{W}^i$) and *zinos* ($\tilde{Z}$) respectively. The common name for all partners of gauge fields is *gaugino*.

- Associating scalar partners to the fermions, i.e. quarks and leptons get scalar partners called *squarks* and *sleptons*.

- introducing one additional Higgs field (for a total of two Higgs doublets, corresponding to five physical Higgs states) and associating one spin 1/2 *Higgsino* to each Higgs boson. This is done to give masses to both up and down-type quarks upon electroweak symmetry breaking and also preserve supersymmetry (therefore, we cannot use the conjugate of the Higgs as is done in Standard Model). Introducing another Higgs doublet also makes the theory anomaly free.

Table 1.3 lists the SUSY particles in the MSSM model.

	Standard Particles		Supersymmetric Partners			
Charge	Particle	Spin	Sparticle	Spin	Name	Eigenstates
-1	e	$\frac{1}{2}$	$\widetilde{e}_L, \widetilde{e}_R$	0	selectron	
-1	μ	$\frac{1}{2}$	$\widetilde{\mu}_L, \widetilde{\mu}_R$	0	smuon	
-1	τ	$\frac{1}{2}$	$\widetilde{\tau}_L, \widetilde{\tau}_R$	0	stau	
0	$\nu = \nu_e, \nu_\mu, \nu_\tau$	$\frac{1}{2}$	$\widetilde{\nu}$	0	sneutrino	
$-\frac{1}{3}, +\frac{2}{3}$	$q = d, u, s, c, b, t$	$\frac{1}{2}$	$\widetilde{q}_L, \widetilde{q}_R$	0	squark	
0	g	1	$\widetilde{g}$	$\frac{1}{2}$	gluino	
0	γ	1	$\widetilde{\gamma}$	$\frac{1}{2}$	photino	neutralinos
0	Z	1	$\widetilde{Z}^0$	$\frac{1}{2}$	zino	$\widetilde{\chi}_1^0 ... \widetilde{\chi}_4^0$
0	h^0, H^0, A^0	0	$\widetilde{H}_1^0, \widetilde{H}_2^0$	$\frac{1}{2}$	neutral higgsino	
± 1	$W^{\pm}$	0	$\widetilde{W}^{\pm}$	$\frac{1}{2}$	wino	charginos
± 1	$H^{\pm}$	0	$\widetilde{H}^{\pm}$	$\frac{1}{2}$	charged higgsino	$\widetilde{\chi}_1^{\pm}, \widetilde{\chi}_2^{\pm}$

Table 1.3: *MSSM Particles.*

As said above, the Higgs MSSM sector contains two complex Higgs doublets that acquire vacuum expectation values v_1 and v_2, whose ratio is defined as $\tan\beta \equiv \frac{v_1}{v_2}$. The five physical Higgs bosons remaining after spontaneous symmetry breaking remain are two charged scalars $H^{\pm}$, two CP-even scalars h^0 and H^0, and one CP-odd scalar A^0. By definition $m_{h^0} < m_{H^0}$.

In general there are six free parameters describing the Higgs sector: four Higgs boson masses, $\tan\beta$ and the mixing angle α between the CP-even

Neutral MSSM Higgs boson coupling strengths

Higgs Boson	f_u	f_d	W/Z
h	$\cos\alpha/\sin\beta$	$-\sin\alpha/\cos\beta$	$\sin(\alpha-\beta)$
H	$\sin\alpha/\sin\beta$	$\cos\alpha/\cos\beta$	$\cos(\alpha-\beta)$
A	$1/\tan\beta$	$\tan\beta$	-

Table 1.4: *Coupling strengths of the neutral MSSM Higgs bosons compared to the SM Higgs boson, to up-type fermions (f_u), down-type fermions (f_d) and the weak gauge bosons.*

states. In the MSSM, relationships between the parameters can be determined from the structure of the superpotential, leaving only two free parameters at tree-level, generally taken to be m_{A^0} and $\tan\beta$.

The masses and coupling strengths to fermions and gauge bosons of all the Higgs bosons are completely defined at tree-level by the choice of these two parameters. The relationships also result in a number of important limits on the masses of the scalars:

$$\begin{aligned} m_{H^\pm} &\geq m_W \\ m_{H^0} &\geq m_Z \\ m_{A^0} &\geq m_{h^0} \\ m_{h^0} &\leq m_Z. \end{aligned}$$

The last limit gives a large constraint on the model, requiring at least one light Higgs boson below the Z boson mass. In fact, the LEP 95% exclusion limit covers the complete allowed range for m_{h^0} at tree level. However, loop corrections to m_{h^0} can be significant. Depending on couplings to the top quark, heavy scalars and mixing in the stop sector, m_{h^0} can be pushed up to ~ 135 GeV.

Not only the MSSM Higgs sector contains a completely different mass spectrum from the SM Higgs sector, but it can also result in very different couplings to the SM particles. Table 1.4 gives the ratio of the couplings of the neutral MSSM Higgs bosons to up-type fermions (f_u), down-type fermions (f_d) and the weak gauge bosons, with respect to the SM Higgs boson couplings.

1.4.3 Channels involving E_T^{miss} in MSSM model: LSP and MSSM Higgs decays

E_T^{miss} is particularly important in SUSY events and thus it is considered the key signature to discover SUSY processes.

LSP

If SUSY exists at the TeV scale, then gluinos and squarks will be copiously produced at the LHC. Their production cross sections are comparable to the jet production cross section. If R parity[1] is conserved, they have distinctive decays into jets, leptons, and the invisible lightest SUSY particle (LSP) $\tilde{\chi}^0$, which gives E_T^{miss}. Since the ATLAS experiment is designed to detect all of these, simple cuts can separate SUSY events from the Standard Model background. The main problem at the LHC is not to discover SUSY but to make precise measurements to determine the masses and other properties of SUSY particles.

Leptonic decays may or may not be large, but jets and E_T^{miss} are always produced, and these generally give the best reach. Many SUSY analyses focus on the measurement of an *effective mass* M_{eff} defined as the sum of E_T^{miss} and p_T of the jets (and leptons if any) in the event as in the Equation:

$$M_{eff} = E_T^{miss} + \sum_{i=1}^{njets} |p_T^i| + \sum_{j=1}^{nlep} |q_T^j|. \tag{1.17}$$

Figure 1.9 shows that the SUSY signal dominates for large E_T^{miss} and large M_{eff} values. It is also clear that a bad reconstructed E_T^{miss} value in a QCD event can fake a SUSY signal, therefore a high E_T^{miss} reconstruction quality is a crucial requirement for SUSY studies.

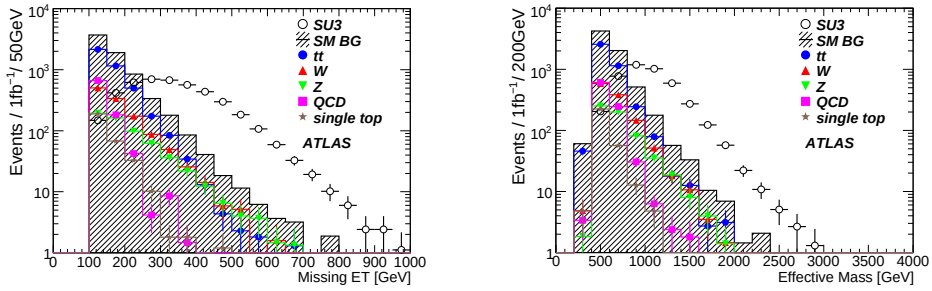

Figure 1.9: *The missing transverse energy (left) and effective mass (right) distributions of the SUSY signal and background processes for the no-lepton mode with an integrated luminosity of 1 fb^{-1} at a centre-of-mass energy of 14 TeV ATLAS Monte Carlo simulated data. The open circles show the SUSY signal. The shaded histogram shows the sum of all Standard Model backgrounds; different symbols show the various components [11].*

[1] R parity, defined as R= $(-1)^{2S+3B+L}$, is a discrete multiplicative symmetry where S is the particle spin, B is the baryon number, and L is the lepton number.

Neutral Higgs decays to a pair of τ lepton: $A/H \to \tau\tau$

In the MSSM the couplings of the Higgs bosons to fermions and bosons are different from those in the Standard Model resulting in different production cross sections and decay rates. As Table 1.4 shows, while decays into ZZ or WW are dominant in the Standard Model for Higgs boson masses above $m_H \sim 160$ GeV, in the MSSM these decay modes are either suppressed by $\cos(\beta - \alpha)$ for the H boson (where α is the mixing angle of the two CP-even Higgs bosons) or even absent for the A boson. However, the coupling of the Higgs boson to third-generation fermions is a function of $\tan\beta$ and is therefore strongly enhanced for large regions of the MSSM parameter space,

The two dominant production modes are b-quark associated production and gluon fusion. In most of the parameter space, Higgs boson decay is completely dominated by the modes $\phi \to b\bar{b}$ ($\sim$90%) and $\phi \to \tau\tau$ ($\sim$10%). Although the $b\bar{b}$ mode has a much larger branching fraction, it is extremely difficult to separate from the overwhelming QCD di-jet background. On the other hand, the tau mode has more distinctive features for discriminating against QCD di-jets and provides much better signal sensitivity.

In the decays to $\tau\tau$, the τs can either decay leptonically or hadronically forming three final states: $\ell\ell$ (12%), $\ell\tau_h$ (46%) and $\tau_h\tau_h$ (42%).

- The $\tau_h\tau_h$ mode suffers similar difficulties as the $b\bar{b}$, being very difficult to separate from the QCD background, but its study is possible for A/H masses above 500 GeV.

- The $\ell\ell$ mode, while providing good suppression of the QCD background, is limited by the branching fraction and is possible only for low A/H masses.

- The $\ell\tau_h$ mode has the largest branching fraction and can be adequately separated from the QCD background, providing the best sensitivity over a large range of the MSSM parameter space.

The three different modes analyses can be combined to improve the result. In the mass range $m_A \geq 150$ GeV, m_A and m_H are degenerate to less than 1 GeV, while m_h is well below m_A. Therefore the signal from A and H sum together and can be searched for with a single analysis, however, the analysis is not sensitive to h.

Figure 1.10 shows the region of MSSM parameter space ($\tan\beta$ vs m_A) which can be accessed by ATLAS with an integrated luminosity of 30 fb^{-1}and $\sqrt{s} = 14$ TeV [12].

Figure 1.11 shows in particular the discovery potential in the MSSM parameter space of the $A/H \to \tau\tau$ channel in the m_h^{max} scenario [13]. The

results of lepton-hadron analysis are evaluated taking into account the theoretical uncertainty on the signal cross section and with a fully correlated treatment of systematic uncertainties. The discovery potential without inclusion of systematic uncertainties is also shown for comparison with previous results shown in Figure 1.10 [14]. The results from the lepton-lepton analysis are superimposed including only experimental systematic uncertainties and a 10% theoretical uncertainty on the $t\bar{t}$ cross-section.

For low Higgs boson masses up to $m_A = 150$ GeV the discovery potential is dominated by the results from the fully-leptonic channel and a 5σ discovery can be achieved for values of $\tan\beta$ as low as ~ 10. For higher Higgs boson masses, the result is dominated by the lepton-hadron channel. For the highest Higgs boson masses a 5σ discovery is only possible for values of $\tan\beta$ as high as ~ 40. It can be combined with the results from the hadron-hadron channel, not shown here [15].

The decay of the neutral Higgs bosons into a pair of τ leptons constitutes an important discovery channel at the LHC. To study this channel a very good invariant $\tau\tau$ mass reconstruction, described in Section 1.2.2, is important and thus a precise E_T^{miss} measurement is crucial to exploit this kind of study.

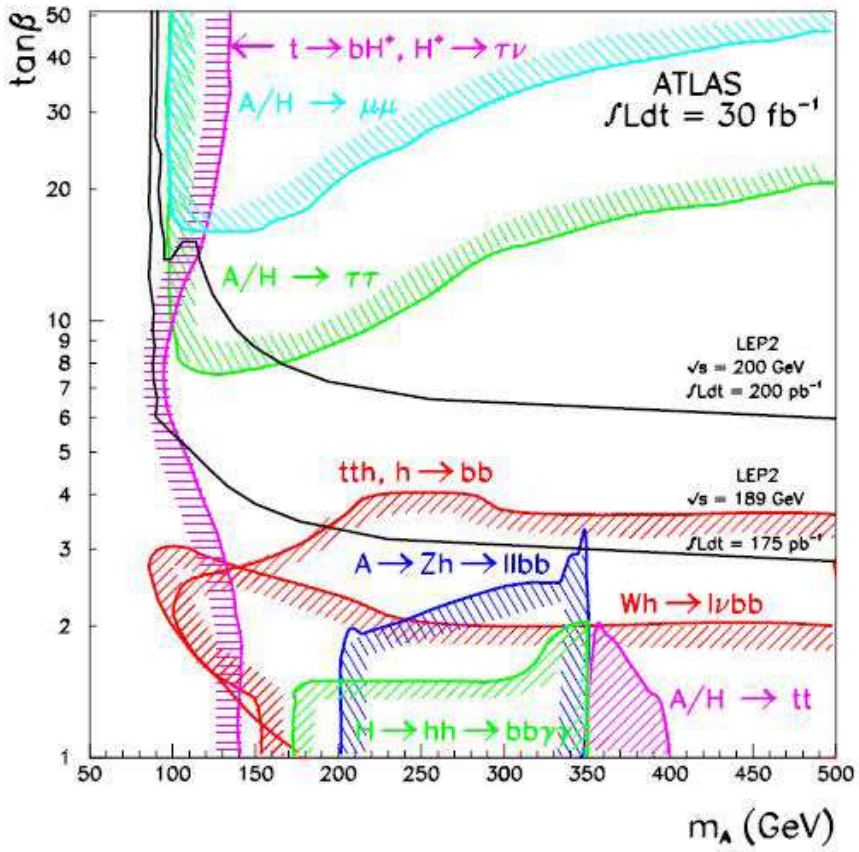

Figure 1.10: *Region of MSSM parameter space which can be accessed by ATLAS (30 fb^{-1} of integrated luminosity) [12].*

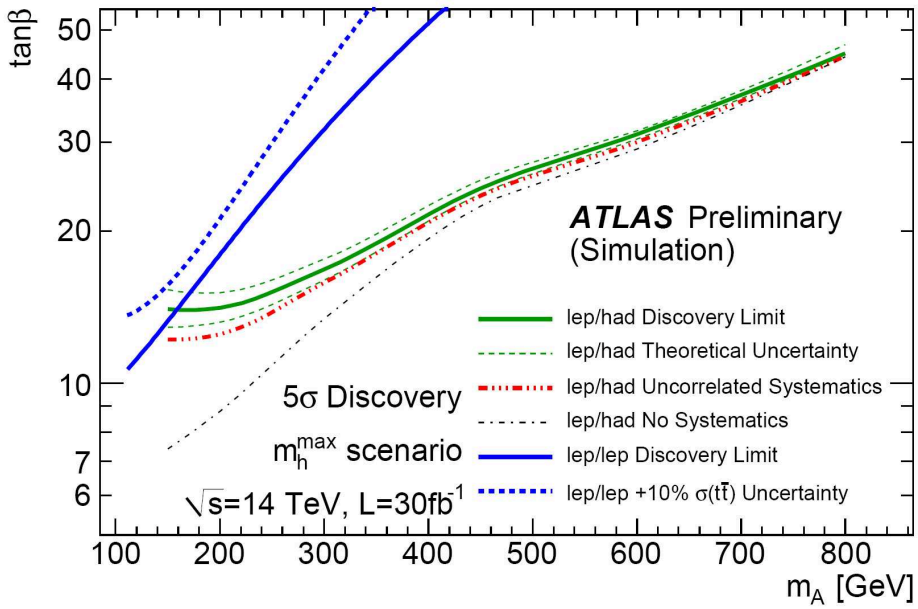

Figure 1.11: *The 5σ discovery potential as a function of* $\tan\beta$ *and* m_A *for* $A/H \to \tau\tau$ *channel. The solid green line is the result of the lepton-hadron analysis. The dashed green lines indicate the effect of the theoretical uncertainty on the signal cross section. The red line gives the results for the fully correlated treatment of systematic uncertainties. The dash-dotted black line shows the discovery potential without inclusion of systematic uncertainties for comparison with previous results [14]. The results from the lepton-lepton analysis are superimposed as blue lines. The solid line indicates the result including only experimental systematic uncertainties and the dashed line indicates the result including a 10% theoretical uncertainty on the* $t\bar{t}$ *cross-section [16].*

Chapter 2

The ATLAS detector at the LHC

ATLAS (A Toroidal LHC ApparatuS) is one of the four main experiments at the Large Hadron Collider (LHC) at CERN. In this chapter a brief introduction to the LHC collider and its physics environment is given, together with a description of the ATLAS detector. The methods for the reconstruction and identification of physics objects of interest for this work are reported, and some relevant performance results of the detector with pp collisions at $\sqrt{s} = 7$ TeV are reviewed.

2.1 The LHC collider

The LHC is designed to provide proton-proton as well as heavy ions collisions. As said in Chapter 1, when running in p-p mode, the design luminosity[1] is of 10^{34} cm^{-2} s^{-1} and the centre-of-mass energy of 14 TeV providing almost an order of magnitude increase in the maximum attainable collision energy, previously reached by the Tevatron. This will open up a new horizon for particle physics.

The production cross sections some processes at proton-(anti)proton colliders are given in Figure 2.1. The cross section for Higgs boson production at the LHC is of particular interest, since in the case of large Higgs mass

[1] Luminosity is defined as

$$L = f\frac{n_1 n_2}{4\pi\sigma^2}F \tag{2.1}$$

where σ is the transverse width of the beam (the particle distribution in the beam is supposed to be gaussian), that in the case of the LHC is 17 μm (nominal), f is the collision frequency, that is the reciprocal of the time delay between two collisions (1/25 ns = 40 MHz), n_1 and n_2 are the numbers of particles in the two colliding beams respectively (at the LHC $\sim 10^{11}$ protons per bunch are foreseen at nominal conditions) and F is a reduction factor due to the crossing angle (~ 0.85 at the LHC).

it can increase by many orders of magnitude with respect to the Tevatron. In general, the increase in collision energy from the Tevatron to the LHC results in a huge increase in the production cross section for any new particles in the mass range 500 GeV $\lesssim m \lesssim$ 5 GeV. This provides sensitivity to a large region of parameters space (including many theories beyond the Standard Model) that was inaccessible to the Tevatron.

The LHC is located at CERN, in the existing 26.7 km long tunnel built for the Large Electron-Positron (LEP) collider. The proton beams are kept in orbit by superconducting magnets operating at a temperature of 1.9 K and fields above 8 T and are accelerated by a 400 MHz superconducting cavity system.

The LEP tunnel has eight possible interaction points, of which four are active at the LHC. Two general purpose experiments: ATLAS and CMS are positioned at Point 1 and Point 5, with focus on the discovery of new physics. LHCb is located at Point 8 and is designed to study B-physics. ALICE (located at Point 2), is a dedicated experiment for the study of quark-gluon plasma, which is expected to be produced in Pb-Pb collisions.

A schematic layout of the LHC is shown in Figure 2.2.

The LHC started operations on 10 September 2008, but immediately after, during the commissioning phase, a major accident imposed a one year stop. During fall 2009 operations started again, culminating in the first 900 GeV collisions, recorded by the LHC experiments on 23 November 2009, and followed shortly after by collisions at 2.36 TeV, the highest energy ever reached before. For machine safety reasons it was decided to limit the maximum centre-of-mass energy to 7 TeV, and the first collisions at this world record energy took place on the 30 March 2010. From then on the number of proton bunches and the number of bunches per beam has been increasing day by day, reaching an instantaneous luminosity of 2.1×10^{32} cm^{-2} s^{-1} at the time this thesis was written.

2.2 Physics at the LHC

The LHC physics program is very ambitious and covers a variety of topics in particle and nuclear physics. In particular the main objectives are:

- The discovery of particles giving rise to the spontaneous symmetry breaking in the SM. The reach for a standard Higgs boson extends from masses from the LEP exclusion limit of 114.4 GeV [8] up to about 1 TeV. If the Higgs boson is found its mass and couplings will be determined.

- Test of the validity of the SM, with precision measurements of the W and top-quark masses and couplings, b-physics and CP violation.

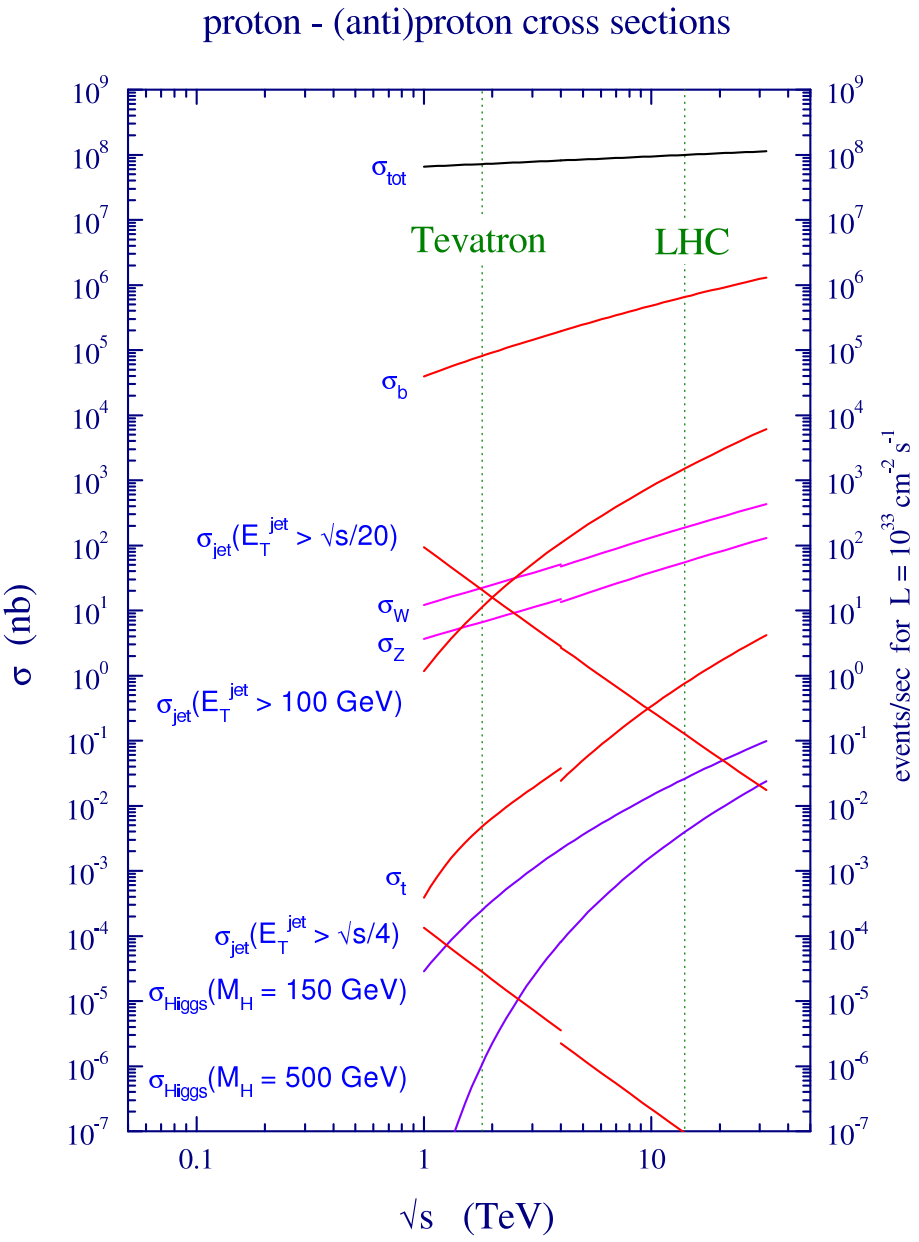

Figure 2.1: *Cross sections vs. collision energy ($\sqrt{s}$) for physics processes at proton-(anti)proton colliders [17]. Note the large increase in the rate of Higgs boson production from the Tevatron to the LHC.*

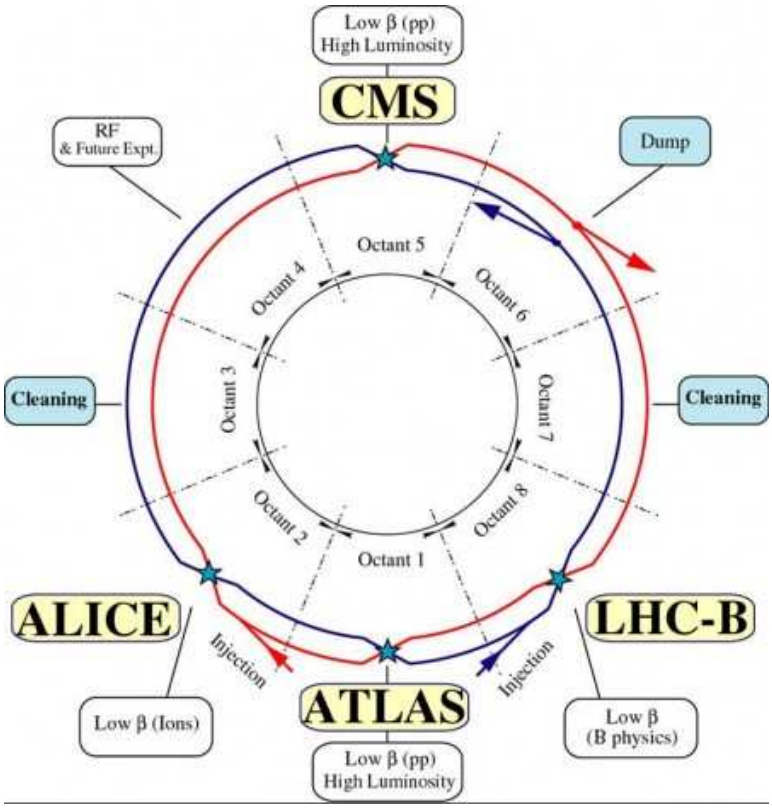

Figure 2.2: *Schematic layout of the LHC [18].*

- Search for signatures beyond the Standard Model, in particular of particles predicted by various Supersymmetry models.

- Study of the properties of hadronic matter under extreme conditions, and possibly the transition to a state in which quarks and gluons are deconfined, called quark-gluon plasma. This will allow an insight of the behavior of matter at the dawn of time shortly after the Big Bang.

The very high luminosity of the LHC is needed to pursue these objectives, since the cross sections of the processes of interest are very low. But a high luminosity regime introduces some difficulties as well. One of them is the presence of pileup, that is the superposition of high cross section inelastic events over the candidates for new physics. At design luminosity 23 pileup events per bunch crossing are expected. Another difficulty due to the nature of proton-proton collisions is that QCD processes will dominate over the processes physicists are most interested in. This imposes strong demands

on the integrated luminosity needed and on the capability of the detectors to identify experimental signatures characteristic of the processes under study. The physics goals therefore translate into requirements the LHC detectors have to face:

- **Fast response, high granularity and resistance to radiations.** The rates of events require a fast and sophisticated electronics, able to discriminate events and minimize the effect of pileup. A high granularity of the detector is necessary to handle the high particle fluxes as well. The detectors must be resistant to high doses, both in terms of operation and aging.

- **Trigger**. The output bandwidth of the detector is limited, and therefore the 40 MHz interaction rate must be reduced to 200 Hz to be written to tape. The capability of triggering efficiently on interesting events with a very high background rejection is therefore crucial.

- **Full coverage**. The study of jets and E_T^{miss} is fundamental for the accomplishment of the physics goals. That requires a coverage over 2π in the azimuthal angle and pseudorapidity $|\eta| < 5$ (for the definition of pseudorapidity see Section 2.3.1).

- **Particle identification**. The capability to precisely reconstruct and identify electrons, muons, photons, tau leptons and jets is an essential requirement for the LHC experiments.

2.3 The ATLAS detector

The ATLAS detector surrounds the interaction region at Point 1 of the LHC collider. It was completed in 2008 after five years of assembly works. ATLAS is a giant multipurpose detector. Even though its performances are aimed at the Higgs search, it can cope with the study of a variety of phenomena. In the following the general layout and nominal performances are briefly reported, together with a description of the main subsystems. A complete description of the detector can be found in [19].

2.3.1 Coordinate system

To aid with the description of the detector, a brief summary of the coordinate system and nomenclature is given.

- The nominal interaction point is defined as the origin of the coordinate system.

- The z-axis is parallel to the beam and the the x and y axes are perpendicular to the beam forming a right-handed cartesian coordinate system where x points towards the centre of the LHC ring and y points upward. The x-y plane is called the *transverse plane*.
- The azimuthal angle, ϕ, is measured around the z-axis and the polar angle, θ, is measured from the z-axis.
- The pseudorapidity, defined as $\eta = -\ln\tan(\theta/2)$, is often preferable as a polar coordinate as is distributes the transverse energy roughly evenly.
- The distance ΔR in η-ϕ space is defined as $\Delta R = \sqrt{\Delta\eta^2 + \Delta\phi^2}$.
- Particles are often described by their transverse momentum p_T and transverse energy E_T (projections in the transverse plane), as these variables are a better indicator of interesting physics than the standard energy and momentum and because they are conserved in the collision.

2.3.2 General layout

The general layout of ATLAS is shown in Figure 2.3. The detector has a cylindric symmetry. Its dimensions are 25 m height and 44 m in length, while the overall weight is approximately 7000 metric tons.

Each of the ATLAS sub-detectors plays an important role in the reconstruction of particles. The sub-detectors are arranged in layers leading out from the interaction point. Closest to the beam pipe is the tracking chamber, used to reconstruct the trajectory of charged particles. It is enclosed by a solenoid magnet, which provides a magnetic field in the chamber that bends the charged particles, thus allowing a measurement of their momentum and charge. The electromagnetic calorimeter encloses the tracking chamber and is designed to precisely measure the energy of electrons and photons. Outside the electromagnetic calorimeter is the hadronic calorimeter, which measures the energy of hadronic particles. Finally, the calorimeters are enclosed by the muon spectrometer designed to reconstruct and identify muons. The spectrometer houses large toroidal magnets to deflect the path of muons. Combined with the tracking chambers it provides precise measurements of momentum and charge. They will be described in the further sections together with the trigger system.

As introduced in Section 2.2, the efficiency of signal selection in analyses is highly dependent on the spatial coverage and sensitivity of the detector. The *detector acceptance* is a commonly used term to quantify this coverage and is defined for a given event-type as the efficiency to reconstruct that event-type due to the coverage of the detector. To maximise the acceptance,

each sub-detector comprises a central cylindrical barrel region, closed off at each end by end-caps. The acceptance of the calorimeters is particularly important for an accurate measurement of E_T^{miss}, so their coverage is extended as close to the beam pipe in the forward and backward directions as possible. The main subsystems comprise the tracker, the electromagnetic calorimeter, the hadronic calorimeter, the muon spectrometer and the luminosity detectors.

The general requirements for the LHC experiments translate into nominal detector performance goals for the ATLAS detector as reported in Table 2.1.

Detector component	Required resolution	η coverage
Tracking	$\sigma_{p_T}/p_T = 0.05\% \, p_T \oplus 1\%$	$\pm$ 2.5
		($\pm$ 2.0 for the TRT)
EM calorimetry	$\sigma_E/E = 10\%/\sqrt{E} \oplus 0.7\%$	$\pm$ 3.2
		($\pm$ 2.5 for the trigger)
Hadronic calorimetry		
barrel and end-cap	$\sigma_E/E = 50\%/\sqrt{E} \oplus 3\%$	$\pm$ 3.2
forward	$\sigma_E/E = 100\%/\sqrt{E} \oplus 10\%$	3.1 ¡ $\lvert\eta\rvert$ ¡ 4.9
Muon spectrometer	$\sigma_{p_T}/p_T = 10\%$ at $p_T = 1$ TeV	$\pm$ 2.7
		($\pm$ 2.4 for the trigger)

Table 2.1: *Nominal detector performance goals and coverage for the ATLAS detector [19].*

2.3.3 Inner detector

The inner detector [20] is devoted to the measurement of charged particles tracks. This task is essential for the reconstruction of charged particles and momentum measurement, reconstruction of secondary vertices, that are signature of b-quark originated jets and tau leptons, and particle identification. Since the environment at nominal conditions is expected to be very busy the granularity of the detector has to be very fine.

The tracker is the system nearest to the beam pipe, and is immersed in a 2 T solenoidal magnetic field, provided by a solenoid placed around the tracker. The overall dimensions of the tracking system are 2.1 m in diameter and 6.2 m in length. The system consists of three subdetectors: the Pixel Detector, the Semiconductor Tracker (SCT) and the Transition Radiation Tracker (TRT), as is shown in Figure 2.4.

The innermost subdetector is the Pixel detector, which is made up by

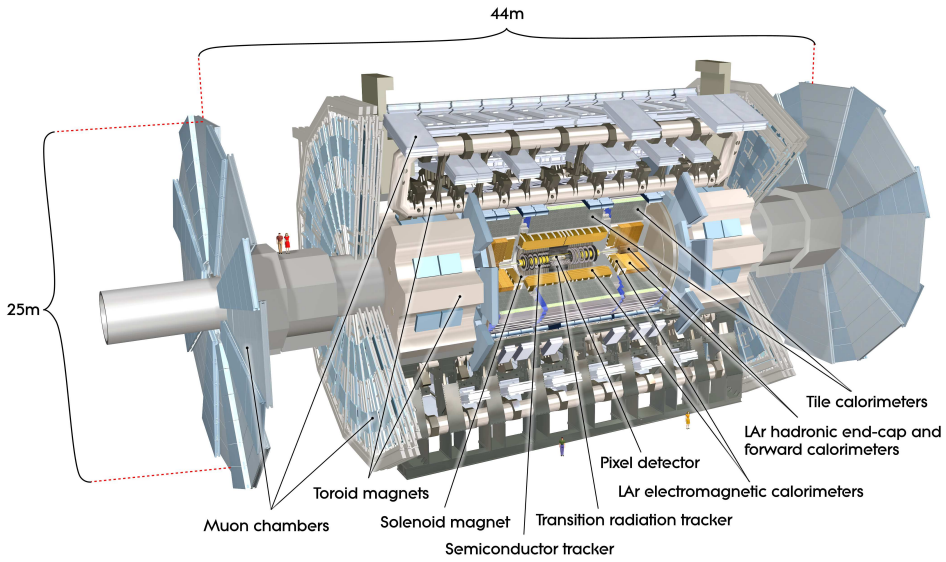

Figure 2.3: *General layout of the ATLAS detector [19].*

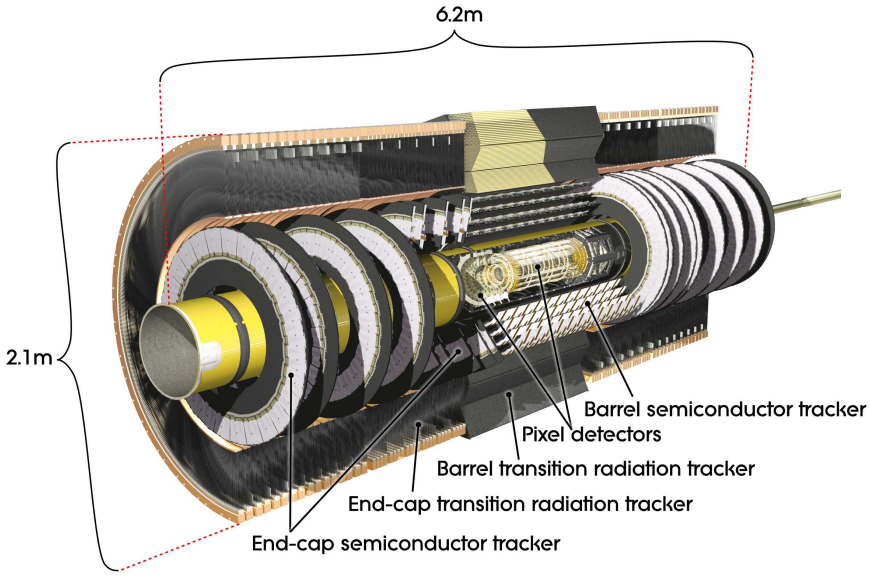

Figure 2.4: *ATLAS inner detector layout [19].*

three cylindrical layers of silicon pixels in the barrel region and three disks in each end-cap. The granularity is very fine, with a pixel size in $R - \phi \times z$

of 50×400 μm^2, allowing for an intrinsic accuracy of 10 μm ($R - \phi$) and 115 μm (η). This detector allows high precision measurements, with three hits per track expected, the inner layer one as close as ~ 2 cm to the beam pipe.
The pixel technology provides very high quality measurements, but its usage is limited to the most internal region, where a better track resolution is needed, by the cost and the enormous number of readout channels, about 80.4 million.

Behind the pixel detector the SCT completes the high precision tracking, with eight hits per track expected. The barrel comprises 4 cylindrical layers of modules of silicon microstrips, each made up by two sensors at a 40 mrad stereo angle in order to measure both coordinates. The pitch of the strip is about 40 μm. The end-cap is made up by 9 disks. The intrinsic accuracies of the SCT are 17 μm ($R - \phi$) and 580 μm (η) and the total number of channels is approximately 6.3 million.

The TRT is made up by 4 mm straw tubes, arranged parallel to the beams in the barrel region and radially in the end-cap. Only $R - \phi$ is provided, with an intrinsic accuracy of 130 μm per straw. A large number of hits per track is expected in this detector, about 36, and the total number of channels is about 351000.

The TRT contributes both to tracking and particle identification. Its tubes are interleaved with layers of polypropylene fibres and foils: a charged particle that passes through the boundary region between materials with a different refraction index emits X-ray radiation whose intensity is proportional to the relativistic γ factor. The TRT works with two threshold levels, the ratio of the high threshold hits versus all the hits can be used to discriminate electrons and pions.

2.3.4 Calorimetry

The calorimeters' purpose is to measure the energy of the particles, together with their direction from their energy deposits. Moreover they limit the punch-through of particles towards the muon system and provide the η coverage crucial for transverse missing energy measurements. The calorimeter is divided into an electromagnetic compartment, dedicated to the measurement of electrons and photons, and a hadronic compartment, suited for jet reconstruction and missing tranverse energy measurements.

The general layout of the calorimetric system is shown in Figure 2.5.

In order to cope with the demanding high luminosity environment, the Electromagnetic Calorimeter (EMCalo) [21] is realised as a lead-LAr (liquid argon) ionization chamber, that has good characteristics in terms of electronic noise, energy resolution, radiation resistance and the possibility

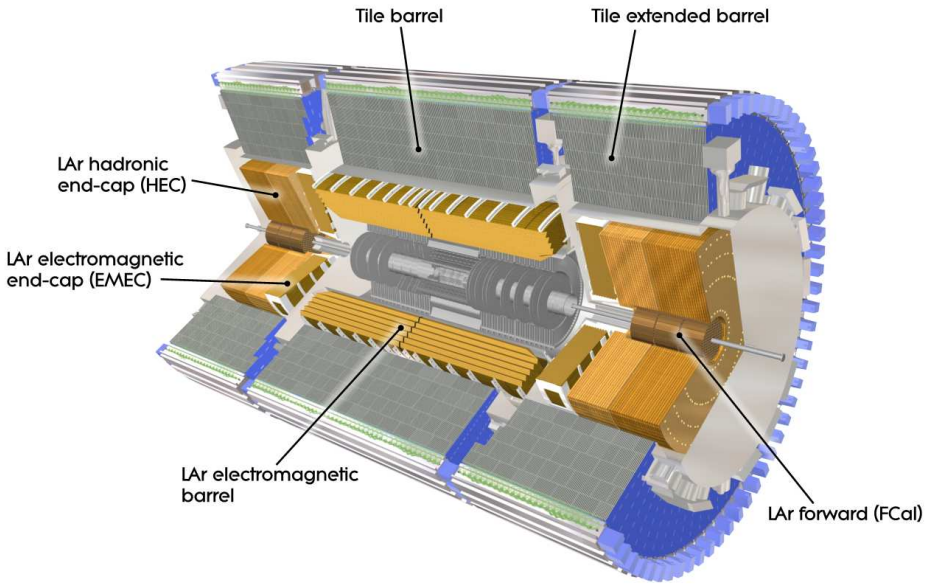

Figure 2.5: *ATLAS calorimetry [19].*

of implementing a high granularity. The EMCalo is divided into two half-barrels (covering the $|\eta| < 1.4$ region) and two end-caps ($1.4 < |\eta| < 3.2$) each subdivided into two coaxial wheels. The region between the barrel and end-cap EM calorimeters, $1.37 < |\eta| < 1.52$, is expected to have poorer performance because of the lack of instrumented material. It is often referred to as crack region. To ensure maximum azimuthal coverage the EMCalo was designed with an accordion geometry: readout electrodes and lead absorbers are laid out radially and folded so that particles can not cross the calorimeter without being detected. The electrodes work as transmission lines as well, so that no dead regions must be introduced.

The barrel is segmented into three regions in depth (strips, middle, back) for a total depth of > 22 radiation lengths. While most of the energy of electrons and photons is collected in the middle, the fine granularity of the strips is necessary to improve the γ-π^0 discrimination and the back measures the tails of highly energetic electromagnetic showers, and helps to distinguish electromagnetic and hadronic deposits. The end-cap inner wheel is segmented in just two regions, for a total depth of > 24 radiation lengths.

The region $|\eta| < 1.8$ is equipped with a presampler, in order to correct for the energy lost upstream in the tracker and in the calorimeter cryostat, that contains the solenoid coil.

The Hadronic Calorimeter is realised with a variety of techniques depending on the region: central, end-cap and forward.

The central region is instrumented with the Tile Calorimeter (Tiles) [22], a sampling steel-scintillator detector. It is divided into a barrel ($|\eta| < 1.0$) and two extended barrels ($0.8 < \eta < 1.7$). There are three segmentations in depth, for a total depth of 9.7 interaction lenghts (at $\eta = 0$). The readout cells in pseudorapidity are pseudo-projective towers towards the interaction region. The Hadronic End-cap Calorimeter (HEC) is a LAr-copper detector, and covers the region, $1.5 < |\eta| < 3.1$, overlapping both with the Tiles and the Forward Calorimeter.

The Forward Calorimeter (FCal) covers the $3.1 < |\eta| < 4.9$ region and is a LAr detector. The absorber material is copper, optimal for electromagnetic measurements, in the first segment in depth, and tungsten for the remaining two segmentats, aimed at the energy measurements of hadrons. Due to the high radiation dose expected in this region, the electrode structure is different from the accordion geometry, consisting of a structure of concentric rods and tubes parallel to the beam axis. The total depth of this subdetector is 10 interaction lengths.

2.3.5 Muon system

Muons are the only particles that can traverse the calorimeters. They are measured by a large air-core muon spectrometer [23], whose layout is shown in Figure 2.6, in order to minimize the effect of multiple scattering.

The large volume magnetic field necessary to bend the particle trajectories is provided by the large barrel toroid in the region $|\eta| < 1.4$, by two smaller end-cap magnets in the $1.6 < \eta < 2.7$ region and by a combination of the two in the transition region ($1.4 < \eta < 1.6$).

There are two different functions that muon chambers must accomplish: triggering and high precision tracking. The trigger system covers the region up to $|\eta| < 2.4$, and is composed by Resistive Plate Chambers (RPCs) in the barrel and Thin Gap Chamber (TGC) in the end-caps. The triggering system provides bunch-crossing identification (BCID), well-defined p_T thresholds and a measurement of the muon coordinate in the direction orthogonal to the chambers dedicated to precision tracking.

The tracking is performed by the Monitored Drift Tubes (MDTs) and by Cathod Strips Chambers (CSCs) at large pseudorapidities. High precision mechanical assembly techniques and optical alignment systems provide the essential alignment of the chambers, while the magnetic field reconstruction relies on Hall sensors distributed throughout the spectrometer volume.

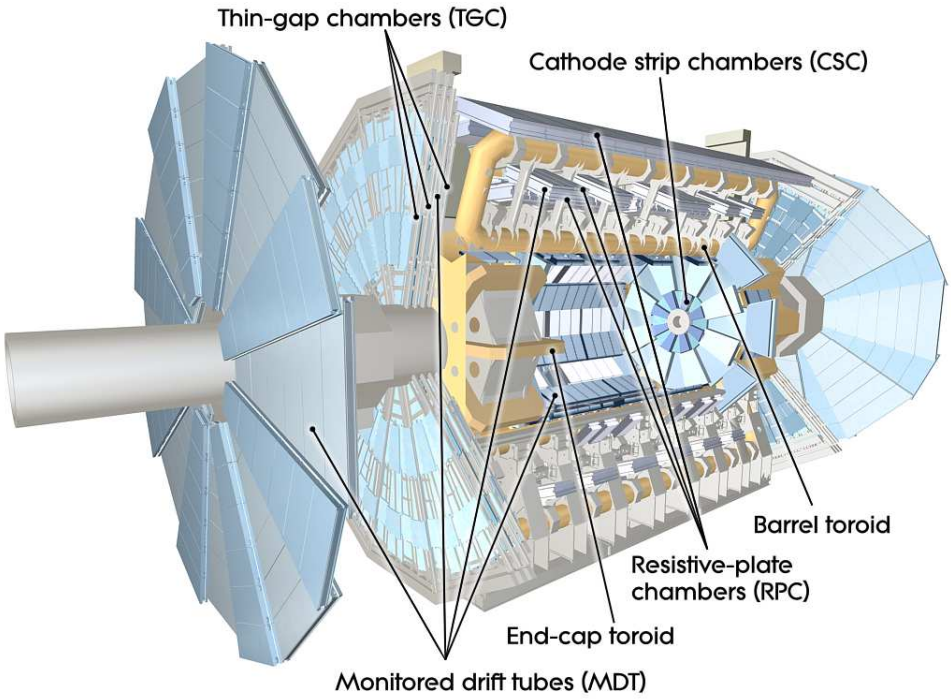

Figure 2.6: *ATLAS muon system [19].*

2.3.6 Luminosity detectors

An essential task for the detector is to determine precisely the luminosity recorded by the experiment. This is accomplished by a set of redundant measurements, taken by three very forward detectors: the LUCID (LUminosity measurement using Cerenkov Integrating Detector), ALFA (Absolute Luminosity for ATLAS) and ZDC (Zero-Degree Calorimeter). The principal monitor is LUCID, that detects inelastic pp scattering events. In addition the Minimum Bias Trigger Scintillators (MBTS), mounted in front of the electromagnetic end-caps, can be used as luminosity detectors in early data analysis, beyond providing a minimum bias trigger signal [24].

Figure 2.7 shows the luminosity delivered by the LHC and collected by ATLAS up to the time this work was written.

2.3.7 Trigger

The ATLAS trigger system must be able to trigger on interesting events while keeping the background rate low in order to cope with the high lumi-

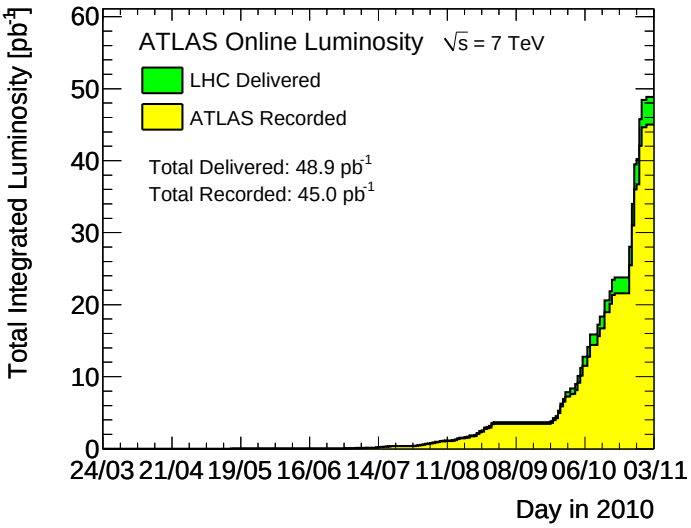

Figure 2.7: *Cumulative luminosity versus day delivered to (green), and recorded by ATLAS (yellow) during stable beams and for 7 TeV centre-of-mass energy. The systematic uncertainty of the luminosity measurement is estimated to be 11% [25, 26].*

nosity, corresponding to a rate of $\sim 10^9$ Hz at nominal conditions, low cross sections of the interesting processes and limited output bandwidth of 200 Hz. The system is implemented in three levels, each step providing a refinement of the decision by more sophisticated algorithms and lower rates. The first level (L1) is hardware-based and makes an initial decision based on timing from an electrostatic beam pick-up (BPTX), coarse detector information from muon trigger chambers and towers of calorimeter cells, together with multiplicity information from the MBTS and very forward detectors. The L1 provides regions of interest (RoIs) to the two further levels, that make up the high level trigger (HLT). The signatures the L1 looks for are high p_T electrons and photons, jets, hadronic tau decays, high values of missing transverse energy. The L1 nominal output rate is $\sim$ 100 kHz. The L1 then passes the RoI information to the High Level trigger, which is composed by the second level trigger (L2) and the Event Filter (EF) and runs on a dedicated processor farm. The L2 examines the RoIs using more detector information than L1, and working in parallel on more RoIs and subdetectors with more complete algorithms. The nominal output rate of L2 is about 1 kHz.

The EF then has access to the complete event and uses reconstruction algorithms similar to the ones used offline. Its output rate is reduced to approximately 200 Hz. The various working trigger chains that make a decision on whether to record an event or not constitute the trigger menu.

Not all the available trigger chains are allowed to make a decision, since some of them have a too high output rate when the luminosity is high. When this happens the trigger chain is prescaled: only a certain fraction of the events that fire the trigger is actually recorded.

2.4 ATLAS reconstruction and performance with early data at 7 TeV

Since E_T^{miss} is calculated from all the energy deposits in the detector, in this section a brief introduction to the ATLAS reconstruction of the different physics objects is presented. Some performance results obtained in early $\sqrt{s} = 7$ TeV collision data are shown as examples of the detector capabilities.

Many early data performance studies rely on minimum bias events (see Section 1.1). These samples are collected triggering with the minimum bias trigger scintillators. Physics analyses instead (apart from soft QCD studies) are based on triggers devoted to the selection of high p_T objects.

2.4.1 Tracking

The reconstruction of tracks is a key ingredient for the reconstruction algorithms of many physics objects, in particular of electrons, muons and taus. Track properties such as TRT hits and the impact parameter provide useful identification information and contain physics information, such as the lifetime of the particle that produced the track.

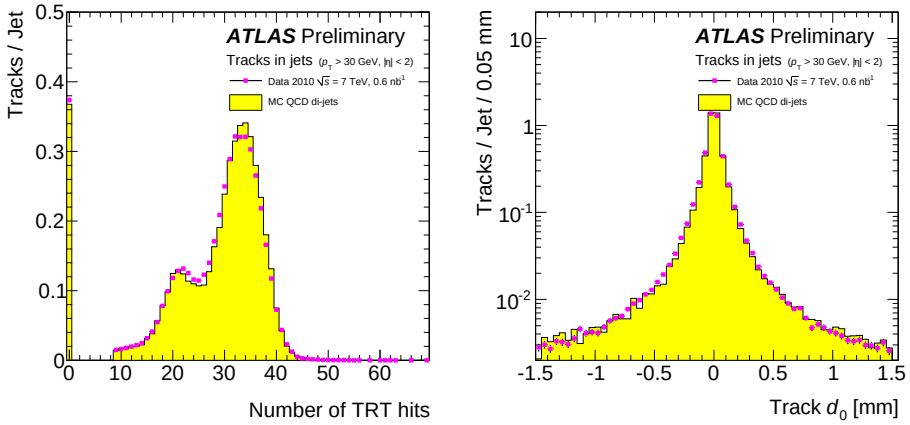

Figure 2.8: *Distribution of the number of TRT hits on tracks and of the transverse impact parameter with respect to the primary vertex for data and di-jet MC events [27].*

Details on the tracking algorithms used in ATLAS can be found in Ref. [28]. The ATLAS tracking algorithms follow an inside-out sequence that starts from seed finding in the silicon layers. The seeds are then used to build roads, within which hits may be found while moving towards the outer edge of the silicon detector. Finally, the search is extended to the TRT and then the collection of hits is fit to obtain the final track parameters.

Figure 2.8 shows the distribution of the number of TRT hits on tracks and of the transverse impact parameter with respect to the primary vertex for 7 TeV data and di-jet MC events. A very good agreement between data and simulation is found for both distributions. A particle passing through the barrel region of the TRT crosses about 35 TRT tubes on its way out. The large peak at zero corresponds to tracks outside the TRT acceptance.

The tracking system provides the reconstruction of vertices, both primary and secondary. The track resolution along the z coordinate is about 100 μm in the pixels and the resolution on the position of the primary vertex is comparable. Therefore the reconstruction of the primary vertex allows to discriminate tracks that come from other interactions in the ~ 5

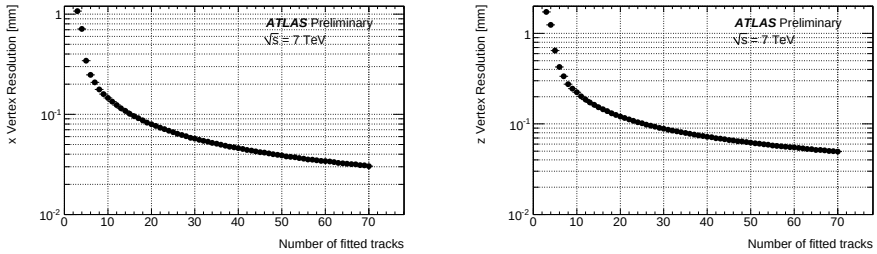

Figure 2.9: *Estimated vertex resolution in x* $\sigma_{x_{\mathrm{PV}},\mathrm{true}}$ *(left) and z* $\sigma_{z_{\mathrm{PV}},\mathrm{true}}$*(right) in 7 TeV data as a function of the number of tracks* N_{trk} *[29].*

cm long interaction region. This is essential in the presence of pileup, since it allows to distinguish objects associated with the primary interaction from superimposed activity.

Figure 2.9 shows the dependence of the vertex position resolutions in x and z on the number of fitted tracks. As expected the errors decrease with increasing values of N_{trk}. The x (z) resolution of the reconstructed primary vertices turns out to be approximately 1-2 mm (about 2 mm) when only two or three tracks are present in the event, since most of these are typically close to the threshold of $p_T > 150$ MeV of a steeply falling distribution, while it approaches 30 μm (50 μm) for 70 tracks. The vertex resolution is expected to improve significantly when moving out from the minimum bias regime to higher track multiplicities.

2.4.2 Electrons and photons

The ATLAS electromagnetic (EM) calorimeter is designed to be able to identify efficiently electrons and photons within a large energy range (5 GeV - 5 TeV), and to measure their energies with a linearity better than 0.5%. In this section, I will focus on the electron reconstruction and identification but similar methods are applied also for photons.

The procedure to measure the energy of an incident electron in the ATLAS EM calorimeter has been described in details in Ref. [12].

A sliding window algorithm [31] is used to identify and reconstruct electromagnetic clusters. Rectangular clusters are formed with a fixed size, in such a way that their position corresponds to the maximum amount of energy deposited inside them (a minimum energy of 3 GeV is required). The optimal cluster size depends on the particle type being reconstructed and the calorimeter region. Electrons need therefore larger clusters than photons

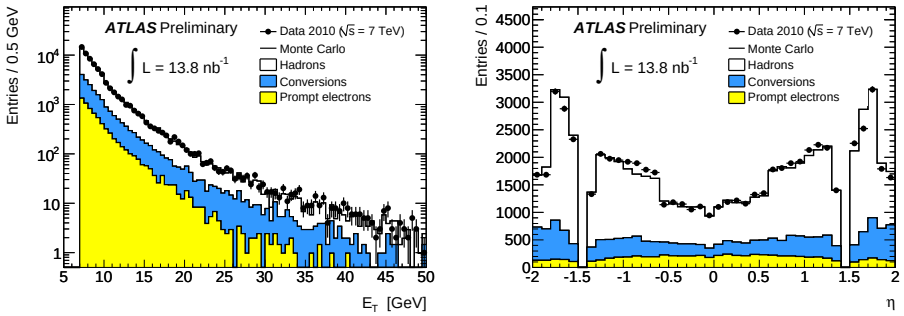

(a) Electron E_T (b) Electron η

Figure 2.10: *Distributions of cluster transverse energy E_T (a) and pseudorapidity η (b), for electron candidates passing the tight identification cuts [30].*

due to their larger interaction probability in the upstream material and also due to the fact that they bend in the magnetic field, radiating soft photons along a range in ϕ. Several series of these kinds of clusters are then built by the reconstruction software, corresponding to different sliding window sizes. These clusters are the starting point of the calibration and selection of electron candidates.

For each of the reconstructed clusters, the reconstruction tries to find a matching track within a $\Delta\eta \times \Delta\phi$ range of 0.05×0.10 with momentum p compatible with the cluster energy E ($E/p < 10$). If one is found, the reconstruction checks for the presence of an associated conversion. An electron candidate is created if a matching track is found while no conversion is flagged. This early classification allows to apply different corrections to electron candidates and is the starting point of a more refined identification based on shower shapes and on respective cuts.

Three levels of electron quality are defined (loose, medium, tight):

- *Loose cuts*: This set of cuts performs a simple electron identification based only on limited information from the calorimeters. Cuts are applied on the hadronic leakage and on shower-shape variables, derived from the middle layer of the EM calorimeter only. This set of cuts provides excellent identification efficiency, but poor background rejection.

- *Medium cuts:* This set of cuts improves the background rejection quality, by adding cuts on the energy deposits in strips in the first layer of the EM calorimeter and on the tracking variables. Strip-based cuts are adequate for $e - \pi^0$ separation. The tracking variables include

the number of hits in the pixels, the number of silicon hits (pixels plus SCT) and the transverse impact parameter. The medium cuts increase the jet rejection by a factor of $3-4$ with respect to the loose cuts, while reducing the identification efficiency by $\sim 10\%$.

- *Tight cuts*: This set of cuts makes use of all the particle identification tools currently available for electrons. In addition to the cuts used in the medium cuts identification,cuts are applied:
  - on the number of vertexing layer hits (to reject electrons from conversions)
  - on the number of hits in the TRT
  - on the ratio of high-threshold hits to the number of hits in the TRT (to reject the dominant background from charged hadrons)
  - on the difference between the cluster and the extrapolated track positions in η and ϕ.

  Two different final selections are available within this tight category: they are named tight (isol) and tight (TRT) and are optimised differently for isolated and non-isolated electrons. In the case of tight (isol) cuts, an additional energy isolation cut is applied to the cluster, using all cell energies within a cone of $\Delta R < 0.2$ around the electron candidate. This set of cuts provides, in general, the highest isolated electron identification efficiency and the highest rejection against jets. The tight (TRT) cuts do not include the additional explicit energy isolation cut, but instead apply tighter cuts on the TRT information to further remove the background from charged hadrons.

The distributions of cluster transverse energy E_T and pseudorapidity η for electron candidates passing the tight identification cuts are shown in Figure 2.10 while the fraction of TRT high-threshold hits on tracks as a function of the relativistic γ factor is shown in Figure 2.11, both in the context of the inclusive electron analysis. The agreement of Monte Carlo with data is found to be good.

To calibrate the electron signal Monte Carlo based methods are used. They correct for the energy deposited in the material in front of the calorimeter, calibrate the cluster energy deposited in the calorimeter and correct for leakage outside the cluster (lateral leakage) and beyond the calorimeter (longitudinal leakage). The four terms are parametrised as a function of the cluster measured signals in the presampler (where present) and in the three accordion longitudinal layers. The parameters are computed at each pseudorapidity value corresponding to the centre of a middle cell and stored in a database [32, 33].

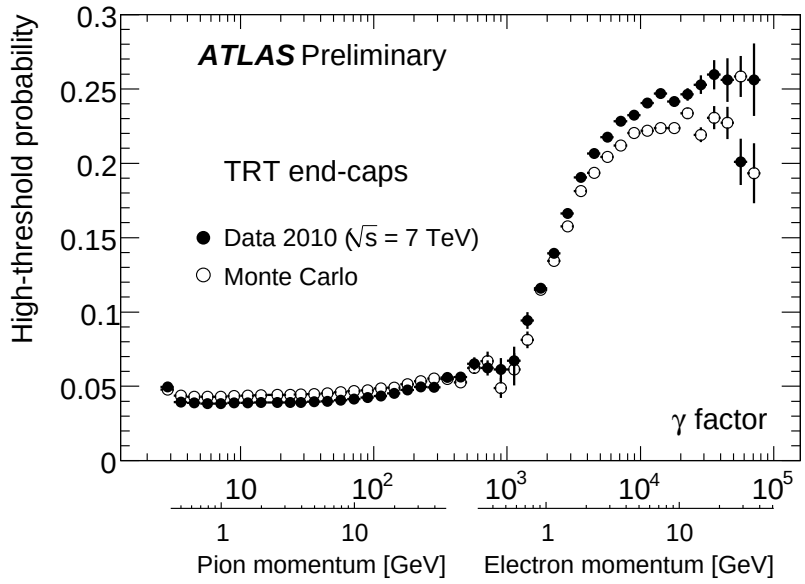

Figure 2.11: *The fraction of TRT high-threshold transition radiation hits over all TRT hits as a function of the relativistic γ factor for data and Monte Carlo in the context of the inclusive electron analysis [30].*

Pure samples of electrons can be selected in the context of physics analyses. The first source of electrons visible in ATLAS was the decay of the J/Ψ meson, whose invariant mass was reconstructed despite the challenges introduced by the low p_T of the electrons, for which ATLAS is not optimised. Then electrons from the Z boson decay have been studied and used for calibrations. Figure 2.12 shows the J/Ψ invariant mass in the top plot and the Z invariant mass in the bottom plot.

2.4.3 Muons

Many physics processes at the LHC are accessible only through the detection of highly energetic muons, due to the overwhelming QCD background. The muon signature in fact is very clean.

The reconstruction of muons is based on information from the Muon Spectrometer, Inner Detector and calorimeters. Different kinds of muon candidates are built, depending on how the detector information is used in reconstruction.

`Stand-alone` muons are reconstructed starting from muon spectrometer hits that are combined into segments to form a track. The muon momentum

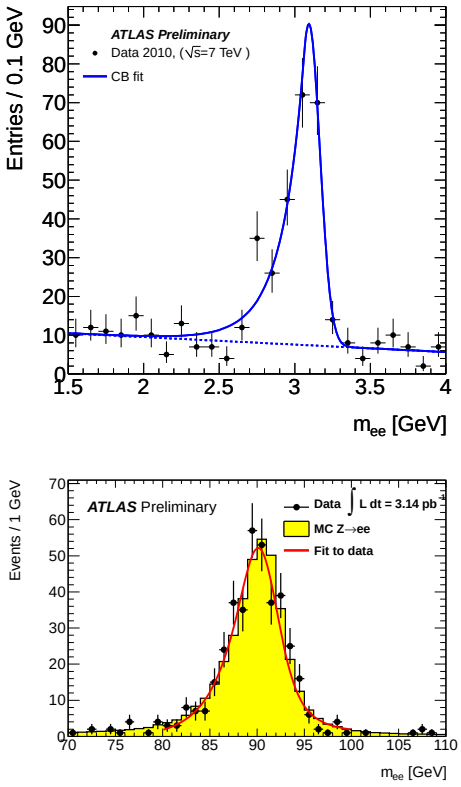

Figure 2.12: *(top) Invariant J/Ψ mass measured with an integrated luminosity of 77 nb^{-1} [34]; (bottom) Invariant Z mass for electron pairs with $|\eta| < 1.37$ [35].*

measured using this track is corrected for the parametrised energy loss of the muon in the calorimeter, to obtain the muon momentum at the interaction point. The track is extrapolated back to the beam axis to obtain the η and ϕ coordinates of the muon and the impact parameter with respect to the interaction point.

`Combined` muons are built starting from stand-alone muons combined with an inner detector track. The information regarding the direction of flight and impact parameter is provided by the muon trajectory in the inner detector.

`Segment tagged` muons are reconstructed using as a seed an inner detector track. The reconstruction algorithms then search for track segments in the precision muon chambers that can be associated to the inner detector track extrapolated to the muon spectrometer.

`Calorimeter tagged` muons are built starting from an inner detector track. The track is identified as a muon if energy depositions compatible with the minimum ionising particle hypothesis can be associated to it.

Muons can be reconstructed by different algorithms. This provides a useful redundancy, but care must be taken in order to avoid overlaps at reconstruction level by not recording stand-alone muons that have been successfully combined, and by flagging just one muon as `BestMatch` when a stand-alone muon matches more than one inner detector track. Overlaps between the tagged and combined muons are removed by combining candidates that share the same inner detector track.

In the early data analysis ATLAS uses two different chains to evaluate the muon performance in detail, `STACO` [36] and `MuId` [37]. These chains correspond to different sets of algorithms that build the classes of candidates listed above.

Both muon combination algorithms create combined tracks out of pairs of muon-only and inner-detector-only tracks. To do this, a match χ^2 is used and corrections are made for energy loss in the calorimeter, however how they handle the combined track differs slightly:

- `STACO` does a statistical combination of the track vectors to obtain the combined track vector
- `MuId` re-fits the combined track, starting from the ID track and then adding Muon measurements

The muon reconstruction performance was preliminarily studied with 0.6 nb^{-1} equivalent minimum bias events, just comparing basic reconstruction quantities with the Monte Carlo simulation [39]. Detector efficiencies, hit multiplicities, muon isolation, and residual distributions of reconstructed muon tracks were measured and found to be well reproduced by the Monte Carlo simulation.

With an integrated luminosity of 17 nb^{-1} further studies were possible [40]. The most abundant background to prompt muons, due to pion decays in flight was estimated using a technique that exploits a large set of exclusively identified $K^0_S \to \pi^+\pi^-$ decays in the inner detector. The pion decay-in-flight probability for combined `STACO` muons is found to be (0.070 $\pm$ 0.012)%. A good level of agreement between data and simulation was found for all of these measurements.

The capability of the ATLAS detector to reconstruct muons on a wide p_T range is illustrated in Figure 2.13, where the di-muon spectrum is shown. The resonances down to ρ and up to Z are evident.

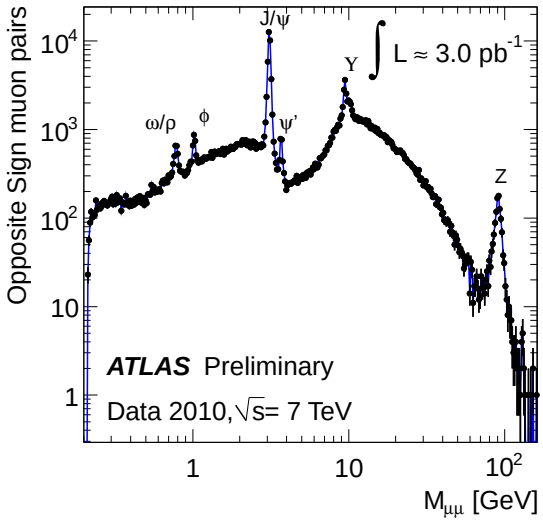

Figure 2.13: *Di-muon invariant mass spectrum for data, from combined opposite sign muons [38]. Peaks corresponding to various resonances are evident.*

2.4.4 Hadronic signals in ATLAS: jets and τ-jets

Hadronic particles in ATLAS deposit their energies mainly in the calorimeter system. As described in Section 2.3.4, the ATLAS calorimeters have a high granularity (about 187000 cells independently read-out) and a high particle stopping power over the whole detector acceptance ($|\eta| < 4.9$). This calorimeter features together with many others described in previous sections allow a high quality jet reconstruction in the challenging environment of the proton-proton collisions at the LHC.

In the following the jet reconstruction techniques are briefly described.

Jet input objects

Cells provide many informations: energy, time, quality, and gain. They are primarily set at the so-called *electromagnetic* scale (EM), as it has been determined by electron test beams and simulations. This energy scale accounts correctly for the energy of electrons and photons. ATLAS calorimeters are not compensating so EM showers generate larger signal than hadrons depositing the same energy, therefore a specific correction for hadronic signals is needed.

Individual cell signals are hard to use because they can be negative due

to noise effects and because it is difficult to determine the source of the signal without signals from neighbours.

Cells have thus to be collected into larger objects like towers or clusters.

- **Calorimeter towers**
  In case of the towers, the cells are projected onto a fixed grid in pseudo-rapidity (η) and azimuth (ϕ). The tower bin size is $\Delta\eta \times \Delta\phi = 0.1 \times 0.1$ in the whole acceptance region of the calorimeters, i.e. in $|\eta| < 4.9$ and $-\pi < \phi < \pi$, with $100 \times 64 = 6.400$ towers in total. Projective calorimeter cells which completely fit inside a tower contribute their total signal to the tower signal. Non-projective cells and projective cells larger than the tower bin size contribute a fraction of their signal to several towers, depending on the overlap fraction of the cell area with the towers.

  Thus, the tower signal is the sum of possibly weighted cell signals (all cells are included). As the cell signals are on the basic electromagnetic energy scale, the resulting tower signal is on the same scale. No further corrections or calibrations are applied at this stage.

- **Topological clusters**
  The alternative representation of the calorimeter signals for jet reconstruction are topological cell clusters, which are basically an attempt to reconstruct three-dimensional energy deposits representing the showers developing for each particle entering the calorimeter. The clustering starts with seed cells with a signal-to-noise ratio, or signal significance $\Gamma = E_{cell}/\sigma_{noise,cell}$, above a certain threshold S, i.e. $|\Gamma| > S = 4$. All directly neighbouring cells of these seed cells, in all three dimensions, are collected into the cluster. Neighbours are considered for those added cells which have Γ above a certain secondary threshold N ($|\Gamma| > N = 2$). Finally, a ring of guard cells with signal significances above a basic threshold $|\Gamma| > P = 0$ is added to the cluster as shown in Figure 2.14. After the initial clusters are formed, they are analysed for local signal maximums by a splitting algorithm, and split between those maximums if any are found.

Jet algorithms

The main common feature of all jet finder implementations in ATLAS is the full four-momentum recombination whenever the constituents of a jet change, either through adding a new constituent, or by removing one, or by changing the kinematic contribution of a given constituent to the jet. Also, in the ATLAS reconstruction software framework ATHENA, the same

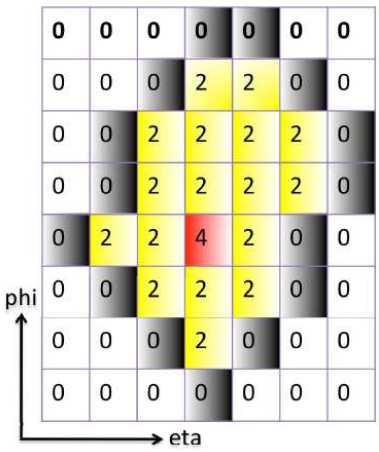

Figure 2.14: *Topocluster schematic representation.*

jet finder code can be run on objects like calorimeter signal towers, topological cell clusters in the calorimeters, reconstructed tracks, and generated particles and partons.

Many algorithms have been used or proposed for defining jets. In this section the two most important techniques are described: cone algorithms and recursive recombination cluster algorithms [41].

- **Cone algorithms**
  The term *Cone Algorithm* is applied to the wide range of jet algorithms which broadly aim to maximise energy (or p_T) in a geometric cone.

  R_{cone} is defined by the following formula :

  $$R_{cone} = \sqrt{\Delta\eta^2 + \Delta\phi^2} \tag{2.2}$$

  where R_{cone} is an indicative quantity for the size of the formed jet. It actually refers to the resolution in (η, ϕ) that a jet algorithm has in order to reconstruct a jet. Two jets that have a distance lower than R_{cone} will finally reconstructed as one jet. The typical default values used in ATLAS are $R_{cone} = 0.4$ and $R_{cone} = 0.6$.

  Figure 2.15 illustrates an example of a different R_{cone} value in the jets algorithms. The two arrows correspond to the (η, ϕ) directions of two jets and the cones correspond to the reconstructed jets. At the left, a jet algorithm with a smaller R_{cone} is used so the two jets are well separated, while is not the case for the image at the right where R_{cone} has a higher value.

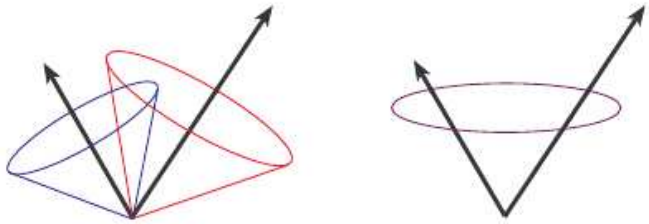

Figure 2.15: *Jet reconstruction algorithms using different R_{cone} values. (left) A jet algorithm with a smaller R_{cone} can discriminate between 2 jets that are found close in ΔR while (right) only one jet is reconstructed in the case of a higher R_{cone}.*

Most frequently used cone algorithms are *iterative*, meaning that when a candidate cone is identified, its momentum vector is calculated and the cone is redrawn around the new centre. The process is repeated until it converges on a stable cone. Figure 2.16 illustrates the different two inputs (towers or clusters) to cone jet algorithm with $R_{cone} = 0.7$. It refers to a QCD event of 4 jets in the final state.

- **Cluster algorithms**
  The *Cluster Algorithms* are based upon pair-wise clustering of the initial constituents. In general, the algorithms define a distance measure between objects, and also some condition upon which clustering should be terminated.

  Two distances are introduced: d_{ij} between entities (particles, pseudojets) i and j and d_{iB} between entity i and the beam (B). The (inclusive) clustering proceeds by identifying the smallest of the distances and if it is a d_{ij} recombines entities i and j, while if it is d_{iB}, calling i a jet and removing it from the list of entities. The distances are recalculated and the procedure repeated until no entities are left.

  The quantities, d_{ij} and d_{iB} are evaluated as follows:

$$d_{ij} = min(k_{ti}^{2p}, k_{tj}^{2p}) \frac{\Delta_{ij}^2}{R^2} \tag{2.3}$$

$$d_{iB} = k_{ti}^{2p} \tag{2.4}$$

  where

$$(\Delta)_{ij}^2 = (y_i - y_j)^2 + (\phi_i - \phi_j)^2 \tag{2.5}$$

  and k_{ti} , y_i and ϕ_i are respectively the transverse momentum, rapidity and azimuth of particle i. In addition to the usual radius parameter

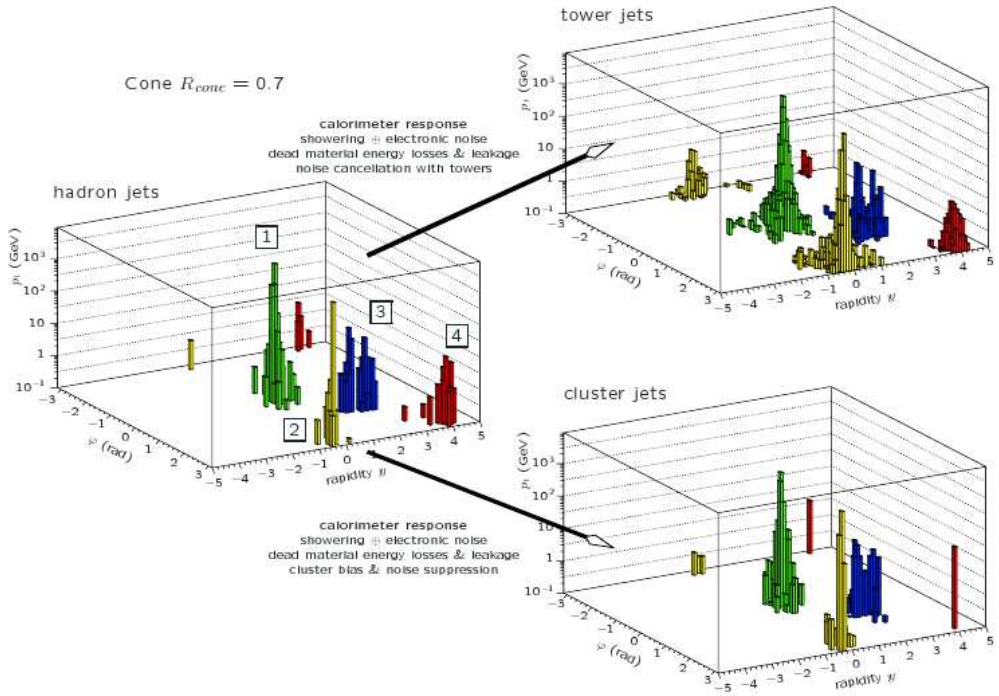

Figure 2.16: *A simulated QCD event with four jets in the final state, as seen at particle level and in the ATLAS calorimeters when using towers or clusters [11].*

R, the parameter p governs the relative power of the energy versus geometrical (Δ_{ij}) scales. For large values of R, the d_{ij} are smaller, and thus more merging takes place before jets are complete.

Three cluster algorithms are considered here: k_T, Cambridge/Aachen, $Anti - k_T$. They basically differ for the value of the parameter p.

– For the k_T **algorithm** [42], the parameter p in Equation 2.4 is taken as $p = 1$. This means that objects with low relative k_T are merged first. In some sense this mimics and inverts the splitting within a parton shower, which tend to be strongly ordered in k_T or a related variable such as angle. This also means that within a jet the final merge is the hardest, and this information can be exploited to interrogate the substructure of the jets, looking for scales associated with the decays of massive particles. Note that if the k_T of an object with respect to the beam is lower than its k_T relative to anything else (divided by R), it will not be merged

any further. Thus soft objects are either merged with nearby hard objects, or left alone with low p_T. In the latter case, they will not be selected by a hard jet p_T cut, and so are ignored.

- For the **Cambridge/Aachen algorithm** [43], $p = 0$ in Equation 2.4. This means that the k_T of the objects is irrelevant in the clustering, and objects near to each other in ΔR are merged first. Thus within a jet the final merge is the most distant, and this information can be exploited to interrogate the substructure of the jets, removing small and peripheral subjets to improve the single-jet mass resolution.
- For the $Anti - k_T$ **algorithm** [44], $p = -1$ in Equation 2.4. This means that in the vicinity $\Delta R < R$ of a hard object, all softer objects will be merged with the harder object in order of their closeness in ΔR. Thus the jet boundary is unaffected by soft radiation. If two comparably hard objects are within $R < \Delta R < 2R$ of each other, energy will be assigned to one of them depending upon their relative k_T and distance. For hard objects within $\Delta R < R$ of each other, a single jet will be formed containing both hard objects and the soft objects within their vicinity. The ordering of the merging is not meaningful for this algorithm. However, the constituents may be reclustered using one of the other algorithms to recover subjet information.

In ATLAS $Anti - k_T$ has been adopted as default with $R = 0.4$ or $R = 0.6$.

Figure 2.17 shows the jet p_T distributions in Monte Carlo simulation and data for jets reconstructed using topological clusters as well as towers and the $Anti - k_T$ algorithm with $R = 0.6$.

Jet Calibrations

ATLAS has developed several calibration schemes with different levels of complexity and different sensitivity to systematic effects, which make them complementary in how they contribute to the understanding of the jet energy measurement:

- **Simple p_T and $\eta-$dependent calibration scheme (EMJES calibration)**. Reconstructed jets are calibrated based on the energy scale reconstructed by the calorimeters, the EM scale. As already said this energy scale accounts correctly for the energy of photons and electrons, but it does not correct for instrumental (detector) effects such as calorimeter non-compensation, energy losses in inactive detector regions, particles not totally contained in the calorimeter, particles that fall

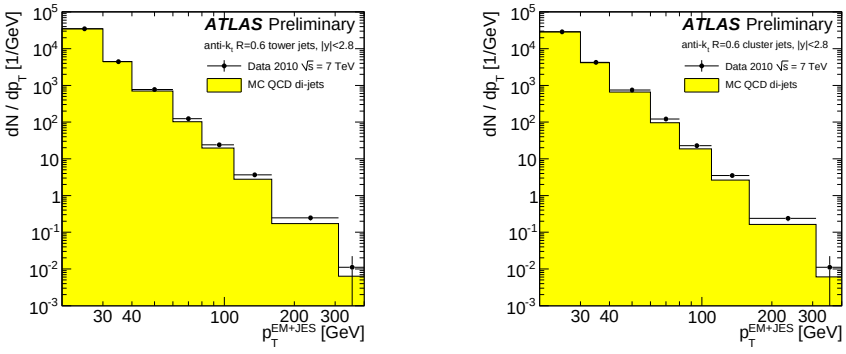

Figure 2.17: *Transverse momentum (p_T) distributions using the Monte Carlo−based p_T and η jet calibration for (left) towers and (right) topoclusters input constituents.[45]*

out of the reconstructed jet but are included in the true jet and finally inefficiencies in calorimeter clustering and jet reconstruction.

The goal of the Jet Energy Scale (JES) calibration, here called EMJES because it is applied on top of the EM scale, is to correct the energy and momentum of the jets measured in the calorimeter, using as a reference the kinematics of the corresponding Monte Carlo truth jets.

The jet p_T response for a reconstructed jet is defined as the ratio between the transverse momentum of the particle jet from the Monte Carlo event generator ($p_T^{MC\ truth\ jet}$) and the transverse momentum of the reconstructed calorimeter jet after the JES calibration (p_T^{jet}), and it is denoted as $R = p_T^{jet}/p_T^{MC\ truth\ jet}$.

The jet energy scale calibration is derived as a global function depending on η and p_T. This function is used to restore the jet response to unity, therefore correcting the energy of the jet to a hadronic scale, starting from the jet response at the electromagnetic scale:

$$R^{EM} = p_T^{jet,EM}/p_T^{MC\ truth\ jet} \tag{2.6}$$

The jet energy response is calculated in the simulation by matching reconstructed calorimeter jets to particle level jets within a cone of $\Delta R = 0.3$ around the jet axis.

The determination of the jet energy scale calibration consists of three steps. Firstly, the jet energy response at the EM scale of Equation 2.6 is determined in fixed $p_T^{MC\ truth\ jet}$ bins. The mean of the jet response, determined by a Gaussian fit to R^{EM} in each $p_T^{MC\ truth\ jet}$

bin, is considered as the average jet response at the centre of this bin. In a second step the jet response, measured as a function of truth transverse momentum $p_T^{MC\ truth\ jet}$, is transformed to the jet response as a function of the reconstructed jet transverse momentum with an inversion techinque, i.e. estimating the average reconstructed $p_T^{jet,EM}$ in each $p_T^{MC\ truth\ jet}$ bin using the jet response definition:

$$p_T^{jet,EM} = R^{EM}(p_T^{MC\ truth\ jet}, \eta) \cdot p_T^{MC\ truth\ jet}. \tag{2.7}$$

After the inversion, the resulting response is a function of reconstructed quantities only ($R^{EM}(p_T^{jet,EM}, \eta)$) and it is parameterised using the function:

$$R^{EM}(p_T^{jet,EM}, \eta) = \sum_{i=0}^{4} \frac{a_i(\eta)}{(ln(p_T^{jet,EM}[GeV]))^i} \tag{2.8}$$

where $a_i(\eta)$ are free parameters for the fit to the parameterization of the response. The JES correction is therefore defined as the inverse of the response function defined in Equation 2.8 and applied inclusively to all jets. The calibrated transverse momentum of the jet is then calculated as:

$$p_T^{jet} = 1/(R^{EM}(p_T^{jet,EM}, \eta)) \cdot p_T^{jet,EM}. \tag{2.9}$$

The JES calibration can be applied not only to EM scale jets but also on top of global calibrated jets.

EMJES is the only ATLAS calibration for which systematic uncertainties have been calculated so far. Systematics are due to dead material in the low p_T region, to uncertainty on calorimeters energy scale calculated from test beams, on simulation of the hadron showers in calorimeters and on MC event generator description of fragmentation and UE.

The JES correction will also be evaluated in-situ from data using γ+jet and di-jet balance techniques.

- **Global cell energy-density weighting calibration scheme (GCW calibration)**. This calibration scheme attempts to compensate for the different calorimeter response to hadronic and electromagnetic energy depositions in the calorimeters. The hadronic signal is characterised by low cell energy densities and, thus, scaled up. The weights, which depend on the cell energy density and location only, are determined by minimising the energy fluctuations between the reconstructed and

particle jets in Monte Carlo simulation. The weights also compensate for energy losses in the dead material. Jets are found from uncalibrated clusters or towers, then cells are weighted and a final p_T- and η-dependent correction is added to ensure that the jet energy is properly reconstructed.

- **Local cluster weighting calibration scheme (LCW calibration).** This calibration scheme uses properties of clusters to calibrate them individually. These weights are determined from Monte Carlo simulations of charged and neutral pions. Jets are found from calibrated clusters and a final correction of the jet energy is applied to account for jet-level effects (e.g.: particles in the jet not reaching the calorimeter).

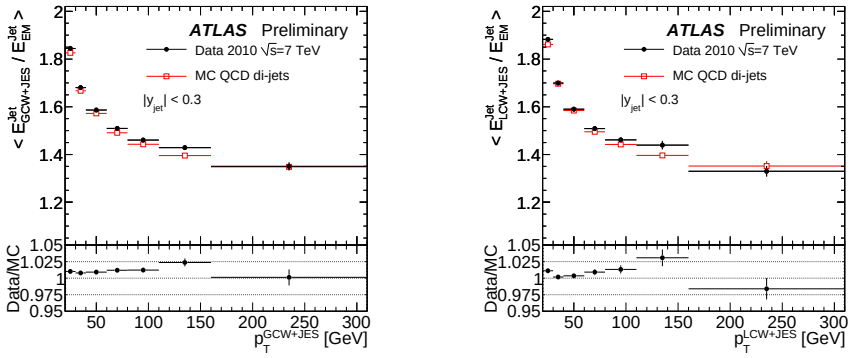

Figure 2.18: *Mean calibrated jet energy over uncalibrated jet energy as a function of calibrated jet p_T for jets constructed of topological clusters calibrated with (left) the global cell energy-density weighting and (right) local cluster weighting calibration schemes. The mean value is shown as obtained in data (black points) and in Monte Carlo simulation (red open squares).[45]*

Figure 2.18 shows the mean of the ratio of calibrated over uncalibrated jet energies as a function of calibrated jet p_T for the GCW and LCW calibration schemes for jets with rapidity $|y_{jet}| < 0.3$. In the Monte Carlo, both calibrations apply the same correction factors on average, indicating that they all calibrate jets correctly. The agreement between the factors applied in the data and the Monte Carlo simulation is better than 2%.

τ-jets

The reconstruction of tau leptons in ATLAS focuses on hadronic decay channels, since it is impossible to distinguish muons and electrons from tau decays

from prompt ones (the relative branching ratios are given in Section 1.2.2). The dominant hadronic decay channels are characterised by the presence of pions, both charged and neutral, in the final state. Hadronic decays can be distinguished in 1-prong and 3-prong decays, that is with one or three charged particles in the final state. Down to an energy of the tau of 10 GeV, the γ factor is > 5, therefore hadronic tau decays typically show up in the detector as collimated jets of hadrons, in particular pions, with a limited number of associated tracks (τ-jet).

Since hadronic tau decays have a complex topology both tracking and calorimeter information is exploited in the reconstruction.

There are two algorithms to reconstruct a τ-jet:

- `tauRec` is a calorimetry-based algorithm that starts from clusters reconstructed in the hadronic and electromagnetic calorimeters and builds the identification variables based on information from the tracker and the calorimeter.

- `tau1p3p` is a track-based algorithm that starts from seeds built from few (low multiplicity) high quality tracks collimated around the leading one. The energy is calculated with an energy-flow algorithm based only on tracks and the energy in the electromagnetic calorimeter. All identification variables are built using information from the tracker and the calorimeter.

Tau candidates can also be reconstructed by both algorithms as well, when a seed track and a seed jet are within a distance $\Delta R < 0.2$. In this case both-seeded candidates are built, with the transverse energy information coming from `tauRec` and the (η, ϕ) position, the number of associated tracks and the charge from `tau1p3p`. The reconstruction of τ-jet candidates provides small background rejection only in the case of `tau1p3p`, and none in case of `tauRec`. A further identification step is necessary in order to improve this feature.

Identification is based on several discriminating variables. From a physics point of view they can be grouped into shower width, particle multiplicity and shower composition variables. From a detector perspective the identification variables can be calorimeter cell-based, calorimeter cluster-based, tracking or tracking-calorimeter combined variables. The many possible variables are eventually combined into multivariate discriminants, such as likelihoods and boosted decision trees.

With the first 15 nb^{-1} of integrated luminosity it was possible to study the performance of the tau reconstruction and identification just for QCD final states, since almost no genuine taus are expected in such a small sample. These studies are summarised in [46, 47]. Identification variables were

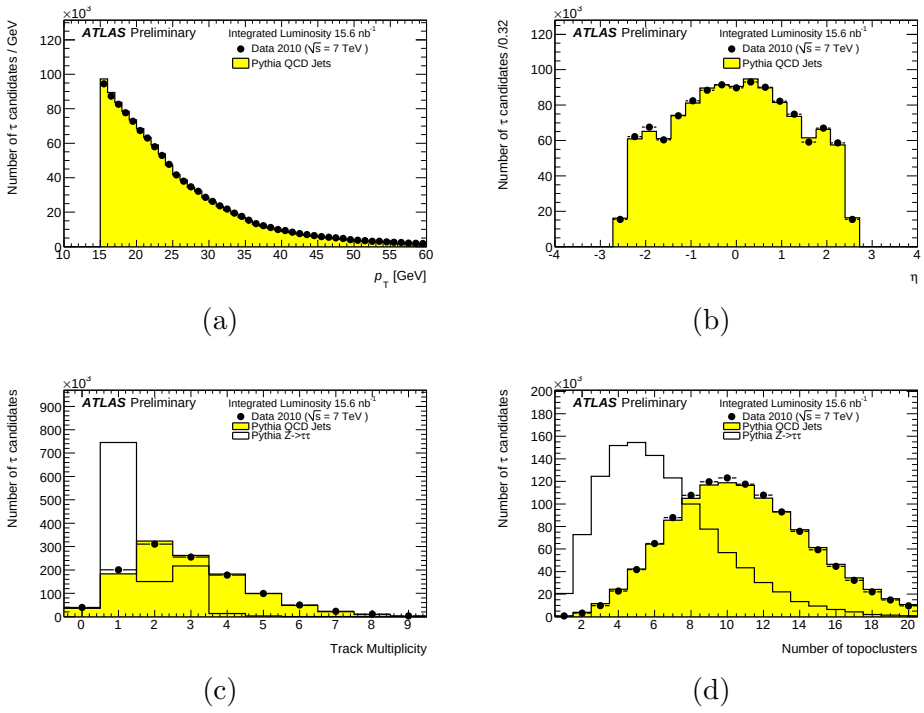

Figure 2.19: (a) Transverse momentum, (b) pseudorapidity, (c) number of associated tracks and (d) number of associated topoclusters of τ candidates in a di-jet selection of 7 TeV data and QCD di-jet Monte Carlo. The Monte Carlo is normalised to data. Superimposed the shape for $Z \rightarrow \tau\tau$ Monte Carlo events is shown as well [46].

compared with Monte Carlo prediction. The overall agreement was found to be fair, even tough some discrepancies were noticed. Figure 2.19 shows the p_T, η, number of associated tracks within $\Delta R < 0.2$ and the number of topoclusters of tau candidates for data and QCD di-jet Monte Carlo. The agreement of the two distributions is good. Also $Z \rightarrow \tau\tau$ Monte Carlo simulation is shown in the bottom plots for comparison.

The tau calibration currently relies on Monte Carlo and is done in two steps:

- First, the GCW calibration scheme (see Section 2.4.4 for details) is used on the calorimeter cells belonging to the tau candidate in order to improve the energy resolution.
- Second, the energy is shifted by a factor that is a discrete function of E_T , η and the number of tracks to restore the tau energy scale to the true energy.

The derivation of the tau calibration fudge factors is done through the following procedure:

- The signals samples like $Z \rightarrow \tau\tau$, $H \rightarrow \tau\tau$, $A \rightarrow \tau\tau$ samples are reconstructed without the calibration factors, obtaining the invariant mass using $E_{\mathrm{T}}^{miss,\mathrm{True}}$ (see Section 3.1.3).
- Taus that can be matched to their truth counterparts are selected, and $E_{T,truth,visible}/E_{T,reco}$ for each of those taus is calculated.
- $E_{T,truth,visible}/E_{T,reco}$ is plotted in different ranges of E_T reco and η reco. Candidates are also separated in 1 track or 2-3 tracks taus.
- A Gaussian fit is performed on those histograms, limiting the fitted range to 2σ around the mean of the histogram. The mean of the fit is the calibration factor. These factors must therefore restore the invariant mass peak to the correct value.

The implementation of an alternative method similar to the JES correction based on the numerical inversion technique (NI) is ongoing at the time of writing.

Chapter 3

Missing transverse energy measurement in ATLAS

As described in Chapter 1, a very good measurement of the missing transverse energy (E_T^{miss}) in terms of linearity and resolution and the absence of tails is essential for many physics studies in ATLAS.

This chapter describes the algorithms used for E_T^{miss} reconstruction in ATLAS, from the simplest to the most refined one. Then the performance of the first E_T^{miss} measurement with ATLAS real data, at $\sqrt{s} = 900$ GeV, 2.36 TeV and 7 TeV, is reported.

3.1 Reconstruction of E_T^{miss}

The missing transverse energy in ATLAS is primarily reconstructed from energy deposits in the calorimeter and reconstructed muon tracks. Apart from the hard scattering process of interest, many other sources, such as the underlying event, multiple interactions, pileup and coherent electronics noise, particles not coming from the LHC collisions lead to energy deposits and/or muon tracks. As already said the ATLAS calorimeters are non-compensating, thus classifying the energy deposits into various types (e.g. electrons or jets) and calibrating them accordingly is the essential key for an optimal E_T^{miss} measurement. In addition, the loss of energy in dead regions and readout channels make the E_T^{miss} measurement a real challenge.

The E_T^{miss} reconstruction algorithm starts from the energy deposits in calorimeter cells that survive a noise suppression procedure. The cells can be calibrated using global calibration weights depending on their energy density. This procedure is found robust already at initial data taking because it does not rely on other reconstructed objects. In a subsequent step, the cells

can be calibrated according to the reconstructed object they are assigned to. Corrections are applied for the muon energy and for the energy lost in the cryostat.

Summarising missing transverse energy is defined as

$$E_{\mathrm{T}}^{\mathrm{miss}} = \sqrt{(E_x^{\mathrm{miss}})^2 + (E_y^{\mathrm{miss}})^2} \tag{3.1}$$

where E_T^{miss} components include contributions from transverse energy deposits in the calorimeters, corrections for energy loss in the cryostat and measured muons:

$$E_{x,y}^{miss} = E_{x,y}^{miss,\mathrm{Calo}} + E_{x,y}^{miss,\mathrm{Cryo}} + E_{x,y}^{miss,\mathrm{Muon}}. \tag{3.2}$$

- $E_{x,y}^{miss,\mathrm{Calo}}$ are defined as

$$\begin{aligned} E_{\mathrm{x}}^{\mathrm{miss}} &= -\sum_{i=1}^{N_{\mathrm{cell}}} E_i \sin\theta_i \cos\phi_i, \\ E_{\mathrm{y}}^{\mathrm{miss}} &= -\sum_{i=1}^{N_{\mathrm{cell}}} E_i \sin\theta_i \sin\phi_i, \end{aligned} \tag{3.3}$$

  where E_i, θ_i and ϕ_i are the cell energy, polar angle and azimuthal angle respectively. Because of the high granularity of the calorimeter (about 187000 cells), it is crucial to suppress noise contributions to E_T^{miss}, i.e. limit the number of cells, N_{cell}, used in the sum. This is done by only using cells belonging to topoclusters (see Section 2.4.4 for details). In the topoclusters building procedure, cells with only noise and cells flagged as very noisy in the ATLAS database, which represent about 0.1% of the total cells in the calorimeter, are removed.

- $E_{x,y}^{miss,\mathrm{Cryo}}$ are added only in some cases and will be described in Section 3.5.2.

- $E_{x,y}^{miss,\mathrm{Muon}}$ are calculated from the momenta of muons measured in a range of pseudorapidity $|\eta| < 2.7$:

$$E_{x(y)}^{\mathrm{miss},\mu} = -\sum_{\text{selected muons}} E_{x(y)}^{\mu} \tag{3.4}$$

  In the region $|\eta| < 2.5$ only good-quality muons in the muon spectrometer with a matched track in the inner detector are considered. The matching requirement considerably reduces contributions from fake muons, sometimes created from high hit multiplicities in the muon spectrometer in events with very energetic jets (see Section 3.1.3).

  The muon term is calculated in a different way for isolated and non-isolated muons, where non-isolated muons are those within the distance $R = \sqrt{\Delta\eta^2 + \Delta\phi^2} < 0.3$ of a jet in the event.

– The p_T of an isolated muon is determined from the combined measurement of the inner detector and muon spectrometer. In this case the energy lost by the muon in the calorimeters ($E_{x(y)}^{\mathrm{miss,calo},\mu}$) is not added to the calorimeter term.
– For a non-isolated muon, the energy lost in the calorimeter cannot be separated from the nearby jet energy. The muon spectrometer measurement of the muon momenta after energy loss in the calorimeter is therefore used unless there is a significant mis-match between the spectrometer and the combined measurement. In this case the combined measurement minus the parameterised energy loss in the calorimeter is used.

For higher values of the pseudorapidity outside the fiducial volume of the inner detector ($2.5 < |\eta| < 2.7$), there is no matched track requirement and the muon spectrometer is used alone.

Apart from the loss of muons outside the acceptance of the muon spectrometer ($|\eta| > 2.7$), muons are lost in other small regions not covered by the muon spectrometer. The muons reconstructed from the inner detector and calorimeter energy deposits can be used to recover these E_T^{miss} contributions.

Unmeasured, badly measured, or fake muons can be a source of large fake E_T^{miss}, while the muon term has a negligible contribution to the E_T^{miss} resolution (see next Section).

For the muon term both muon algorithms, `STACO` and `MuId` can be used (see Section 2.4.3 for details).

3.1.1 E_T^{miss} resolution

In order to evaluate the E_T^{miss} performance, the E_x^{miss}, E_y^{miss} resolutions as function of the total transverse energy $\sum E_T$ are studied.

The E_T^{miss} resolution, expressed as $\sigma(E_{x,y}^{miss,\mathrm{True}} - E_{x,y}^{miss})$, where $E_{x,y}^{miss,\mathrm{True}}$ and $E_{x,y}^{miss}$ are the true and reconstructed E_T^{miss} components, respectively, approximately follows a stochastic behaviour in its dependence on $\sum E_T$. The true E_T^{miss} ($E_{\mathrm{T}}^{miss,\mathrm{True}}$) is calculated from the particles that interact weakly with the detector. The resolution scales in good approximation as

$$\sigma(E_{x,y}^{miss,\mathrm{True}} - E_{x,y}^{miss}) = a \times \sqrt{\sum E_{\mathrm{T}}}, \tag{3.5}$$

where a is the scale factor indicating the resolution quality level.

Resolution curves have been studied for all the data samples analysed and for all the different calibrations applied. In minimum bias and jets events $E_{x,y}^{miss,\mathrm{True}}$=0 is assumed.

3.1.2 E_T^{miss} linearity

To fully evaluate E_T^{miss} performance the E_T^{miss} linearity has also been studied.

The E_T^{miss} linearity is defined by the following expression:

$$Linearity = (E_{\mathrm{T}}^{miss,\mathrm{True}} - E_T^{miss})/E_{\mathrm{T}}^{miss,\mathrm{True}}, \tag{3.6}$$

where E_T^{miss} and $E_{\mathrm{T}}^{miss,\mathrm{True}}$ are reconstructed and true E_T^{miss}, respectively. This definition of linearity assumes non-zero $E_{\mathrm{T}}^{miss,\mathrm{True}}$ values and that fake E_T^{miss} measurements are small such that the E_T^{miss} angle is well measured.

3.1.3 Fake E_T^{miss}

The reconstructed E_T^{miss} has two constituents, coming one from physics, $E_{\mathrm{T}}^{miss,\mathrm{True}}$ and an other one due to detector inefficiencies and resolution ($E_{\mathrm{T}}^{miss,\mathrm{Fake}}$). For an accurate measurement of E_T^{miss} it is important to have a good understanding of the sources of $E_{\mathrm{T}}^{miss,\mathrm{Fake}}$ in data:

- **Fake E_T^{miss} from muons**
  $E_{\mathrm{T}}^{miss,\mathrm{Fake}}$ from muons can be caused either by inefficiencies in reconstructing a high p_T muon or by reconstructing a fake high p_T muon. The latter could be present due to a combination of a lower p_T muon and/or random hits from high p_T jet punch-throughs from the calorimeter to the muon chambers. Fake muons that are reconstructed from random hits in the muon chambers can be arbitrarily hard and strongly contribute to $E_{\mathrm{T}}^{miss,\mathrm{Fake}}$ but can be suppressed using cuts on the hits in the muon chambers.

- **Fake E_T^{miss} from the calorimeter**
  $E_{\mathrm{T}}^{miss,\mathrm{Fake}}$ in the calorimeter is produced by mis-measurements of hadronic jets, taus, electrons or photons. The calorimeter has cracks and gaps in the transition regions, which are also used for service outlets. These regions have poorer resolution and are expected to give larger contributions to $E_{\mathrm{T}}^{miss,\mathrm{Fake}}$ The majority of the badly measured jets have η pointing to the gap region $1.3 < |\eta| < 1.6$ (see Section 2.3.4).

- **Fake E_T^{miss} from jet leakage**
  Jet leakage from the calorimeters or fluctuations in large jet energy deposits in non-instrumented regions such as the cryostat between the liquid argon and tile calorimeters can also be a source of $E_{\mathrm{T}}^{miss,\mathrm{Fake}}$. Together with jets pointing to crack regions, this is the main source of $E_{\mathrm{T}}^{miss,\mathrm{Fake}}$ in the events presented in this chapter.

- **Fake E_T^{miss} from instrumental effects**
  Every instrumental failure and hardware problem can be a source of $E_{\mathrm{T}}^{miss,\mathrm{Fake}}$. A lot of effort has been done to remove or correct events where energy comes from known problematic regions or cells (see Section 3.2.1).

- **Fake E_T^{miss} from non-collision signals**
  Events not due to the LHC collisions, as cosmic muons, beam halo, beam gas are another source of $E_{\mathrm{T}}^{miss,\mathrm{Fake}}$. They can be suppressed through timing and direction requests.

3.2 Data and Monte Carlo

The results presented in this Chapter have been obtained from 900 GeV, 2.36 TeV and 7 TeV data samples collected during stable periods of *pp* collisions with nominal magnetic field conditions.

For each run only those luminosity blocks (periods corresponding to about two minutes of data-taking) satisfying data quality criteria for inner detector, calorimeters and jet and missing transverse energy reconstruction were analysed [48].

In order to suppress cosmic-ray and beam-related backgrounds, events were required to contain at least one primary collision vertex, defined by at least five reconstructed charged-particle tracks.

Collision events were triggered by the Minimum Bias Trigger Scintillators (MBTS, see Section 2.3.6). Timing criteria based on calorimeter measurements were applied to reject residual beam background by requiring signals from both sides of the detector to coincide within 5 (10) ns in the end-cap calorimeters (MBTS).

The results are shown for 0.3 nb^{-1} of data for minimum bias events and with 14.3 nb^{-1} to 300 nb^{-1} of data containing an enhanced number of high p_T physics objects selected by requiring the Level-1 calorimeter trigger ("L1Calo") to have fired, which indicates a significant energy deposit in a certain region of the calorimeter. In both cases no genuine E_T^{miss} is expected.

Data have been compared to Monte Carlo minimum bias and di-jet events generated using the PYTHIA Monte Carlo program [49]. All Monte Carlo events pass through a full Geant 4 [50] detector simulation with a detailed description of geometry and material. The same trigger and event selection, as described for the data, are applied to the Monte Carlo simulation.

For data events with only one primary vertex are considered in all the figures of Sections 3.3, 3.4, 3.5 and 3.6. Effects due to pileup have also been

studied and are presented in Section 3.9. Monte Carlo events have been simulated with no pileup.

3.2.1 Jet reconstruction and selection

Jets (if any) are reconstructed with the Anti-k_t algorithm (see Section 2.4.4) with a distance parameter $R = 0.6$ and full four-momentum recombination. Three selection criteria are applied to identify jets caused by noise or by out-of-time energy deposition in the calorimeters [48]:

- Fake jets caused by sporadic noise bursts in the HEC are identified by requiring that the fraction of the jet's energy in the HEC is larger than 0.8, and that 90% of jet energy is distributed over less than 6 calorimeter cells. It was observed that this criterion is not working if the HEC burst is overlaid with real energy deposition, so an additional cut is applied based on the correlation between the jet energy fraction in HEC and the jet quality, defined on the base of the fraction of jet energy from LAr calorimeter cells flagged as problematic (low signal quality).
- Fake jets caused by very few noise burst in the electromagnetic calorimeter causing large coherent noise in neighboring cells are identified by requiring the fraction of jet energy from LAr calorimeter cells flagged as problematic to be greater than 0.8, and the fraction of energy in only the electromagnetic calorimeter to be greater than 0.95.
- Jets reconstructed from large out-of-time energy deposits in the calorimeter (for example those due to photons produced by cosmic ray muons overlaid on a minimum bias collision event) are identified if the time of the jet is more than 50 ns different from that of the average event time.

For this study events were rejected if any jet in the event with transverse momentum $p_T > 10$ GeV/c at the electromagnetic scale fell into any of the three categories above.

3.3 Performance of the E_T^{miss} reconstruction at the electromagnetic scale

E_T^{miss} reconstruction performance has been first determined with data at 900 GeV and confirmed later in events at 7 TeV.

Since first data are mainly minimum bias events, the number of muons is very small, the number of jets is also small (therefore the energy deposit

in the cryostat is small as well), thus E_T^{miss} can be reconstructed only with the calorimeters.

In the first step cells were taken at the electromagnetic scale (EM, see Section 2.4.4 for details).

3.3.1 EM scale results in minimum bias events at $\sqrt{s} = 900$ GeV

At $\sqrt{s} = 900$ GeV mainly soft proton-proton collisions occur where no true E_T^{miss} is expected. This is confirmed by the Monte Carlo simulation with minimum bias events and the data. $\sum E_T$ up to 100 GeV are deposited in the calorimeter for minimum bias events in the 900 GeV data.

The E_T^{miss} distribution, shown in Figure 3.1. For $E_T^{miss} \gtrsim 5$ GeV data show a harder spectrum than Monte Carlo simulation.

In simulation, there is an outlier event with E_T^{miss}~30 GeV, which is explained by the presence of a high p_T jet, not balanced since the other jet in the event is poorly reconstructed because of detector acceptance. In data, the two events with E_T^{miss}~30 GeV are traced back to energy deposited in few cells out of time by at least two bunch crossings.

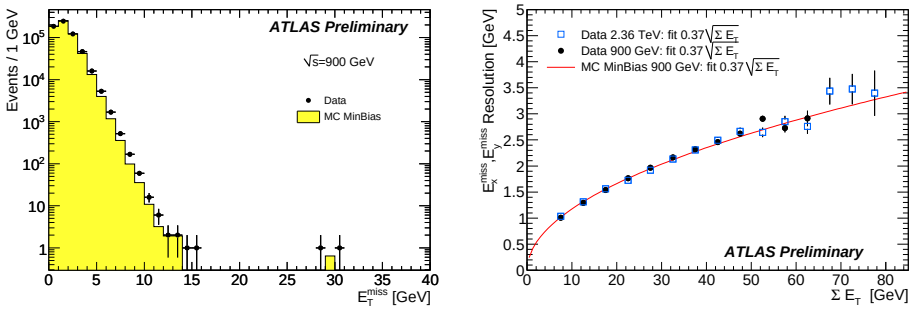

Figure 3.1: *(left) Distribution of E_T^{miss} in minimum bias events (dots) at 900 GeV. The expectation from Monte Carlo simulation is superimposed (histogram) and normalised to the number of events in data. (right) E_x^{miss} and E_y^{miss} resolution as a function of $\sum E_T$.*
The line represents a fit to the resolution obtained in the Monte Carlo simulation and the full dots (open squares) are the results with data at 0.9 (2.36) TeV [51].

A more quantitative evaluation of the E_T^{miss} performance can be obtained from the E_x^{miss} and E_y^{miss} resolutions as a function of the $\sum E_T$ in the event. The resolutions observed in the ATLAS data both at a centre-of-mass energy of 900 GeV and in a small amount of data taken at 2.36 TeV

are presented as a function of $\sum E_T$ in Figure 3.1. A very good agreement between data and Monte Carlo is obtained at both centre-of-mass energies. The E_T^{miss} resolution is $\sigma(E_x^{miss},E_y^{miss}) = 0.37 \times \sqrt{\sum E_{\mathrm{T}}}$ for both data and Monte Carlo. The error on the fitted scale factor 0.37 is negligible.

A data-simulation discrepancy has been observed in the number of events with at least one jet: they are about 4% in data and 5% in MC. In 7 TeV data described in the next section the same 20% data-simulation discrepancy in the number of events with at least one jet found in 900 GeV data is seen.

3.3.2 EM scale results in minimum bias events at $\sqrt{s} = 7$ TeV

The same distributions done for 900 GeV data have been obtained for 7 TeV minimum bias events. Results are shown in Figure 3.2. Here the E_T^{miss} distribution is found to be in good agreement with spectra comparable within 20% for data and Monte Carlo.

In data, one outlier event with E_T^{miss} of 52 GeV is due to a multi-jet event in which one of the jets points to a crack and appears to have been mis-measured. In the simulation, one outlier event at E_T^{miss} of 68 GeV, not shown in the figure, is also due to a multi-jet event where E_T^{miss} lines up with a mis-measured jet.

The resolution can be seen for ATLAS data and Monte Carlo in the right-hand plot of Figure 3.2. The resolution curve extends up to $\sum E_T$ values around 250 GeV in the present data set. For higher values of $\sum E_T$ the numbers of events in each $\sum E_T$ bin are too small to be considered for the fit. A reasonable agreement between data and Monte Carlo is obtained. The E_T^{miss} resolution is $\sigma(E_x^{miss},E_y^{miss}) = 0.41(0.43) \times \sqrt{\sum E_{\mathrm{T}}}$ for data (Monte Carlo). The error on the fitted scale factors is negligible. The observed differences in the data and Monte Carlo scale factors are likely due to imperfections of the modeling of soft particle activity in PYTHIA.

Figure 3.3 shows the distributions of E_x^{miss} and E_y^{miss} for data and Monte Carlo simulation. The discrepancy between data and simulation, more visible in E_y^{miss} distribution, is due to a small misalignment of the forward detector ($\sim$ 2.5 mm). Removing the region $|\eta| > 4.5$, mostly affected by this shift, improves the data-simulation agreement in E_T^{miss} components distribution and does not degrade E_T^{miss} resolution significantly. E_x^{miss} and E_y^{miss} for data and Monte Carlo simulation within $|\eta| < 4.5$ are shown in Figure 3.4. The agreement of the spectra is within 20%(50%) for $E_x^{miss}(E_y^{miss})$ within 15 GeV.

All the further results in this chapter are obtained only with energy deposits collected in the region $|\eta| < 4.5$ even if calibrated results have been obtained with reprocessed Monte Carlo simulated data that partially correct

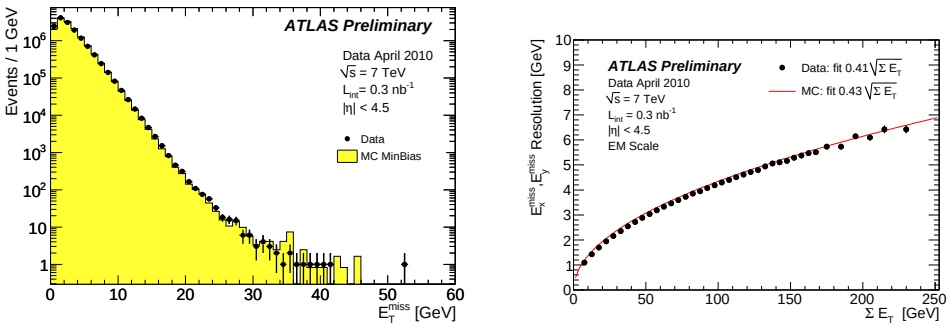

Figure 3.2: *Minimum bias events at $\sqrt{s}$= 7 TeV. (left) Distribution of E_T^{miss}. The expectation from Monte Carlo simulation is superimposed (histogram) and normalised to the number of events in data. (right) E_x^{miss} and E_y^{miss} resolution as a function of $\sum E_T$. The line represents a fit to the resolution obtained in the Monte Carlo simulation and the full dots are the results from data [52].*

for this geometry mismatch.

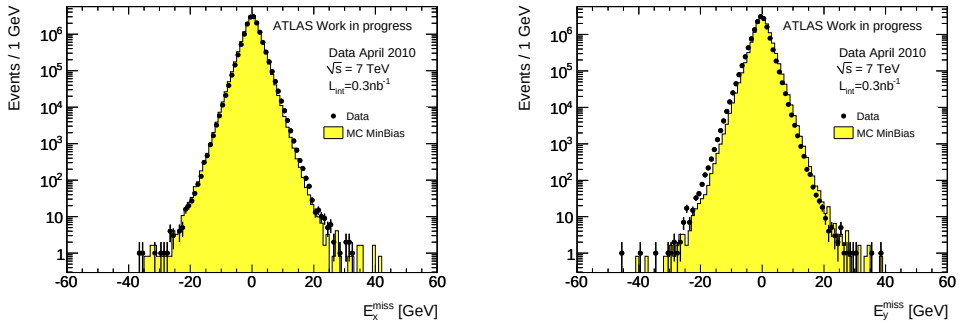

Figure 3.3: *Minimum bias events at $\sqrt{s}$= 7 TeV. E_x^{miss} (left) and E_y^{miss} distributions in the full detector acceptance ($|\eta| < 4.9$). The expectation from Monte Carlo simulation is superimposed (histogram) and normalised to the number of events in data.*

3.4 Global E_T^{miss} calibration

As briefly discussed in the Section 3.1, using the EM scale signals for all cells to reconstruct E_T^{miss} does not yield a good measure for the real missing transverse energy in events with neutrinos or possible other non-interacting

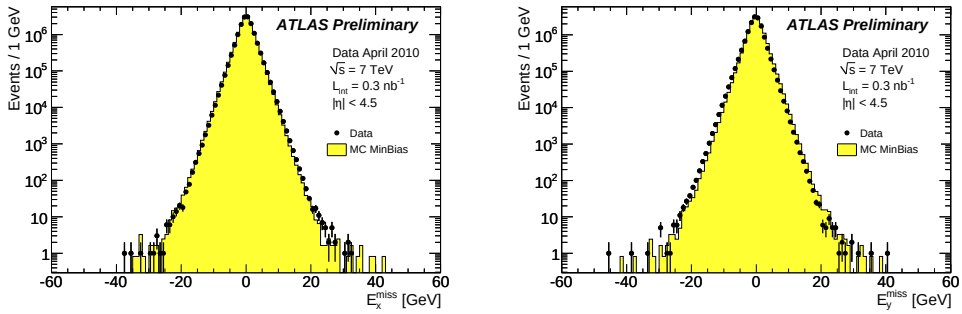

Figure 3.4: *Minimum bias events at $\sqrt{s}$= 7 TeV. E_x^{miss} (left) and E_y^{miss} distributions for the region $|\eta| < 4.5$. The expectation from Monte Carlo simulation is superimposed (histogram) and normalised to the number of events in data [52].*

particles in the final state, in particular in the presence of jets.

A dedicated calibration scheme has been developed for the hadronic energy deposits in calorimeters in which corrections for the different calorimeter response to hadrons and electrons/photons and for losses in inactive materials are applied. This gives a better reconstruction of the mean of E_T^{miss} and optimizes its resolution.

The E_T^{miss} calibrations described in this section are indicated with the term "global" since all cells belonging to topoclusters are calibrated with the same scheme, independently of the object they belong to. A calibration scheme dependent on the parent object is considered in the "refined calibration" scheme which is described in Section 3.5. The E_T^{miss} global calibration can be implemented using two different cell calibration schemes based on the cell energy density, which have been described in Section 2.4.4.

- Global cell energy-density weighting calibration scheme (Global calibration or GCW);
- Local cluster weighting calibration scheme (Local hadronic calibration or LCW).

GCW or LCW weights are applied to all calorimeter cells in topoclusters in the E_T^{miss} calculation from Equation 3.3.

3.4.1 Global calibrated E_T^{miss} performance

The distributions of E_x^{miss} and E_y^{miss} and of E_T^{miss}, shown at the EM scale in Section 3.3, are now obtained for the after applying calibrations based on calorimeter cell weighting.

The E_T^{miss} distributions for both calibrations are shown in Figure 3.5 for the same minimum bias sample. Apart for some discrepancy for very low E_T^{miss} values, they are found to be in overall good agreement within 20% with expectations from the Monte Carlo simulation. No additional tails are created by the calibration, as it can be seen comparing Figure 3.5 with the E_T^{miss} distribution at EM scale shown in Figure 3.2.

E_T^{miss} in events with jets with high transverse momentum has also been studied with significantly more data and can be seen in Figure 3.6. Above 20 GeV a data-Monte Carlo discrepancy larger than 20% in the frequency distributions is observed. Many studies have been done to understand the reason of such a disagreement and it seems to be due to events where a jet is pointing to the region $1.5 < |\eta| < 2.5$. Removing such events improves the agreement between data and simulation. The reason of this problem in this region is still under investigation.

In Figure 3.6 there are outlier events both in data and in Monte Carlo simulation. All of the events with large E_T^{miss} contain high-p_T jets, with the E_T^{miss} aligned or anti-aligned in ϕ with a high-p_T jet. This suggests jet energy mis-measurement as the source of this fake E_T^{miss} (see Section 3.1.3). Similar events are found in Monte Carlo simulation. Most of the mis-measured jets in these events enter the transition regions between the calorimeters, where the jet energy resolution is worse. These events can be rejected at the analysis level with a cut based on $\Delta\phi$(jet,E_T^{miss}).

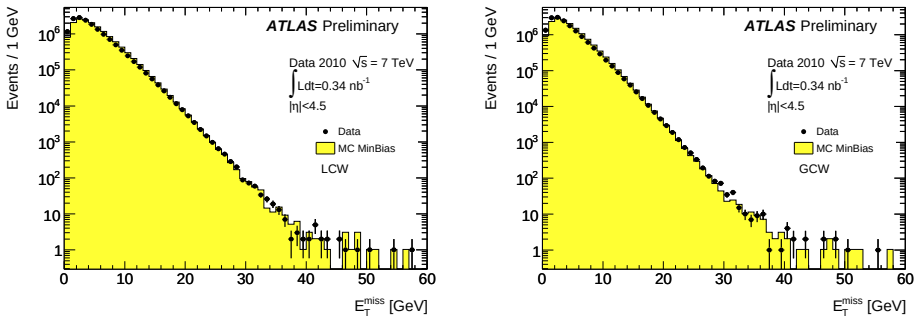

Figure 3.5: *Distribution of E_T^{miss} as measured in a data sample of* 15.2 *million selected minimum bias events (dots) at 7 TeV centre-of-mass energy, recorded in April 2010. In the calculation only topocluster cells are used, with energies calibrated with the LCW (left) and with energies calibrated with the GCW (right). The expectation from Monte Carlo simulation is superimposed (histogram) and normalised to the number of events in data [53].*

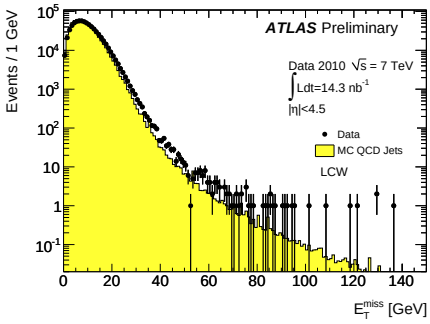

Figure 3.6: *Distribution of E_T^{miss} as measured in a data sample of about* 700 *thousand selected events with at least one jet, reconstructed with the Anti-k_t with R=0.4 algorithm, with p_T>20 GeV at EM scale at 7 TeV centre-of-mass energy, recorded in April and May 2010 (dots). In the calculation only topocluster cells are used, with energies calibrated with the LCW. The expectation from Monte Carlo simulation is superimposed (histogram) and normalised to the number of events in data [53].*

E_T^{miss} resolution curves

The E_T^{miss} resolution for data and simulation in shown in Figure 3.7. The resolution curve extends up to $\sum E_T \approx$ 300 GeV in the used data sample. A reasonable agreement between data and simulations is obtained. The observed differences in the scale factors (that are 0.49 (0.48) in data and 0.51 (0.50) in the Monte Carlo for LCW (GCW) with a negligible statistical uncertainty) are less than 5% and, as already said for EM scale resolution curves, they may be due to imperfections of the modeling of soft particle activity in PYTHIA.

The reference variable $\sum E_T$ used in Figure 3.7 is taken at the same scale to which $\sigma(E_x^{miss}, E_y^{miss})$ is reconstructed, meaning it is systematically shifted to a larger value for the same event after calibrations have been applied. This leads to the impression that the calibrated resolution is worse than the resolution at EM scale.

To permit a comparison between different calibrations, plots have been made where the calibration is taken into account event-by-event by scaling $\sigma(E_x^{miss}, E_y^{miss})$, reconstructed including the calibrations, with the ratio of $\sum E_T$ on the EM scale over $\sum E_T$ after applying the calibration and plotting it as a function of $\sum E_T$(EM).

These plots are presented in Figure 3.8, which clearly shows a resolution improvement when calibrations (GCW or LCW) are applied. These observations also indicate that even in the event sample studied here, which has

no expected net E_T^{miss}, applying the appropriate calibration improves the transverse energy balance in the event. In addition, Figure 3.8 shows that the same trend between data and Monte Carlo with respect to the E_T^{miss} resolution is preserved after application of calibrations.

The effect of calibration on the reconstruction of E_x^{miss} and E_y^{miss} can be measured by the ratio $E_{x(y)}^{\mathrm{miss,cal}}/E_{x(y)}^{\mathrm{miss,EM}}$, with cal = LCW, GCW. Figure 3.9 shows that the dependence of this ratio on $\sum E_T$ at the EM scale is very similar for data and simulations. The figure also shows that considerable differences between the two calibration approaches can be observed in both data and simulation, in particular at lower $\sum E_T$. A more quantitative comparison between data and Monte Carlo is shown in the right graph of Figure 3.9, where the double ratio $(E_{x(y)}^{\mathrm{miss,cal}}/E_{x(y)}^{\mathrm{miss,EM}})_{\mathrm{data}}/(E_{x(y)}^{\mathrm{miss,cal}}/E_{x(y)}^{\mathrm{miss,EM}})_{\mathrm{MC}}$ is plotted as function of the EM scale $\sum E_T$. At this level data and simulation agree to better than 2%, with a slightly rising systematic discrepancy with increasing $\sum E_{\mathrm{T}}$. This shows that the present Monte Carlo is adequate for the determination of the cell calibration functions used in the GCW and LCW approaches within this uncertainty.

Using the results shown in previous Figures of this section, we summarize the performance of calibrated E_T^{miss} in Figure 3.10, where the resolution of E_T^{miss} calibrated with LCW is shown for data, superimposed with the fit to the Monte Carlo simulated resolution on the LCW calibrated scale.

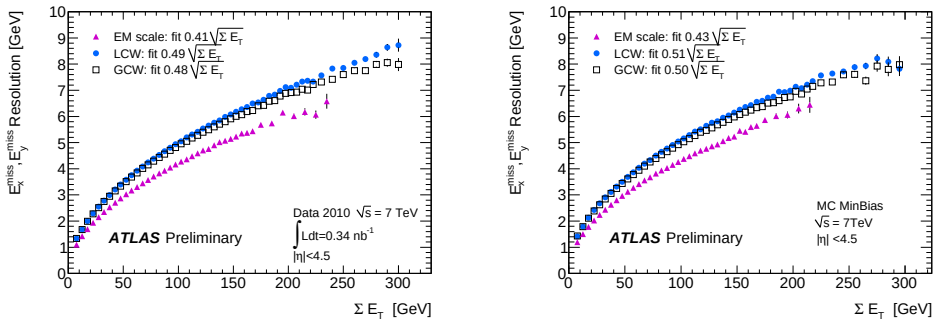

Figure 3.7: *E_x^{miss} and E_y^{miss} resolution as a function of the $\sum E_T$ for minimum bias events for data taken at $\sqrt{s}$= 7 TeV (left) and MC (right). E_x^{miss}, E_y^{miss}, $\sum E_T$ are computed with topocluster cells at the EM scale and calibrated with GCW and with LCW. The $\sum E_T$ on the x-axis is taken at the same scale to which E_x^{miss}, E_y^{miss} are reconstructed, meaning it is typically shifted to a larger value for the same event after calibrations have been applied. This leads to the impression that the calibrated resolution is worse than the resolution at EM scale [53].*

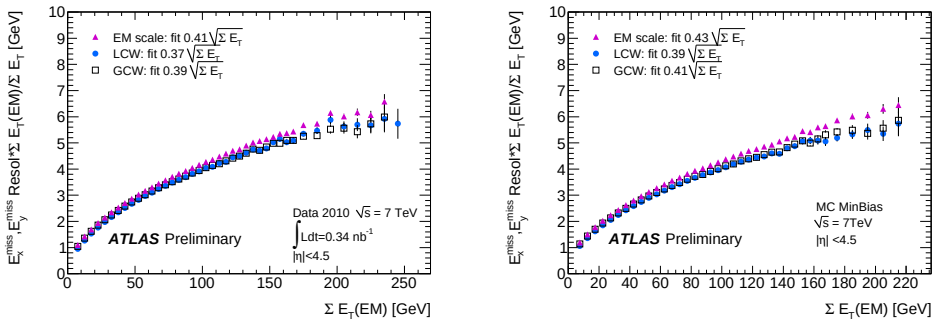

Figure 3.8: *E_x^{miss} and E_y^{miss} resolution scaled by the ratio of $\sum E_T$ at EM scale and calibrated scale as a function of $\sum E_T$ for minimum bias events for data taken at $\sqrt{s}$= 7 TeV (left) and MC (right). E_x^{miss} and E_y^{miss} are computed with topocluster cells at the EM scale and calibrated with GCW and with LCW. The $\sum E_T$ at the EM scale is used on the abscissa [53].*

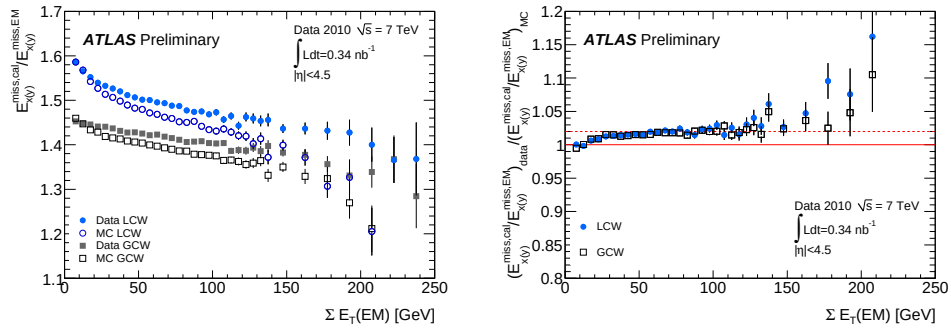

Figure 3.9: *The ratio $E_{x(y)}^{\mathrm{miss,cal}}/E_{x(y)}^{\mathrm{miss,EM}}$, with* cal $=$ LCW, GCW *and* EM $=$ *EM scale, in data and MC (left) and the double ratio $(E_{x(y)}^{\mathrm{miss,cal}}/E_{x(y)}^{\mathrm{miss,EM}})_{\mathrm{data}}/(E_{x(y)}^{\mathrm{miss,cal}}/E_{x(y)}^{\mathrm{miss,EM}})_{\mathrm{MC}}$ (right) as a function of $\sum E_T$ at the EM scale for minimum bias events for data taken at $\sqrt{s}$= 7 TeV [53].*

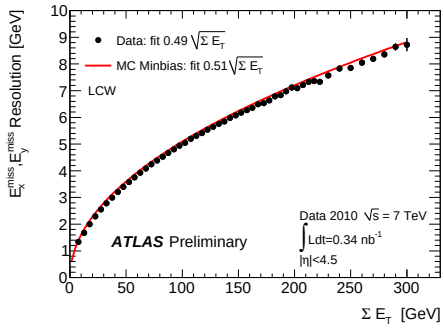

Figure 3.10: *E_x^{miss} and E_y^{miss} resolution as a function $\sum E_T$ for minimum bias events. The line represents a fit to the resolution obtained in the Monte Carlo simulation and the full dots represent the results from data taken at $\sqrt{s}$= 7 TeV. E_x^{miss}, E_y^{miss}, $\sum E_T$ are computed with topological cluster cells calibrated with LCW [53].*

E_T^{miss} dependence on topology

In events with larger hadronic activity, e.g. with jets at high transverse momentum, the E_T^{miss} resolution degrades both in data and Monte Carlo simulation. This effect is most pronounced in E_T^{miss} reconstructed at the EM scale, suggesting, as expected, that the calibration is necessary. As it can be seen in Figure 3.11 (left plot), in events with high p_T jets (p_T> 20 GeV) the resolution is worse when the E_T^{miss} is used at EM scale. When the LCW calibration is applied (right plot) the resolutions for events with different topology become more comparable. The same trend is observed both for data and Monte Carlo (Figure 3.12).

3.5 Refinement of E_T^{miss} calibration

The final step is the refinement of the calibration of cells associated with different reconstructed *physics* objects and also of cells not belonging to any object. Calorimeter cells are associated with a parent reconstructed and identified high-p_T object, in a chosen order: electrons, photons, hadronically decaying τ-leptons, jets and muons. Cells not associated to any object are also taken into account. Refined calibration of the object is then used in E_T^{miss} to replace the initial global calibration cells. The calibration of these objects is known to higher accuracy than the global calibration, enabling to improve the E_T^{miss} reconstruction. This calibration of cells on the base of the reconstructed physics object they belong to is called *refined calibration.*

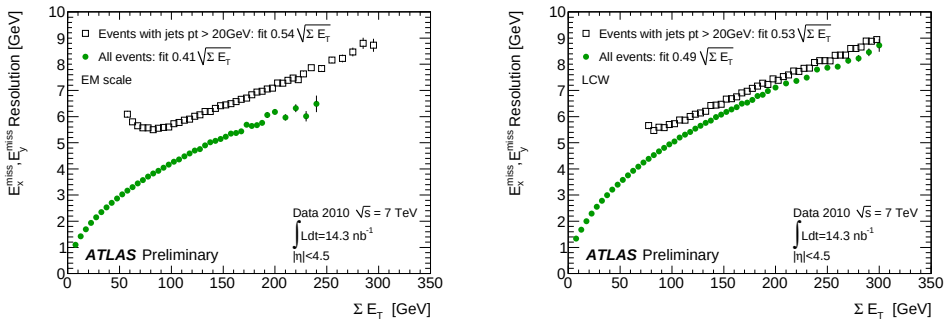

Figure 3.11: *E_x^{miss} and E_y^{miss} resolution as a function of the $\sum E_T$ for minimum bias and L1Calo events for data taken at $\sqrt{s}$= 7 TeV. E_x^{miss}, E_y^{miss} and $\sum E_T$ are computed with topocluster cells at the EM scale (left) and calibrated with LCW (right) [53].*

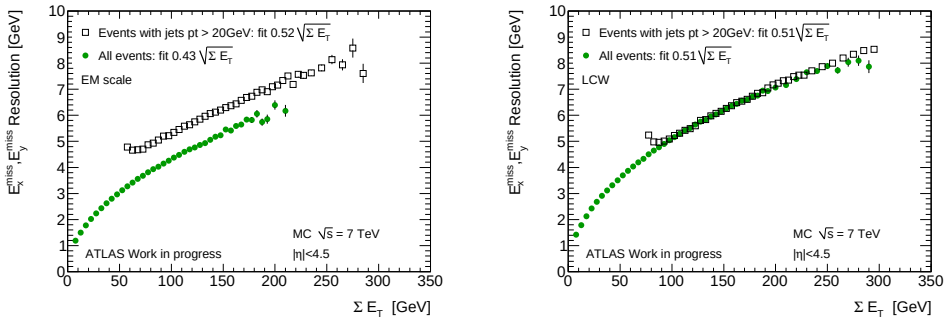

Figure 3.12: *E_x^{miss} and E_y^{miss} resolution as a function of the $\sum E_T$ for MC minimum bias and QCD at $\sqrt{s}$= 7 TeV. E_x^{miss}, E_y^{miss} and $\sum E_T$ are computed with topocluster cells at the EM scale (left) and calibrated with LCW (right) [53].*

Once the cells are associated with categories of objects as described above and calibrated, E_T^{miss} is calculated as follows:

$$E_{x(y)}^{\text{miss,calo,calib}} = E_{x(y)}^{\text{miss},e} + E_{x(y)}^{\text{miss},\gamma} + E_{x(y)}^{\text{miss},\tau} + E_{x(y)}^{\text{miss,jets}} + E_{x(y)}^{\text{miss,calo},\mu} + E_{x(y)}^{\text{miss,CellOut}} \quad (3.7)$$

where each term is calculated from the negative sum of calibrated cell energies inside the corresponding objects.

In Section 3.5.1 the different contributions are described in detail. The final $E_{x(y)}^{\text{miss,calib}}$ is then calculated from Equation 3.2 adding to $E_{x(y)}^{\text{miss,calo,calib}}$ term the $E_{x(y)}^{\text{miss},\mu}$ and $E_{x(y)}^{\text{miss,cryo}}$ terms, which are discussed in more detail in Section 3.1 and in Section 3.5.2 (see also Figure 3.13 that presents a schematic view of the algorithm).

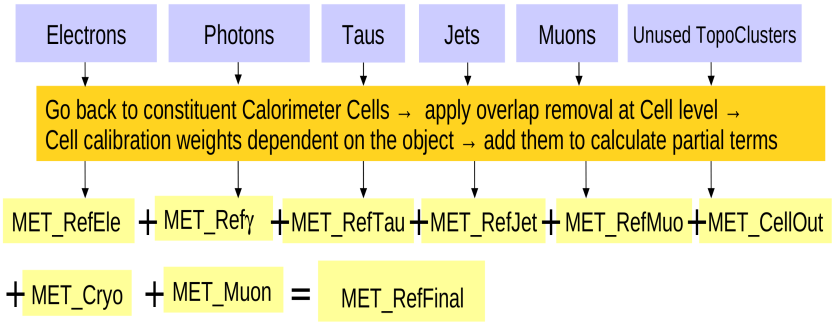

Figure 3.13: *Sketch to illustrate how the reconstructed physics objects are used to calculate* E_T^{miss}.

3.5.1 The E_T^{miss} calo term

The contribution coming from the different calorimeter energy deposits is described in Equation 3.7.

The calorimeter cells are associated with the reconstructed objects through the use of an association map. This map is filled starting from the reconstructed/identified objects in the chosen order, navigating back to their component clusters and back again to their cells. If a cell belongs to several kinds of reconstructed objects, only the first association is included in the map, i.e. the overlap removal is done at cell level. This avoids double counting of cells in the E_T^{miss} calculation. In the following the different contributions are described.

Electron contribution: $E_{x,y}^{\mathrm{miss},e}$

For electrons, the final cluster-level calibration (which can be propagated back to the cell-level) described in Section 2.4.2 is used. This calibration corrects for upstream material, longitudinal leakage and out-of-cone energy. The last correction is not applied in the E_T^{miss} calculation because the contribution of cells outside objects already accounts for it.

Photon contribution: $E_{x,y}^{\mathrm{miss},\gamma}$

Photons are used at the EM scale because of their low purity and the proper photon calibration is not applied.

Tau-jet contribution: $E_{x(y)}^{\mathrm{miss},\tau}$

At the moment the τ contribution is calibrated with the Global Calibration scheme chosen for the jet term (LCW or GCW). The correct way to treat cells belonging to τ objectsτ would be to apply to them also a τ-jet energy scale calibration. The implementation of the tau-jet Energy Scale correction in E_T^{miss} calculation is still to be done at the moment of the writing of this thesis.

Jet contribution: $E_{x(y)}^{\mathrm{miss,jets}}$

The jet contribution has been split in two classes:

- soft jets with 7 GeV $< p_T <$ 20 GeV,
- jets with p_T above 20 GeV.

This separation allows to have different calibrations for low energy jets with respect to high energetic ones due to the fact that the Jet Energy Scale (JES, see Section 2.4.4) calibration is only available for jets with $p_T >$ 20 GeV (for details see Section 2.4.4 and Ref.[54]).

Two contributions give the overall JES factor: the *response* accounting for the effect of dead material and of the calorimeter non-compensation and the *showering* accounting for truth particles depositing their energy out-of-cone, in-cone energy falling outside the reconstructed jet and out-of-cone energy falling outside the jet. Since the effect of the *showering* is already taken into account in the contribution of topoclusters outside reconstructed objects, the JES could give a double counting contribution, therefore the performance has been evaluated with and without this calibration to estimate the effect of the possible over-correction.

Different combinations of calibrations have been studied for the jet term: EM, LCW, GCW with and without JES.

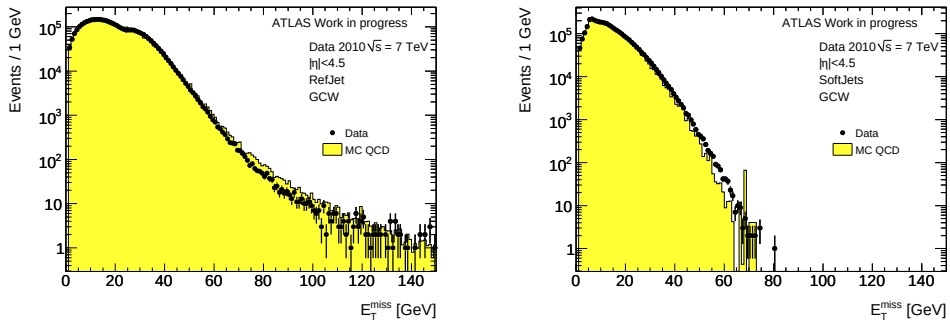

Figure 3.14: *E_T^{miss} distribution for jets with $p_T > 20$ GeV (left) and soft jets (right) terms calibrated with GCW for data (dots) and Monte Carlo simulation (histograms) at 7 TeV centre-of-mass energy. The number of events in Monte Carlo simulation are normalised to the number of events in data.*

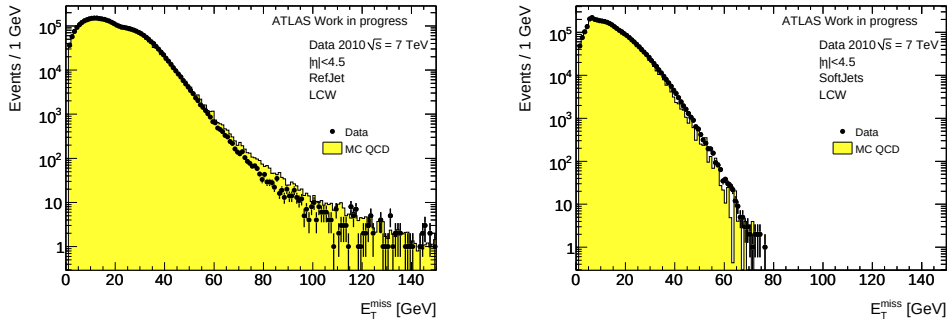

Figure 3.15: *E_T^{miss} distribution for jets with $p_T > 20$ GeV (left) and soft jets (right) terms calibrated with LCW for data (dots) and Monte Carlo simulation (histograms) at 7 TeV centre-of-mass energy. The number of events in Monte Carlo simulation are normalised to the number of events in data.*

Figure 3.14 shows the distribution for both high p_T jet and soft jet terms for 7 TeV data. A good agreement in the spectra within the 20% between data and simulation is found for the soft jet term both for the Local and for the Global calibrated data. For the high p_T jets distributions a disagreement in events with jet p_T above 60 GeV is found. As already said in Section 3.4.1 these are mainly events where a jet is pointing to $1.5 < |\eta| < 2.5$.

Figures 3.14 and 3.15 show a double bump structure in the high p_T jets distributions. The low E_T^{miss} value bump is due to two-jets events that are more balanced in transverse energy, as it is visible in Figure 3.16 that shows E_T^{miss} for the high-p_T jets term in case of two jets events, the second bump is likely from single jets events.

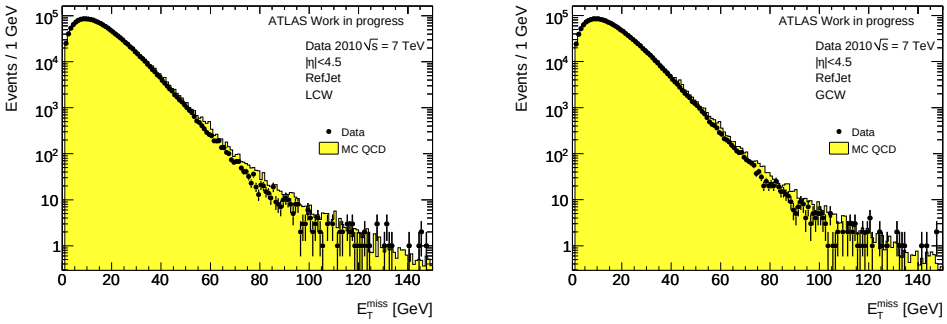

Figure 3.16: *E_T^{miss} distribution for GCW (left) and LCW (right) jets terms in events with two jets with $p_T > 20$ GeV for data (dots) and Monte Carlo simulation (histograms) at 7 TeV centre-of-mass energy. The number of events in Monte Carlo simulation are normalised to the number of events in data.*

Muons contribution in calorimeters: $E_{x(y)}^{\mathrm{miss,calo},\mu}$

The $E_{x(y)}^{\mathrm{miss,calo},\mu}$ is the contribution to E_T^{miss} from the energy lost by muons in the calorimeter. It contributes to the final E_T^{miss} according to the muon type used for the calculation of the E_T^{miss} muon term (see Section 3.1).

Cells outside physics objects: $E_{x(y)}^{\mathrm{miss,CellOut}}$

The $E_{x(y)}^{\mathrm{miss,CellOut}}$ term is calculated from the cells in topoclusters which are not included in any reconstructed object.

The importance of the energy deposits of these low energy particles for the E_T^{miss} calculation is evident in Figure 3.17 that shows the distribution

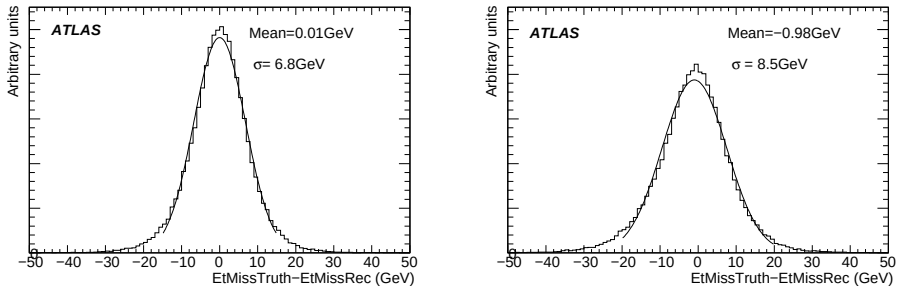

Figure 3.17: *Distribution of the difference between true and reconstructed E_T^{miss} for $Z \rightarrow \tau\tau$ simulated events (left) including and (right) excluding cells in topoclusters not associated with reconstructed high-p_T objects.*

of the difference between true and reconstructed E_T^{miss} for $Z \rightarrow \tau\tau$ simulated events including and excluding cells in topoclusters not associated with reconstructed high-p_T objects. The shift in the absolute value of the reconstructed E_T^{miss} is about 1 GeV while the resolution is degraded by a factor ~ 1.25.

For the present study we have taken into account three different calibration for the CellOut term: LCW, GCW and LCW and the so-called *Energy Flow calibration* (Eflow).

The Energy Flow is a calibration dedicated to low energy deposits that may not seed a topocluster and moreover it exploits the tracking power of the ATLAS inner detector that provides better resolution and calibration at low p_T.

In fact this algorithm adds tracks to E_T^{miss} calculation and substitutes them to associated topoclusters with the procedure briefly described in the following:

- select tracks with quality criteria;
- remove from tracks the muons found in the muon containers;
- veto tracks associated to topoclusters in identified objects using conservative cuts to avoid inefficient associations;
- add tracks not associated to topoclusters in E_T^{miss} calculation;
- add all remained topoclusters to E_T^{miss} calculation.

The Energy Flow algorithm uses LCW calibrated topoclusters, therefore it cannot be applied in case of GCW calibration. More details on the Energy Flow algorithm can be found in [55].

The effect of applying the Energy Flow calibration to the cells outside physics objects is visible for simulated $Z \rightarrow \mu\mu$ events in Figure 3.18. It shows the mean value of the projection of E_T^{miss} along the Z boson axis as a function of the Z p_T.

$Z \rightarrow \mu\mu$ events have no genuine E_T^{miss} and thus E_T^{miss} along the Z axis is expected to be 0, because the Z is completely balanced by the hadronic recoil, which mainly consists in low energy deposits since jets occur only in $\sim 20\%$ of Z events. When using the the refined calibration for reconstructed E_T^{miss} there is a negative bias that increases for high Z p_T due to the inefficient calibration of low energy deposits. The bias is largely reduced when applying Energy Flow calibration.

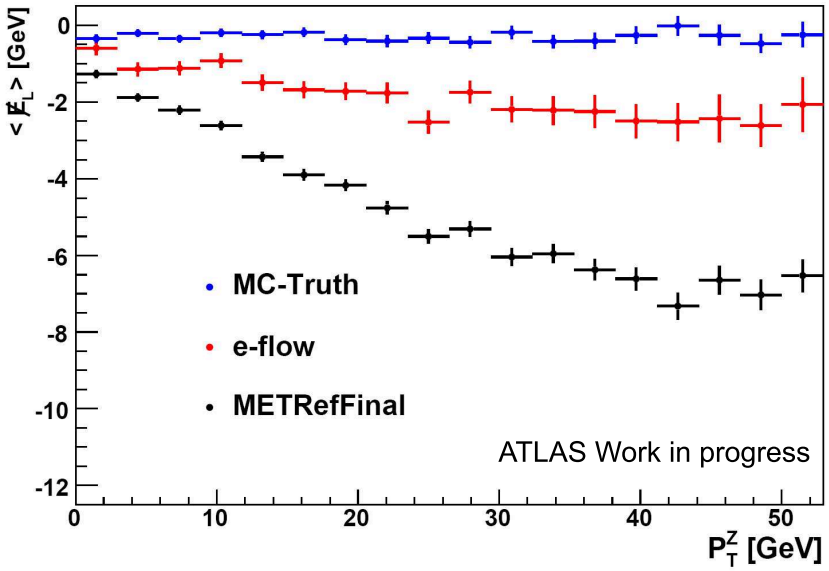

Figure 3.18: *E_L^{miss} mean as a function of the the Z p_T, using the the refined calibration for reconstructed events (black), the refined calibration plus Energy Flow for the CellOut term (red) and using Monte Carlo-truth information (blue line) for Monte Carlo $Z \rightarrow \mu\mu$ events [55].*

3.5.2 The E_T^{miss} cryostat term

The correction for the energy lost in the cryostat between the LAr barrel electromagnetic calorimeter and the TileCal barrel hadronic calorimeter, which at a thickness of about half an interaction length can lead to significant energy losses in hadronic showers, is separately applied in case of

the calorimeter calibration with GCW. When the calorimeter term is calibrated with the LCW scheme, a corresponding correction is already done at topocluster level, e.g. $E_{x(y)}^{\text{miss,cryo}} = 0$.

The E_T^{miss} reconstruction, when it is calibrated with GCW, recovers this loss of energy in the cryostat using the correlation of energies between the last layer of the LAr calorimeter and the first layer of the hadronic calorimeter. This correction is called the "cryostat term" when used for jet energy correction. It is defined as follows:

$$E_{x(y)}^{\text{miss,cryo}} = -\sum_{\text{jets}} E_{x(y)}^{\text{jet,cryo}} \tag{3.8}$$

where all reconstructed jets are summed in the event, and

$$\begin{aligned} E_x^{\text{jet,cryo}} &= w^{\text{cryo}} \sqrt{E_{\text{EM3}}^{\text{jet}} \times E_{\text{HAD1}}^{\text{jet}}} \frac{\cos\phi_{\text{jet}}}{\cosh\eta_{\text{jet}}} \\ E_y^{\text{jet,cryo}} &= w^{\text{cryo}} \sqrt{E_{\text{EM3}}^{\text{jet}} \times E_{\text{HAD1}}^{\text{jet}}} \frac{\sin\phi_{\text{jet}}}{\cosh\eta_{\text{jet}}} \end{aligned} \tag{3.9}$$

where w^{cryo} is a calibration factor, determined together with the cell signal calibration weights in the GCW fits. E_{EM3} and E_{HAD} are the energies in jets deposited on the third layer of the electromagnetic calorimeter and in the first layer of the hadronic calorimeter, respectively. The cryostat correction turns out to only be non-negligible for high-p_T jets, so it is not crucial in minimum bias events.

3.6 Refined calibration results in 7 TeV data

Configurations	e/γ	τ	Jets	soft jets	CellOut	Muon
1 GCW	default	GCW	GCW	GCW	GCW	`STACO`
2 GCW_NI	default	GCW	GCW+NI	GCW	GCW	`MuId`
3 LCW	default	LCW	LCW	LCW	LCW	`STACO`
4 LCW_NI_eflow	default	LCW	LCW+NI	LCW	LCW+eflow	`STACO`
5 LCW_NI_ noSoftJet_eflow	default	LCW	LCW+NI	-	LCW+eflow	`STACO`
6 EMJES	default	LCW	EM+NI	LCW	LCW	`STACO`
7 LCW_NI	default	LCW	LCW+NI	LCW	LCW	`STACO`
8 LCW_eflow	default	LCW	LCW	LCW	LCW+eflow	`STACO`

Table 3.1: *Refined calibrations configurations.*

In this section the results obtained using different configurations for the most refined E_T^{miss} calibration will be shown, exploiting the different calibration possibilities for the different objects as described in the previous section. For this study L1Calo data (defined in Section 3.2) have been used. For simulated data Monte Carlo di-jet events are considered.

A scheme of the 8 different configurations that have been studied is shown in Table 3.1, where NI means that the JES is applied in the form of the numerical inversion correction (see Section 2.4.4 for details).

3.6.1 Resolution for GCW calibration configurations

As discussed in Section 3.1.1 the E_T^{miss} performance can be evaluated studying the E_x^{miss}, E_y^{miss} resolutions as function of the total transverse energy $\sum E_T$. We have first studied the two calibration schemes using GCW (number 1 and 2 in Table 3.1):

- **GCW configuration**: electrons are calibrated with their proper calibration, photons are taken at the EM scale, `STACO` is used for muons, all other objects and CellOut are calibrated according to the GCW calibration.

- **GCW_NI configuration**: electrons are calibrated with their proper calibration, photons are taken at the EM scale, `MuId` is used for muons, high p_T jets are calibrated with GCW plus the JES, all other objects and CellOut are calibrated according to the GCW calibration.

Figure 3.19 shows the distributions as in Figure 3.8 for data at the EM scale with no calibration (*Topo*), applying the GCW scheme (*GCW*) and applying GCW_NI (*GCW_NI_Muid*) in events with at least one jet with $p_T > 20$ 20 GeV (left) and in events with only two jets both with $p_T > 20$ GeV (right).

Figure 3.20 shows the same distributions for Monte Carlo di-jet events.

The E_T^{miss} resolution is $\sigma(E_x^{miss},E_y^{miss}) = a \times \sqrt{\sum E_{\mathrm{T}}}$ where the fitted scale factor a assumes values $a = 0.54$ (0.54) in EM scale case, $a = 0.45$ (0.42) in GCW case and $a = 0.45$ (0.41) in GCW_NI case for data (MC) when considering events with at least one jet with $p_T > 20$ GeV. For 2 jets events the fitted scale factor values are $a = 0.49$ (0.52) in EM scale case, $a = 0.41$ (0.41) both in GCW and GCW_NI cases for data (MC). The error on a is negligible.

Both data and Monte Carlo distributions show better resolutions for events with two jets because such events have better transverse energy balance. Moreover when using GCW_NI the two highest p_T objects in the event (the two jets) are calibrated with the same calibration, while in a generic

event with at least one jet with $p_T > 20$ GeV there can be a large contribution from topoclusters outside objects and soft jets that are calibrated differently. The small discrepancy between data and simulation up to 5%, already present in the minimum bias event distributions in Figures 3.2 and 3.5, is still visible here.

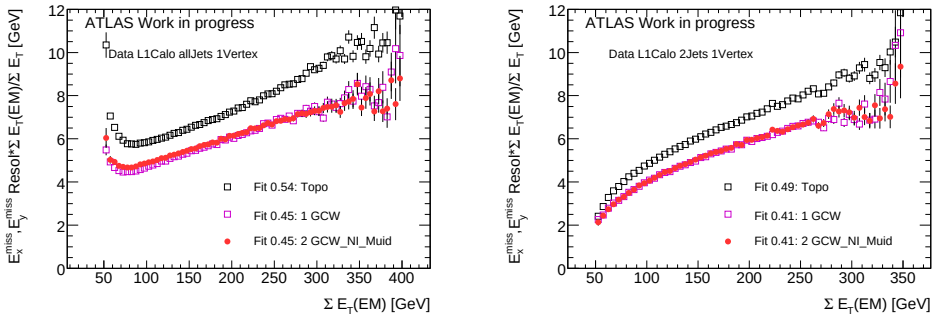

Figure 3.19: *E_x^{miss} and E_y^{miss} resolution scaled by the ratio of $\sum E_T$ at EM scale and calibrated scale as a function of the $\sum E_T$ for data taken at $\sqrt{s}$= 7 TeV for events with at least 1 jet with $p_T > 20$ GeV (left) and for events with 2 jets with $p_T > 20$ GeV (right). E_x^{miss}, E_y^{miss}, $\sum E_T$ are computed with topocluster cells at the EM scale (Topo) and calibrated with GCW (GCW) and with GCW_NI (GCW_NI_Muid). The $\sum E_T$ on the x-axis is taken at the EM scale.*

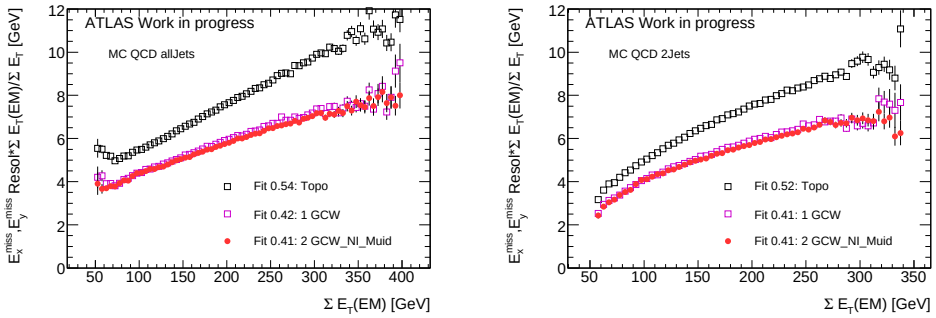

Figure 3.20: *E_x^{miss} and E_y^{miss} resolution scaled by the ratio of $\sum E_T$ at EM scale and calibrated scale as a function of the $\sum E_T$ for 7 TeV Monte Carlo simulated di-jet events for events with at least 1 jet with $p_T > 20$ GeV (left) and for events with 2 jets with $p_T > 20$ GeV (right). E_x^{miss}, E_y^{miss}, $\sum E_T$ are computed with topocluster cells at the EM scale (Topo) and calibrated with GCW (GCW) and with GCW_NI (GCW_NI_Muid). The $\sum E_T$ on the x-axis is taken at the EM scale.*

Figures 3.19 and 3.20 show a significant improvement in E_T^{miss} resolution when applying the calibration, as already observed in Figure 3.11 of Section 3.4.1. The JES correction does not have a big effect on the resolution. In fact both in data and in simulation results for all jets and two jets, GCW and GCW_NI calibrations configurations reach the same performance.

3.6.2 Resolution for LCW calibration configurations

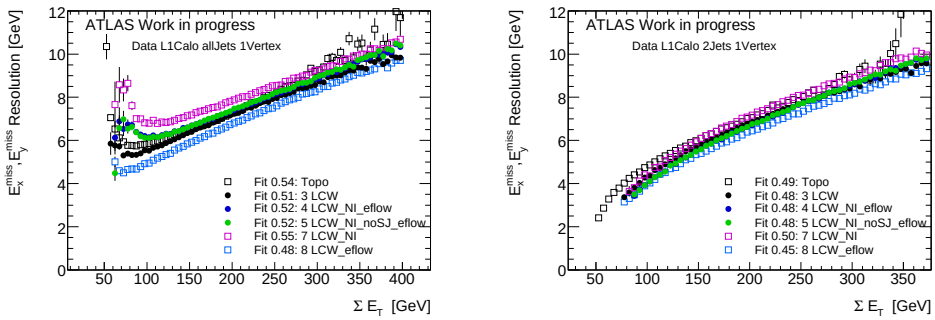

Figure 3.21: *E_x^{miss} and E_y^{miss} resolution as a function of the $\sum E_T$ for data taken at $\sqrt{s}$= 7 TeV for events with at least 1 jet with $p_T > 20$ GeV (left) and for events with 2 jets with $p_T > 20$ GeV (right). E_x^{miss}, E_y^{miss}, $\sum E_T$ are computed with topocluster cells at the EM scale (Topo) and calibrated with 5 different LCW calibration schemes. The $\sum E_T$ on the x-axis is taken at the same scale to which E_x^{miss}, E_y^{miss} are reconstructed.*

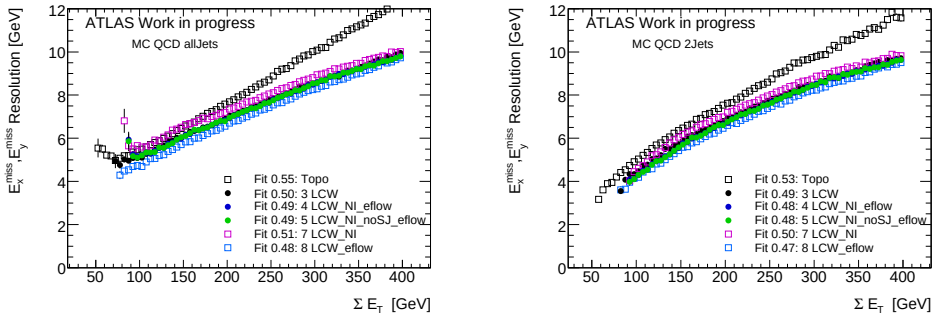

Figure 3.22: *E_x^{miss} and E_y^{miss} resolution as a function of the $\sum E_T$ for MC di-jet events with at least 1 jet with $p_T > 20$ GeV (left) and with 2 jets with $p_T > 20$ GeV (right). E_x^{miss}, E_y^{miss}, $\sum E_T$ are computed with topocluster cells at the EM scale (Topo) and calibrated with 5 different LCW calibration schemes. The $\sum E_T$ on the x-axis is taken at the same scale to which E_x^{miss}, E_y^{miss} are reconstructed.*

In the case of LCW calibration, five different configurations have been studied (numbers from 3 to 5 and 7 to 8 in Table 3.1):

Electrons are calibrate with their proper calibration, photons are taken at the EM scale and τ are calibrated with LCW and `STACO` muons are used, while jets, soft jets and topoclusters outside objects can be calibrated in different ways:

- **LCW configuration**: high p_T jets, soft jets and CellOut are calibrated according to the LCW calibration.
- **LCW_NI_eflow configuration**: high p_T jets are calibrated with LCW plus the JES, soft jets with LCW, CellOut term is calibrated with LCW plus Energy Flow.
- **LCW_NI_noSoftJets_eflow configuration**: high p_T jets are calibrated with LCW plus the JES, soft jets and CellOut terms are calibrated with LCW plus Energy Flow.
- **LCW_NI configuration**: high p_T jets are calibrated with LCW plus JES, soft jets and CellOut term is calibrated according to the LCW calibration.
- **LCW_eflow configuration**: jest are calibrated with LCW, CellOut term is calibrated with LCW plus Energy Flow.

Figures 3.21 and 3.22 show E_T^{miss} resolution curves for all jet events and 2 high p_T jets events for data and Monte Carlo respectively for the 5 different calibration schemes and for the EM scale (*Topo*) where the reference variable $\sum E_T$ is taken at the same scale to which $\sigma(E_x^{miss}, E_y^{miss})$ is reconstructed. Figures 3.23 and 3.24 compare different calibrations.

The E_T^{miss} resolution is $\sigma(E_x^{miss},E_y^{miss})= a \times \sqrt{\sum E_{\mathrm{T}}}$ where the fitted scale factor a assumes values $a = 0.42$ (0.41) in LCW case $a = 0.40$ (0.39), in LCW_NI_eflow and in LCW_NI_noSoftJets_eflow cases, $a = 0.43$ (0.41), in LCW_NI case and $a = 0.38$ (0.39) in LCW_eflow case for data (MC) when considering events with at least one jet with $p_T > 20$ GeV. For 2 jets events the fitted scale factor values are $a = 0.39$ (0.40) in LCW case $a = 0.37$ (0.38) in LCW_NI_eflow and LCW_NI_noSoftJets_eflow cases, $a = 0.40$ (0.40), in LCW_NI case and $a = 0.36$ (0.38) in LCW_eflow case The error on a is negligible.

Applying the JES makes the E_T^{miss} resolution slightly worse and this may indicate a small problem with double counting due to the use of JES.

Applying Energy Flow calibration to the cells outside physics objects yields a significant improvement in E_T^{miss} resolution, of about 5%. As for the GCW case, better results are found in the case of two jets events, with

an improvement of about 4%(2%) in the scale factor for data (simulation) distributions. The trend in data is well reproduced by the Monte Carlo simulation even if a 5% disagreement is still present.

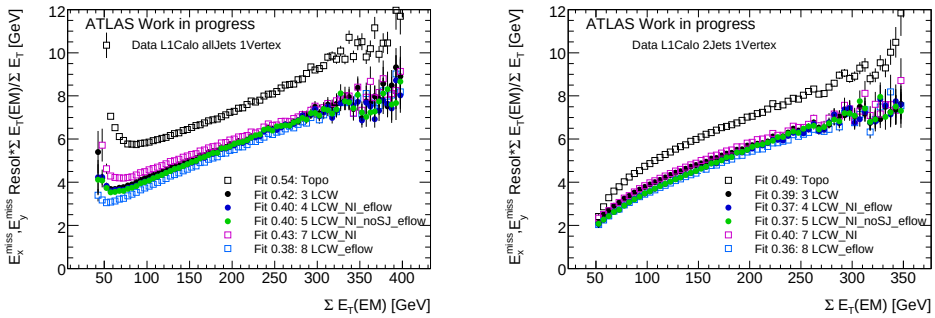

Figure 3.23: E_x^{miss} *and* E_y^{miss} *resolution scaled by the ratio of* $\sum E_T$ *at EM scale and calibrated scale as a function of the* $\sum E_T$ *for data taken at* $\sqrt{s}$= 7 *TeV for events with at least 1 jet with* $p_T > 20$ *GeV (left) and for events with 2 jets with* $p_T > 20$ *GeV (right).* E_x^{miss}, E_y^{miss}, $\sum E_T$ *are computed with topocluster cells at the EM scale (Topo) and with 5 different LCW calibration schemes. The* $\sum E_T$ *on the x-axis is taken at the EM scale.*

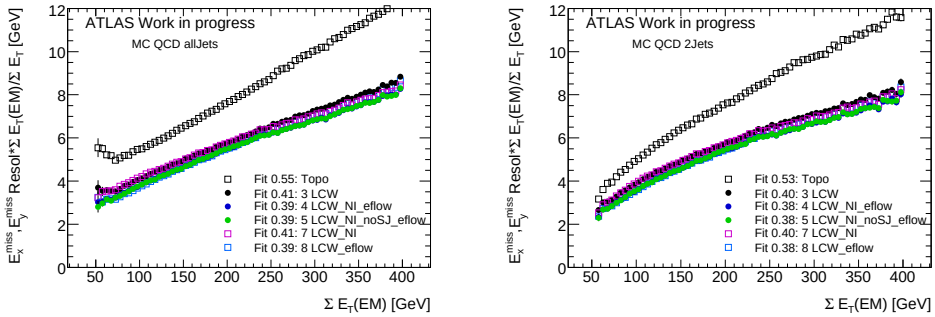

Figure 3.24: E_x^{miss} *and* E_y^{miss} *resolution scaled by the ratio of* $\sum E_T$ *at EM scale and calibrated scale as a function of the* $\sum E_T$ *for 7 TeV Monte Carlo simulated di-jet events for events with at least 1 jet with* $p_T > 20$ *GeV (left) and for events with 2 jets with* $p_T > 20$ *GeV (right).* E_x^{miss}, E_y^{miss}, $\sum E_T$ *are computed with topocluster cells at the EM scale (Topo) and calibrated with 5 different LCW calibration schemes. The* $\sum E_T$ *on the x-axis is taken at the EM scale.*

3.6.3 Linearity results

To evaluate the linearity, as described in Section 3.1.2, events with genuine E_T^{miss} are needed and $E_{\mathrm{T}}^{miss,\mathrm{True}}$ has to be known, thus linearity studies are

possible only using Monte Carlo simulation.

Figure 3.25 shows the linearity in simulated $t\bar{t}$ events for the different calibration configurations that have been described in Sections 3.6.1 and 3.6.2 and for

- **EMJES configuration**: electrons are calibrated with their proper calibration, photons are at the EM scale, `STACO` is used for muons, high p_T jets are calibrated only with the JES (EMJES), all other objects and cells outside physics objects are calibrated according to the LCW calibration.

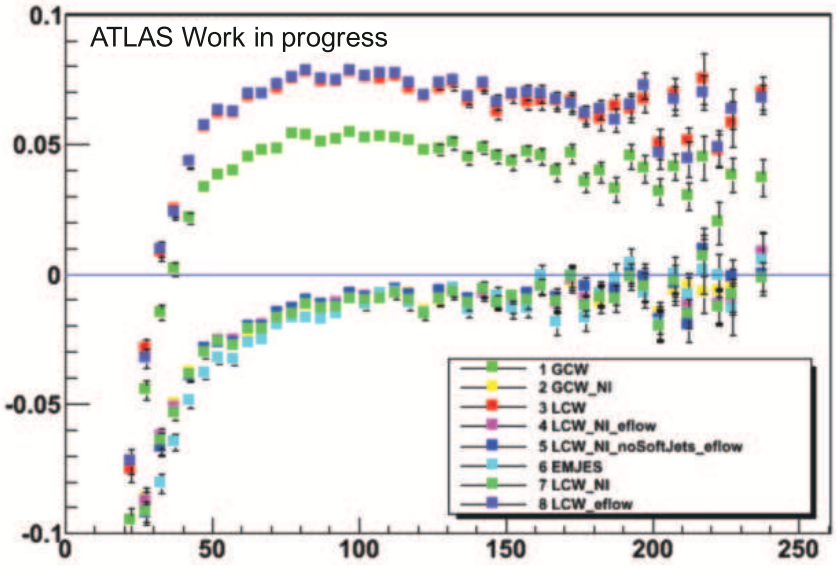

Figure 3.25: *E_T^{miss} linearity in Monte Carlo $t\bar{t}$ events. Results for all the different calibration configurations are compared.*

The bias of linearity at low $E_{\mathrm{T}}^{miss,\mathrm{True}}$ is due to the finite resolution of the E_T^{miss} measurement. The reconstructed E_T^{miss} is positive by definition, so the linearity is negative when the true E_T^{miss} is near to zero.

It is evident that applying the JES (NI) determines a significant improvement in the linearity both at EM scale and for GCW and LCW calibration schemes while Energy Flow calibration does not contribute to restore the linearity.

3.6.4 Toward the best calibration

A good performance in terms of resolution and linearity may enhance the ability to reconstruct the mass of final states which involve neutrinos.

In the previous sections many different calibration schemes have been studied and their performance has been compared. Since from Figure 3.25 the JES has been found to be important to obtain a good E_T^{miss} linearity, despite the possible double counting problem, only calibration schemes where JES is applied to the jet contribution are considered.

To summarize the results obtained so far a selection of resolution curves is presented in Figure 3.26 showing all events with jets on the left, and events with 2 high p_T jets on the right. It shows for LCW and GCW based calibrations the configuration giving the best performance from Figures 3.19 and 3.23: GCW_NI and LCW_NI_eflow.

To fully understand the different effects LCW_NI is also shown (with no Energy Flow calibration added to cells outside physics objects). The EMJES case is also shown to understand the effect of applying only the Jet Energy Scale but no calibration on jets.

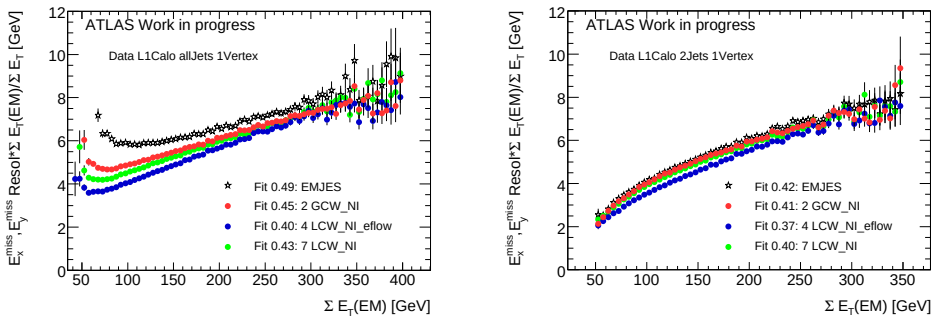

Figure 3.26: *E_x^{miss} and E_y^{miss} resolution scaled by the ratio of $\sum E_T$ at EM scale and calibrated scale as a function of the $\sum E_T$ for data taken at $\sqrt{s}$= 7 TeV for events with at least 1 jet with $p_T > 20$ GeV (left) and for events with 2 jets with $p_T > 20$ GeV (right). E_x^{miss}, E_y^{miss}, $\sum E_T$ are computed with topocluster cells with different calibration schemes. The $\sum E_T$ on the x-axis is taken at the EM scale.*

From Figure 3.26 the following conclusions can be drawn:

- The best resolution is obtained using the LCW_NI_eflow configuration, that provides a scale factor of 0.37 in case of two jets events and of 0.40 in case of generic jets events as a function of $\sum E_T$ at EM scale;
- LCW performs slightly better than GCW improving the E_T^{miss} resolution performance of about 2% (4%) for two jets (all jets) events;

- The Energy Flow calibration has a large impact on the resolution, in fact the LCW_NI case shows a 8% (7%) degradation in the scale factor for two jets (all jets) events;
- The configuration with EMJES applied to jet at EM scale gives worse resolution with respect to GCW_NI and LCW_NI of 2-5% (10%) for two jets (all jets) events.

Therefore the conclusion of this detailed study on E_T^{miss} is that the best calibration is obtained with:

- electrons calibrated with their proper calibration,
- photons at EM scale,
- `STACO` muons,
- τ-jets calibrated with LCW,
- jets ($p_T > 20$ GeV) calibrated with LCW + JES,
- soft jets ($8 < p_T(\text{GeV}) < 20$) calibrated with LCW,
- topoclusters outside reconstructed object calibrated with LCW + Energy Flow.

A further improvement in the calibration can be obtained removing the out-of-cluster correction in the JES in order to avoid the double counting. This can be obtained either factorising the terms of JES correction (see Section 3.5.1) in order to not apply the *showering* term in the E_T^{miss} calibration or selecting two coaxial cones, the first one containing the jet topoclusters, the second one containing also the out-of-cluster contributions, and subtracting the ring region (conical corona) between them from the CellOut term.

E_T^{miss} and its components distributions for 7 TeV data and simulation are shown in Figure 3.27. The agreement is found good for E_T^{miss} up to 20 GeV. For larger values of E_T^{miss} the spectra deviate up to 40%.

3.7 $\sum E_T$ distributions

The $\sum E_T$ quantity is used to obtain the resolution curves, thus a detail study on the performance of $\sum E_T$ measurement has been performed and results are presented in this section.

The top left plot of Figure 3.28 shows the $\sum E_T$ distributions for 7 TeV events with at least one jet of $p_T > 20$ GeV calibrated using the best available calibration described above. For $\sum E_T$ values above 200 GeV the

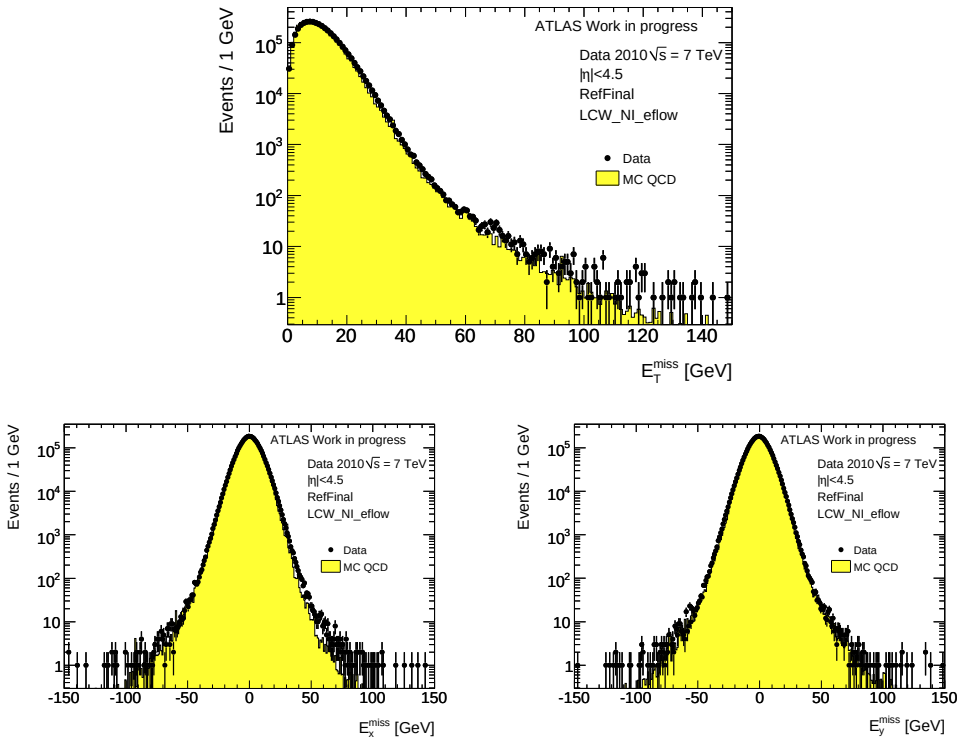

Figure 3.27: *E_T^{miss} (top), E_x^{miss} (bottom left) and E_y^{miss} (bottom right) distributions for the best calibration configuration. The number of events in Monte Carlo simulation are normalised to the number of events in data.*

data spectra are harder than simulation up to 60%. To understand its origin the $\sum E_T$ distributions for the most significant contributions are also shown in Figure 3.28 for L1Calo events.

The largest data-simulation disagreement in the distributions is observed for soft jets and cells outside objects, where data spectra are systematically much harder than simulation, suggesting a problem of modeling of soft physics in the Monte Carlo.

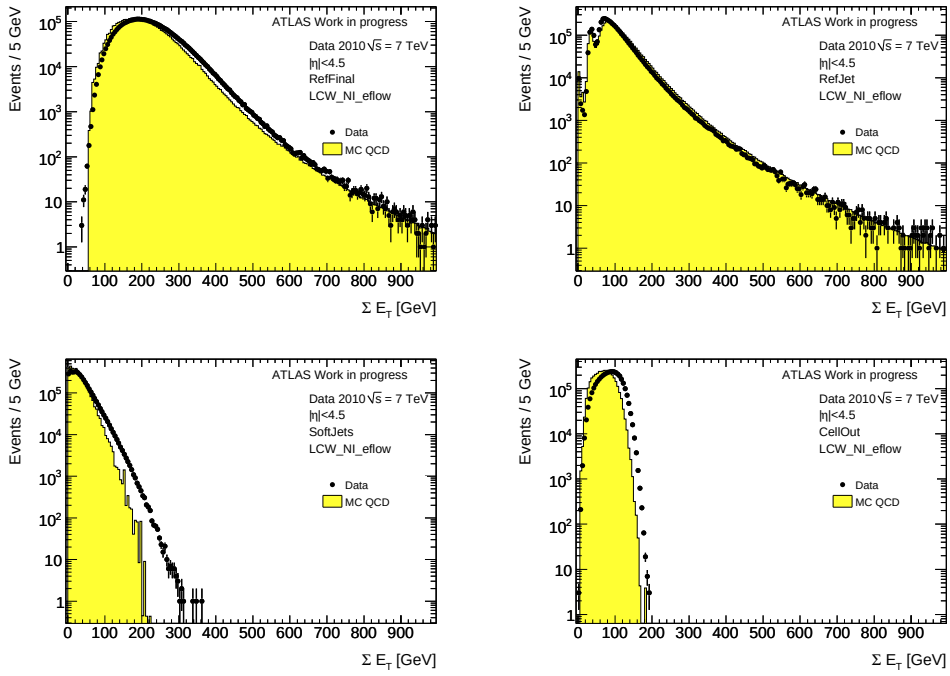

Figure 3.28: *(top left) $\sum E_T$ distribution for $\sqrt{s}$= 7 TeV events with at least one jet of $p_T > 20$ GeV. LCW_NI_eflow calibration is applied. $\sum E_T$ for jets (top right), soft jets (bottom left) and CellOut (bottom right) terms are also shown. The expectation from MC simulation is superimposed (histogram) and normalised to the number of events in data.*

Since L1Calo events used in Figure 3.28 are mainly high p_T jets events, the same distributions have been studied with minimum bias events at 7 TeV, to confirm of the soft physics issue. They are shown in Figure 3.29 where the same trend as in Figure 3.28 is observed.

To understand if the calibration applied is the reason of the observed discrepancy, $\sum E_T$ has also been studied in minimum bias events at the EM scale and after applying global calibrations. Figure 3.30 shows the $\sum E_T$

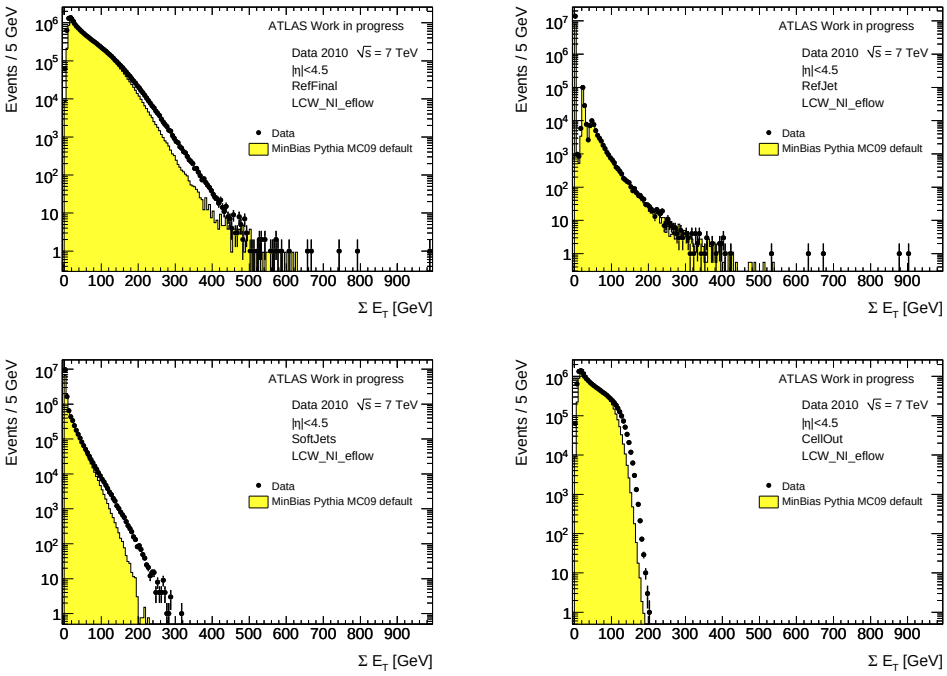

Figure 3.29: *(top left) $\sum E_T$ distributions for $\sqrt{s}$= 7 TeV minimum bias events. LCW_NI_eflow calibration is applied. $\sum E_T$ for jets (top right), soft jets (bottom left) and CellOut (bottom right) terms are also shown. The expectation from MC simulation is superimposed (histogram) and normalised to the number of events in data.*

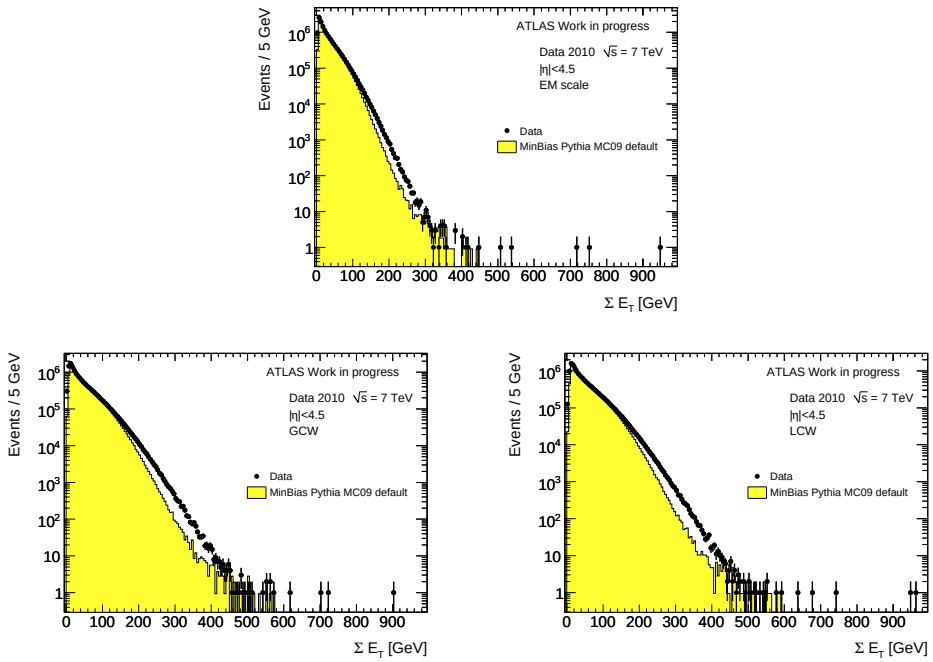

Figure 3.30: *$\sum E_T$ distributions for $\sqrt{s}$= 7 TeV minimum bias events obtained from topoclusters cells at the EM scale (top) and global calibrated with GCW (bottom left) and LCW (bottom right). The Monte Carlo simulation is obtained with the standard PYTHIA tuning. The expectation from MC simulation is superimposed (histogram) and normalised to the number of events in data.*

distributions for 7 TeV minimum bias events at EM scale, with GCW calibration and with LCW calibration. Data spectra are systematically harder than Monte Carlo simulation. The discrepancy amounts to more than 80% for $E_T^{miss} > 120$ GeV ($E_T^{miss} > 180$) at EM scale (calibrated with LCW or GCW).

There are significant hints that the motivation of this disagreement lies in the tuning of the underlying event (UE) component of the PYTHIA Monte Carlo simulation to which the data are compared.

Figure 3.31 and 3.32 show the same data distributions as in Figure 3.30 and 3.29 (respectively) but compared to a Monte Carlo simulated sample with enhanced underlying event activity in PYTHIA. In particular, the PARP90 parameter value is set to 0.16, instead of the default 0.25 [49, 56]. The agreement of data and simulation improves but the simulation spectra tend now to be harder than data up to 40%. This indicates that the UE tuning has to be refined. Nevertheless these preliminary results indicate that the problem lies in the underlying event tuning in the Monte Carlo.

3.8 ϕ distributions

As already said, large energy fluctuations in the calorimeter or muon mismeasurements can produce large $E_{\mathrm{T}}^{miss,\mathrm{Fake}}$. In general, for events with genuine missing transverse energy, the E_T^{miss} angular resolution will depend on the relative fraction of $E_{\mathrm{T}}^{miss,\mathrm{Fake}}$ and on the event topology. For values of $E_{\mathrm{T}}^{miss,\mathrm{True}}$ below 40 GeV, the accuracy of the measurement of the direction degrades rapidly. In contrast, for high values of $E_{\mathrm{T}}^{miss,\mathrm{True}}$, azimuthal accuracies better than 100 mrad are achieved [11].

Detector inefficiencies may perturb the radial symmetry of the physics events. Thus, observations of ϕ asymmetries in reconstructed variables may be a hint of instrumental problems. In case of jet events measuring $\Delta\phi(jet - E_T^{miss}) = \pi$ can be an indication of $E_{\mathrm{T}}^{miss,\mathrm{Fake}}$due to the loss of the second jet, while $\Delta\phi(jet - E_T^{miss}) = 0$ can be due to mismeasurement of the jet energy. Thus a $\Delta\phi$ cut can be used to remove $E_{\mathrm{T}}^{miss,\mathrm{Fake}}$ events as already said in Section 3.4.1.

In general a ϕ asymmetry is observed in E_T^{miss}: Figure 3.33 shows the E_T^{miss} ϕ distribution in minimum bias events. A modulation is visible in Monte Carlo (due to the increased material of $\sim 5\%$ to 10% in the upper half of the detector that was added into the simulation). It is much more evident in data at 7 TeV. Even removing the region where the small forward calorimeter misalignment described in Section 3.3.2 is present does not recover completely the effect.

E_T^{miss} is calculated assuming the primary vertex to be in the origin of

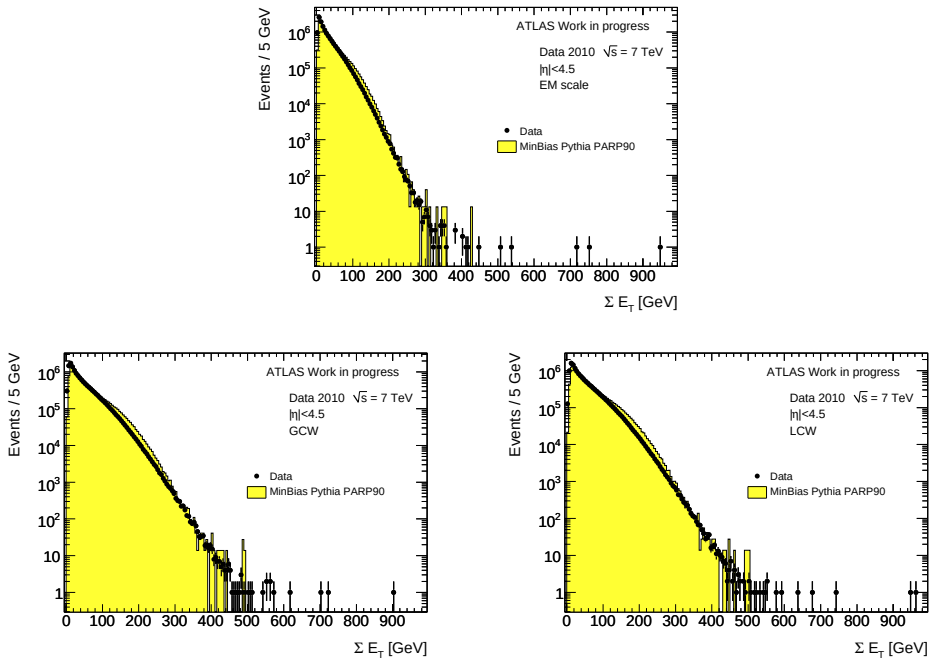

Figure 3.31: *$\sum E_T$ distributions for $\sqrt{s}$= 7 TeV minimum bias events obtained from topoclusters cells at the EM scale (top) and global calibrated with GCW (bottom left) and LCW (bottom right). The Monte Carlo simulation is obtained with the different tuning of PYTHIA UE component (PARP90=0.16) with respect to the default (PARP90=0.25). The expectation from MC simulation is superimposed (histogram) and normalised to the number of events in data.*

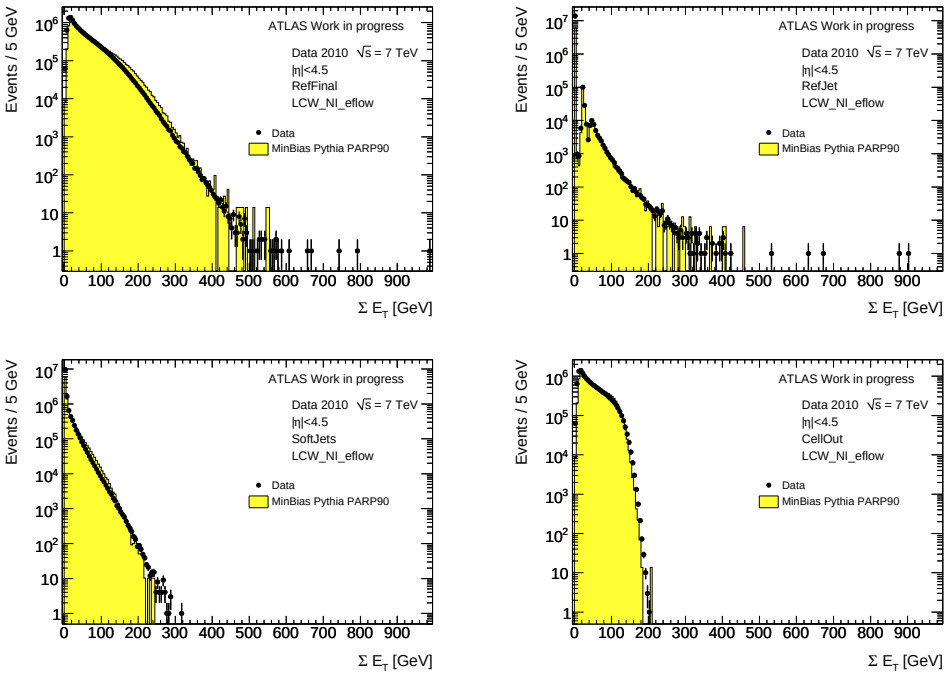

Figure 3.32: *(top left) $\sum E_T$ distributions for $\sqrt{s}$= 7 TeV minimum bias events. LCW_NI_eflow calibration is applied. $\sum E_T$ for jets (top right), SoftJets (bottom left) and CellOut (bottom right) terms are also shown. The Monte Carlo simulation is obtained with a different tuning of PYTHIA UE component (PARP90=0.16) with respect to the default (PARP90=0.25). The expectation from MC simulation is superimposed (histogram) and normalised to the number of events in data.*

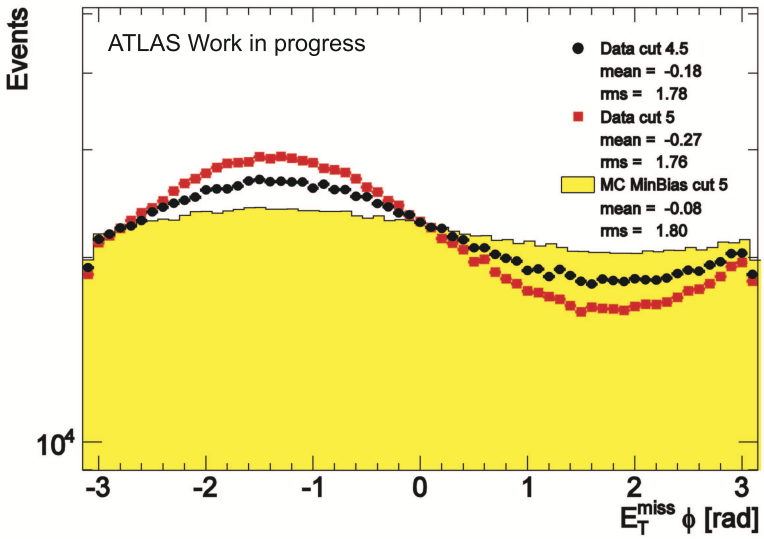

Figure 3.33: E_T^{miss} *ϕ distribution in minimum bias events in* $|\eta| < 5$ *(red) and in* $|\eta| < 4.5$ *(black). The expectation from MC simulation is superimposed (histogram) and normalised to the number of events in data.*

the coordinate system, thus to remove the effect of the different beam spot description in the simulation, E_T^{miss} has been reconstructed from the reconstructed primary vertex but no significant improvement has been found in the ϕ distribution. The hypothesis is that the observed ϕ asymmetry is a feature of the asymmetry of the detector.

3.9 Pileup effects

The effects of pileup (described in Section2.2) on E_T^{miss} have also been analysed. First the impact on E_T^{miss} resolution has been studied. Figure 3.34 shows the E_T^{miss} resolution for events with at least 1 jet with $p_T > 20$ GeV and for events with 2 jets with $p_T > 20$ GeV, applying the LCW_NI_eflow calibration scheme, in case of events with only one primary vertex, two primary vertices and more than two primary vertices. The presence of pileup does not degrade the E_T^{miss} resolution, in fact the scale factors for events with no pileup are very similar if not identical to the ones for events with many vertices. It is also evident from Figure 3.34 that events with many vertices reach higher $\sum E_T$ values due to their higher particle activity.

The presence of pileup has a strong impact on the distribution of E_x^{miss}, E_y^{miss} and therefore E_T^{miss}. Figures 3.35 and 3.36 show E_T^{miss} and its com-

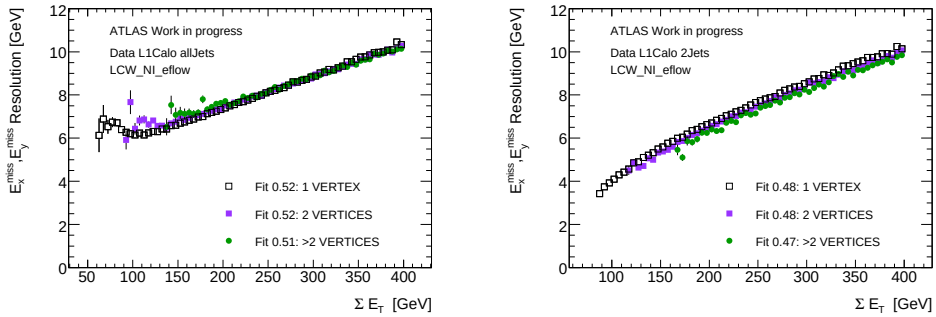

Figure 3.34: *E_x^{miss} and E_y^{miss} resolution as a function of $\sum E_T$ for data taken at $\sqrt{s}$= 7 TeV for events with at least 1 jet with $p_T > 20$ GeV (left) and for events with 2 jets with $p_T > 20$ GeV (right). E_x^{miss}, E_y^{miss}, $\sum E_T$ are computed with topocluster cells using LCW_NI_eflow calibration scheme. Distributions for events with one primary vertex, 2 primary vertices and more than 2 primary vertices are compared. The $\sum E_T$ on the x-axis is taken at the same scale to which E_x^{miss}, E_y^{miss} are reconstructed.*

ponents distributions in events with only one primary vertex, two and more than two primary vertices. The mean value of the E_T^{miss} distribution is about 10% larger in case of two vertices and about 20% in case of more than two vertices, as documented in Figure 3.35. This E_T^{miss} degradation has to be taken into account when applying a E_T^{miss} cut or when using E_T^{miss} in physics measurement such as mass reconstruction, because it can degrade the mass resolution.

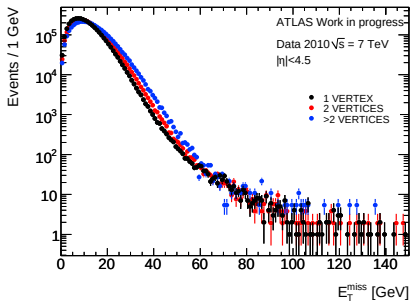

Figure 3.35: *E_T^{miss} distributions for data taken at $\sqrt{s}$= 7 TeV. Events with one primary vertex, 2 primary vertices and more than 2 primary vertices are compared.*

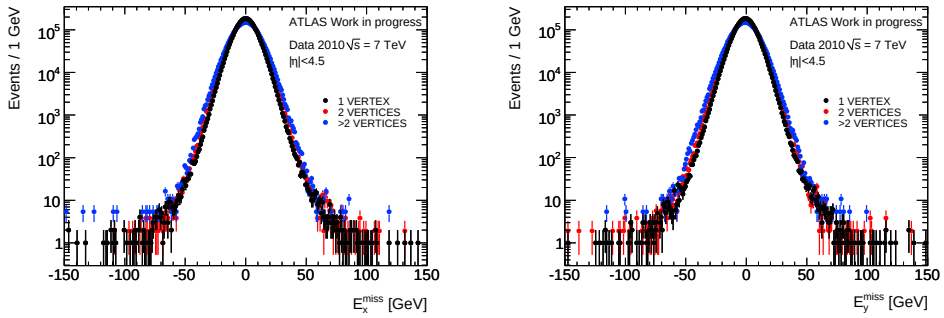

Figure 3.36: *E_x^{miss} (left) and E_y^{miss} (right) distributions for data taken at $\sqrt{s}$= 7 TeV. Events with one primary vertex, 2 primary vertices and more than 2 primary vertices are compared.*

3.10 E_T^{miss} systematics

A complete study of the E_T^{miss} systematics uncertainties have not yet been done. It represents an important step forward to complete the work presented in this thesis.

Since E_T^{miss} is obtained from all the reconstructed physics objects and also from energy deposits outside physics objects, its systematics is determined by the systematics of the different objects and also to the systematics in the measurement of cells outside physics objects.

At the moment in ATLAS the systematics on electrons energy scale have been estimated to be of about 1-2%. Concerning jets, taking into account all the sources, the EMJES systematic uncertainty varies between 10% for jets with p_T between 20 and 100 GeV and 6.5%(7%) for jets with $p_T > 100$ GeV in the central (endcap) region (see Section 2.4.4 and [54]). For calibrated jets the JES systematics have still to be provided. The systematics for τs have still to be provided and are expected to be slightly smaller than the systematics on jets.

The calculation of the systematics for the cells outside physics objects is in progress. It is very important for events where the CellOut contribution is large compared to the contributions of other objects, as possible in W and Z events. .

Chapter 4

E_T^{miss} scale

Another important issue for the E_T^{miss} measurement is the determination of the absolute E_T^{miss} scale. The knowledge of the absolute energy scale over the full pseudorapidity coverage, including the forward calorimeter, is of main interest for physics involving an accurate E_T^{miss} measurement.

The E_T^{miss} scale can be determined from the study of the shape of the lepton-neutrino transverse mass distribution in $W \to l\nu$ events with the already available statistics of data at 7 TeV collected by ATLAS ($\sim$ 45 pb^{-1}).

Later, with at least 100 pb^{-1} of data, the scale can be cross-checked using $Z \to \tau\tau$ events since the $\tau\tau$ invariant mass distribution, obtained using the collinear approximation described in Section 1.2.2, is very sensitive to E_T^{miss}.

In this Section preliminary results of the E_T^{miss} scale determination from $W \to l\nu$ events in data and Monte Carlo are shown. A detailed Monte Carlo based study to measure the E_T^{miss} scale from $Z \to \tau\tau$ events performed on simulated events at 10 TeV is also presented.

4.1 E_T^{miss} scale determination from $W \to l\nu$ events

As described in Section 1.2.2, W boson decays to leptons are channels with genuine E_T^{miss} and thus they are very interesting to study E_T^{miss} performance.

In this Section a preliminary study of E_T^{miss} performance in $W \to e\nu$ and $W \to \mu\nu$ events is presented. The main goal is the development of the method for the estimation of the E_T^{miss} scale.

The data sample used corresponds to an integrated luminosity of $\sim$ 2800 nb^{-1} ($\sim$ 10200 nb^{-1}) for $W \to e\nu$ ($W \to \mu\nu$) channel, collected during

periods od stable of pp collisions with nominal magnetic field conditions and with the detectors operating in good conditions.

Monte Carlo samples at $\sqrt{s} = 7$ TeV for both channels were generated with PYTHIA and consist of $\sim$ 700000 events both for $W \to e\nu$ and for $W \to \mu\nu$ channel.

4.1.1 Event selection

For both data and Monte Carlo an event selection very similar to the one applied in [5] is used:

- **Electrons for $W \to e\nu$ analysis**
  Electron candidates selected with the identification level *tight* (according to the algorithm described in Section 2.4.2) are required to have a cluster $E_T > 20$ GeV within the range $|\eta| < 2.47$, excluding the transition region between the barrel and end-cap calorimeters ($1.37 < |\eta| < 1.52$). No isolation criteria are applied. Only the highest p_T electron per event is considered.

- **Muons for $W \to \mu\nu$ analysis**
  Muon candidates are selected according to the `Staco` algorithm described in Section 2.4.3. They are required to be combined muons with $p_T > 20$ GeV and to have a muon-spectrometer track with $p_T > 10$ GeV within the range $|\eta| < 2.4$. To increase the robustness against track reconstruction mismatches, the difference between the inner-detector and muon-spectrometer p_T, is required to be less than 15 GeV. A track-based isolation defined as the sum of the transverse momenta of tracks with $p_T > 1$ GeV in the inner detector within a cone of $\Delta R < 0.4$ around the muon track, divided by the p_T of the muon, is considered. An isolation requirement of $\sum p_T^{ID}/p_T < 0.2$ is imposed in the muon selection.

  Furthermore, to be more consistent with the E_T^{miss} objects selection criteria, events are rejected if the distance between the muon candidate and any reconstructed jet is within $\Delta R = 0.3$. Only the highest p_T muon per event is considered.

- E_T^{miss}
  The refined calibrated E_T^{miss} is used in the best configuration (described in Sections 3.6.4, the LCW_NI_eflow). E_T^{miss} is required to be above 25 GeV.

Only events with one primary vertex have been used, so events with pileup are not considered in the following. Since different data periods have

been considered for the $W \to e\nu$ and $W \to \mu\nu$ analyses, requiring only one vertex rejects 45%(75%) of data for $W \to e\nu$ ($W \to \mu\nu$) case.

After applying this selection 3715 (3003) events are collected for the $W \to e\nu$ ($W \to \mu\nu$) channel. These numbers are compatible with the number of events selected in [5], taking into account the effect of different statistics and the single vertex requirement.

For Monte Carlo simulation after the selection criteria $\sim$ 200000 events are collected for each lepton channel.

4.1.2 E_T^{miss} in $W \to l\nu$ events

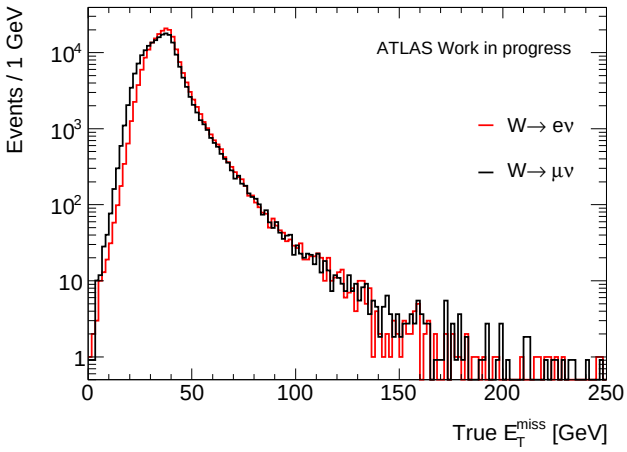

Figure 4.1: $E_{\mathrm{T}}^{miss,\mathrm{True}}$ *distribution in Monte Carlo* $W \to e\nu$ *events (black) and* $W \to \mu\nu$ *(red) at particle level after lepton selection.*

The $E_{\mathrm{T}}^{miss,\mathrm{True}}$ spectrum, as obtained from the Monte Carlo particle level stable and non-interacting truth particles, for events passing the lepton selection criteria described in Section 4.1.1 can be seen in Figure 4.1 for both channels, while Figure 4.2 shows the reconstructed Monte Carlo p_T distribution of the electron (muon) passing the selection cuts for the $W \to e\nu$ ($W \to \mu\nu$) analysis. Both the $E_{\mathrm{T}}^{miss,\mathrm{True}}$ and the lepton p_T distributions are slightly different in the two channels. This is due to the different lepton selections applied in the two analyses.

E_T^{miss} in $W \to e\nu$ events

Figure 4.3 shows the distributions of E_T^{miss} and $\sum E_T$ for data and $W \to e\nu$ Monte Carlo passing the selection criteria and an additional cut on the trans-

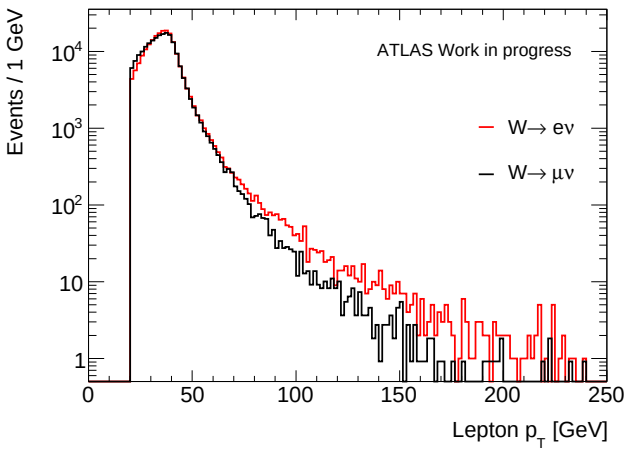

Figure 4.2: *Reconstructed lepton p_T distribution in Monte Carlo $W \rightarrow e\nu$ events (black) and $W \rightarrow \mu\nu$ (red) after lepton selection.*

verse mass, $m_T(electron, E_T^{miss}) > 50$ GeV. As expected $W \rightarrow e\nu$ events have high E_T^{miss} values with respect to relative low $\sum E_T$ values. E_T^{miss} distribution shows a peak for $E_T^{miss} = 40$ GeV that is due to the presence of the neutrino (see Figure 4.1). The E_T^{miss} data-Monte Carlo agreement is acceptable, taking into account that the Monte Carlo for signal events only is used, while the data contain also background events, estimated [5] to be $\sim 7\%$ after lepton, E_T^{miss} and m_T cuts. For data E_T^{miss} distributions one event has $E_T^{miss} > 150$ GeV. This is not surprising since the $E_{\mathrm{T}}^{miss,\mathrm{True}}$ spectrum reaches this energy. Nevertheless there are indications that such outliers are not due to mismeasured or lost high-p_T jets. The $\sum E_T$ distribution shows a disagreement that has already been discussed in Section 3.7.

In Figure 4.4 the main contributions to E_T^{miss} in $W \rightarrow e\nu$ events are shown: E_T^{miss} from electrons, jets, soft jets and E_T^{miss} from cells outside physics objects. The main contribution is from the electron term as expected. Also, the jet term is significant due to the fact that in 20% of the cases W bosons are produced together with high p_T jets as can also be seen by the two-peaks shape: the E_T^{miss}=0 GeV peak is due to events with no jets while the one starting from E_T^{miss}=20 GeV is due to events with jets. The region between the two peaks is due to events where a high p_T jet is overlapped with an electron. In such cases in E_T^{miss} algorithm electron topoclusters are identified and assigned to the electrons term while the residual deposits are assigned to the jet term.

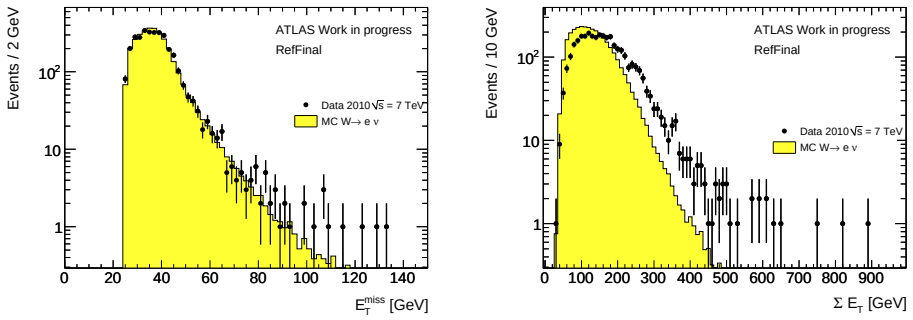

Figure 4.3: E_T^{miss} *(left) and* $\sum E_T$ *(right) distributions. The expectation from* $W \to e\nu$ *Monte Carlo simulation is superimposed (histogram) and normalised to the number of events in data.*

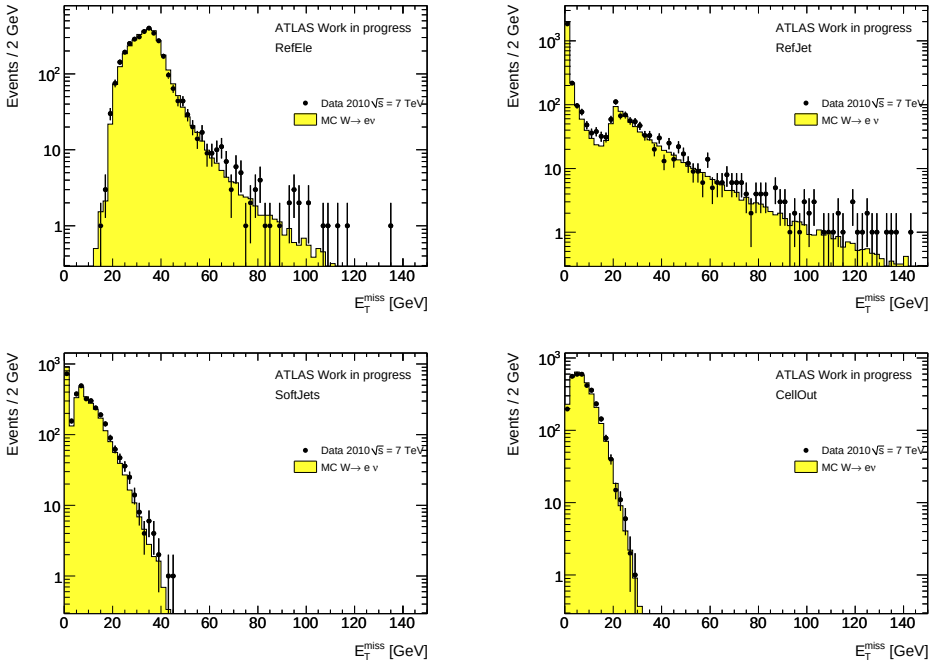

Figure 4.4: E_T^{miss} *distributions for* $\sqrt{s}$*= 7 TeV* $W \to e\nu$*. LCW_NI_eflow calibration is applied.* E_T^{miss} *from electrons (top left), jets (top right), soft jets (bottom left) and CellOut (bottom right) terms are also shown. The expectation from MC simulation is superimposed (histogram) and normalised to the number of events in data.*

The average p_T of the charged lepton and the neutrino in $W \rightarrow l\nu$ events are expected to be the same, so their relative distributions have been studied. Figure 4.5 shows the ratio $R = p_{T(ele)}/E_T^{miss}$ for events passing all the selection cuts. This variable should be ~ 1, but its distribution is distorted by the kinematic and acceptance requirements on the charged leptons. In particular 5‰ of the events have $R > 3$.

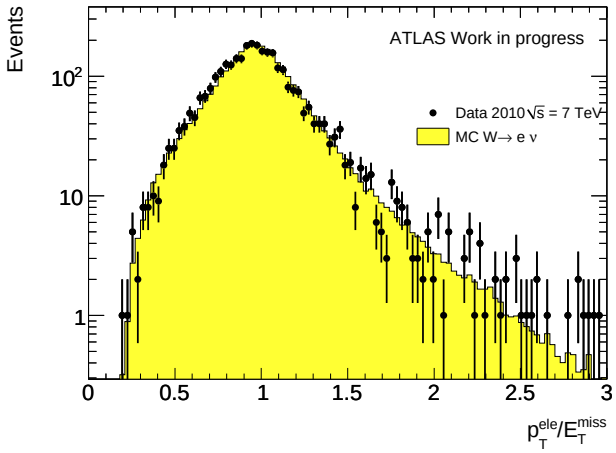

Figure 4.5: *Ratio electron p_T to E_T^{miss} in data and $W \rightarrow e\nu$ Monte Carlo simulation. The expectation from MC simulation is superimposed (histogram) and normalised to the number of events in data.*

E_T^{miss} in $W \rightarrow \mu\nu$ events

For the muon channel the same distributions as for the $W \rightarrow e\nu$ channel have been studied.

Figure 4.6 shows the distributions of E_T^{miss} and $\sum E_T$ for data and $W \rightarrow \mu\nu$ Monte Carlo passing the selection criteria and the $m_T(\mu, E_T^{miss}) > 50$ GeV cut. They show the same trends as those in $W \rightarrow e\nu$ events.

In Figure 4.7 the main contributions to E_T^{miss} in $W \rightarrow \mu\nu$ events are shown: E_T^{miss} from muons, jets, soft jets and E_T^{miss} from cells outside physics objects. The most important contribution to E_T^{miss} is due to the muons term as expected. Three events in data have $E_T^{miss} < 20$ GeV for the muon term despite the requirement of muon $p_T > 20$ GeV. They are both due to the small discrepancy between the analysis muon selection criteria and E_T^{miss} muon selection criteria and to other muons that may be present in the events entering in E_T^{miss} muon term calculation. As for $W \rightarrow e\nu$, the

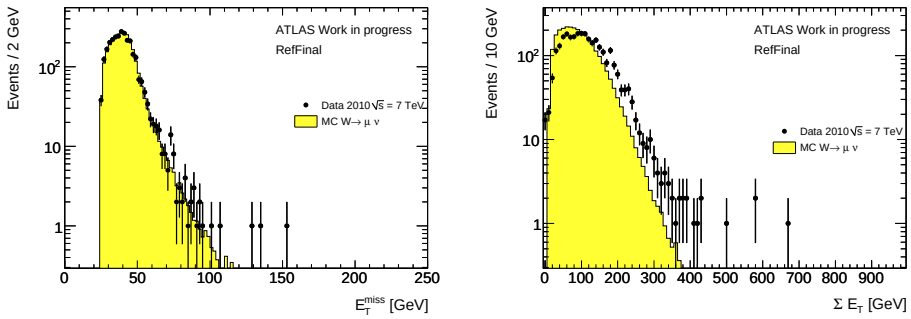

Figure 4.6: *E_T^{miss} (left) and $\sum E_T$ (right) distributions. The expectation from $W \to \mu\nu$ Monte Carlo simulation is superimposed (histogram) and normalised to the number of events in data.*

jet contribution is also important and the two-peak shape is again clearly visible. The overall agreement in all the contribution distributions is good.

The ratio $R = p_{T(\mu)}/E_T^{miss}$ is shown in Figure 4.8, no events have $R > 3$.

4.1.3 E_T^{miss} performance in $W \to l\nu$ events

To evaluate the E_T^{miss} reconstruction performance in $W \to l\nu$ events, both E_T^{miss} resolution, defined in Equation 3.5, and E_T^{miss} linearity, defined in Equation 3.6, have been studied.

E_T^{miss} performance in $W \to e\nu$ events

$E_{x,y}^{miss}$ resolution curves for the Monte Carlo simulated $W \to e\nu$ events are shown in Figure 4.9 for all the different calibration configurations described in Sections 3.6.1 and 3.6.2. For the LCW_NI_eflow configuration the resolution can be described with:

$$\sigma(E_{x,y}^{miss,\mathrm{True}} - E_{x,y}^{miss}) = 0.4 \times \sqrt{\sum E_{\mathrm{T}}}. \tag{4.1}$$

The linearity in Monte Carlo simulated $W \to e\nu$ events is shown in Figure 4.10 for the different calibration configurations. For LCW_NI_eflow configuration the linearity, $(E_{\mathrm{T}}^{miss,\mathrm{True}} - E_T^{miss})/E_{\mathrm{T}}^{miss,\mathrm{True}}$ is not constant: it is overestimated for $E_{\mathrm{T}}^{miss,\mathrm{True}} < 25$ GeV, then it is underestimated in the range 25-60 GeV, finally for $E_{\mathrm{T}}^{miss,\mathrm{True}} > 60$ GeV it is restored to 0.

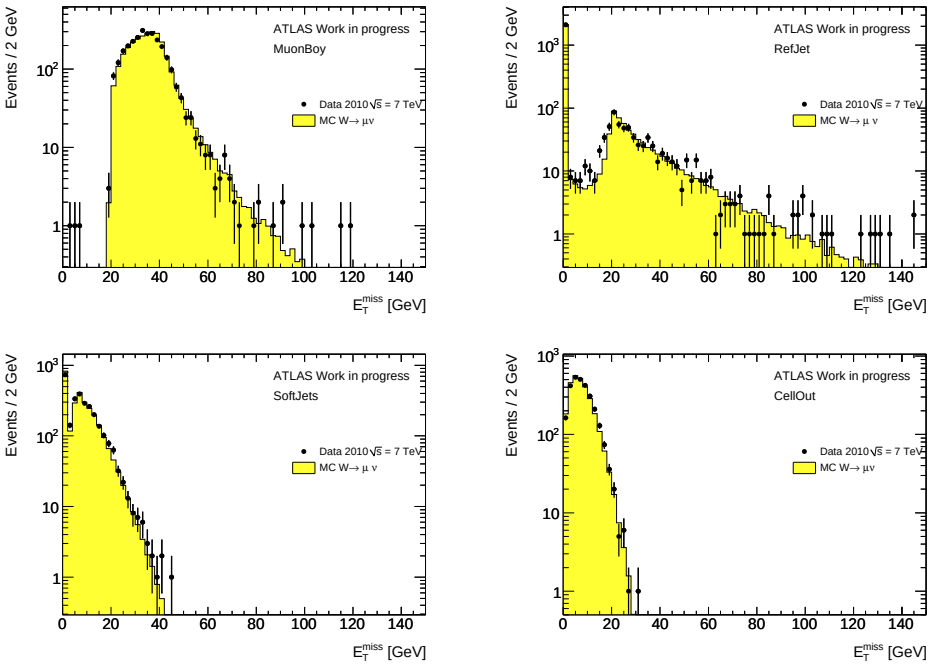

Figure 4.7: *E_T^{miss} distributions for $\sqrt{s}$= 7 TeV $W \rightarrow \mu\nu$. LCW_NI_eflow calibration is applied. E_T^{miss} from muons (top left), jets (top right), soft jets (bottom left) and CellOut (bottom right) terms are also shown. The expectation from MC simulation is superimposed (histogram) and normalised to the number of events in data.*

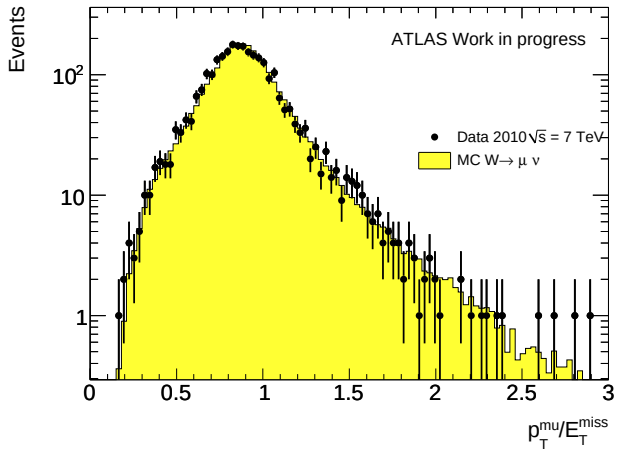

Figure 4.8: *Ratio muon p_T to E_T^{miss} in data and $W \to \mu\nu$ Monte Carlo simulation. The expectation from MC simulation is superimposed (histogram) and normalised to the number of events in data.*

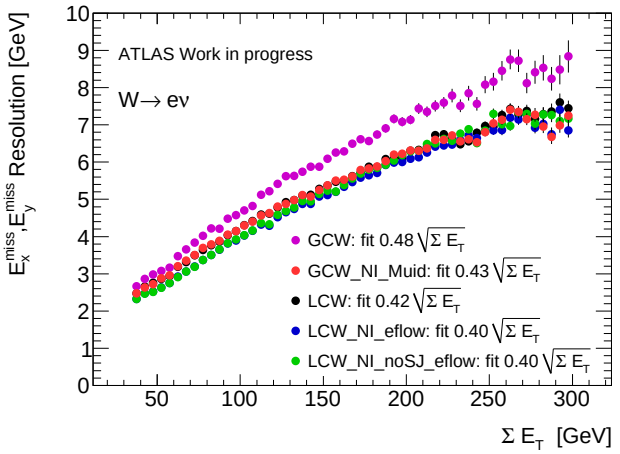

Figure 4.9: *E_x^{miss} and E_y^{miss} resolution as a function of the total transverse energy ($\sum E_T$) for $W \to e\nu$ Monte Carlo simulated events. E_x^{miss}, E_y^{miss}, $\sum E_T$ are computed with different calibration schemes. The $\sum E_T$ on the x-axis is taken at the same scale to which E_x^{miss}, E_y^{miss} are reconstructed.*

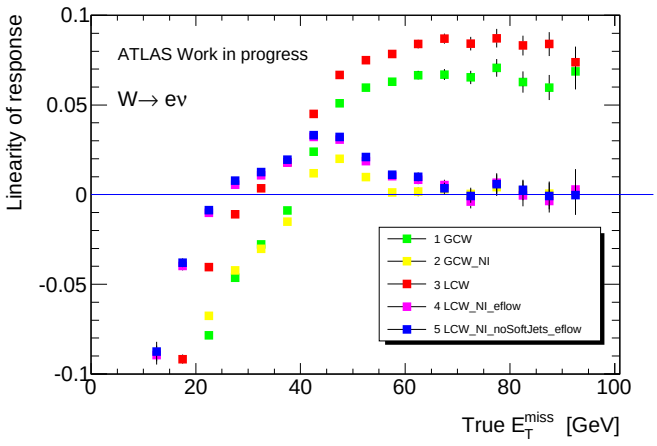

Figure 4.10: E_T^{miss} *linearity in Monte Carlo* $W \rightarrow e\nu$ *events. Results for different calibration configurations are compared.*

E_T^{miss} performance in $W \rightarrow \mu\nu$ events

Also for $W \rightarrow \mu\nu$ events $E_{x,y}^{miss}$ resolution curves for all the different calibration configurations have been studied and are shown for the Monte Carlo simulation in Figure 4.11

For the LCW_NI_eflow configuration the resolution is found to be:

$$\sigma(E_{x,y}^{miss,\mathrm{True}} - E_{x,y}^{miss}) = 0.5 \times \sqrt{\sum E_{\mathrm{T}}}. \tag{4.2}$$

The linearity in Monte Carlo simulated $W \rightarrow \mu\nu$ events is shown in Figure 4.12 for the different calibration configurations. $W \rightarrow \mu\nu$ events seem to be much less linear than $W \rightarrow e\nu$ ones. For LCW_NI_eflow configuration the linearity for $E_T^{miss} > 25$ GeV is found to be negative, improving with the increasing of E_T^{miss} from -0.08 for $E_{\mathrm{T}}^{miss,\mathrm{True}}$ =25 GeV to ~ 0 for $E_{\mathrm{T}}^{miss,\mathrm{True}} >$ 90 GeV.

This worst performance is due to a problem in the calculation of the energy lost by muons in the calorimeters that enters in E_T^{miss} calculation. As described in Section 3.1, for isolated muons as used in this analysis, the muon energy is determined from the combined measurement of the inner detector and muon spectrometer and the energy lost by the muon in the calorimeters ($E_{x(y)}^{miss,\mathrm{calo},\mu}$) is not added to the E_T^{miss} calorimeter term. In the reconstruction version of data and Monte Carlo used for this study, $E_{x(y)}^{miss,\mathrm{calo},\mu}$ is not accounting for all the energy that the muons deposit in the calorimeters because only the energy of cells along the muon trajectory are considered. This results in higher values of the reconstructed E_T^{miss} as it

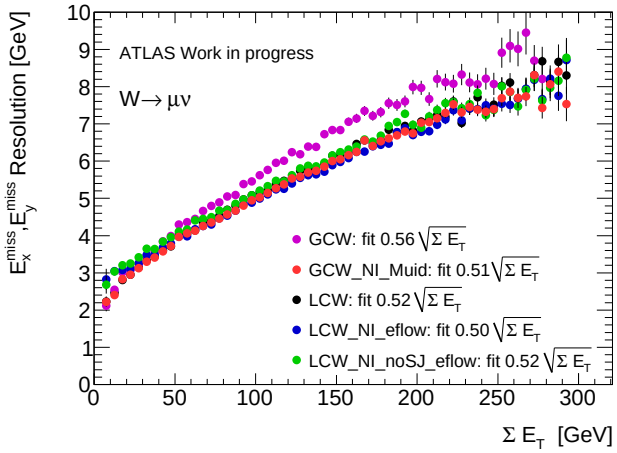

Figure 4.11: *E_x^{miss} and E_y^{miss} resolution as a function of the total transverse energy ($\sum E_T$) for $W \to \mu\nu$ Monte Carlo simulated events. E_x^{miss}, E_y^{miss}, $\sum E_T$ are computed with different calibration schemes. The $\sum E_T$ on the x-axis is taken at the same scale to which E_x^{miss}, E_y^{miss} are reconstructed.*

can be seen in Figure 4.13 where for both $W \to l\nu$ channels in Monte Carlo events passing the full selection criteria, the $E_{\mathrm{T}}^{miss,\mathrm{True}}$ and the reconstructed E_T^{miss} distributions are shown. For $W \to e\nu$ events E_T^{miss} is very similar to $E_{\mathrm{T}}^{miss,\mathrm{True}}$ while for $W \to \mu\nu$ E_T^{miss} is shifted towards higher values with respect to the $E_{\mathrm{T}}^{miss,\mathrm{True}}$.

4.1.4 E_T^{miss} scale determination method

$W \to e\nu$ analysis

A method using the shape of the reconstructed transverse mass of the W boson (m_T, defined in Equation 1.6) has been studied. This method, based on the analysis presented in [11], is sensitive to both the E_T^{miss} resolution and the scale. The m_T is reconstructed from Monte Carlo simulated data under the hypothesis that E_T^{miss} is completely due to the neutrino momentum p_T^{ν}. The m_T distribution is fitted in a χ^2 test fit that uses template histograms. The template histograms of the m_T distributions are generated by convolving the true transverse mass distribution with the E_T^{miss} response:

$$E_{x,y\,\mathrm{smeared}}^{miss} = \alpha\, p_T^{\nu} \oplus Gauss(0,\sigma) \tag{4.3}$$

where parameters α and σ are the E_T^{miss} scale and resolution (in GeV), respectively, taken from Monte Carlo.

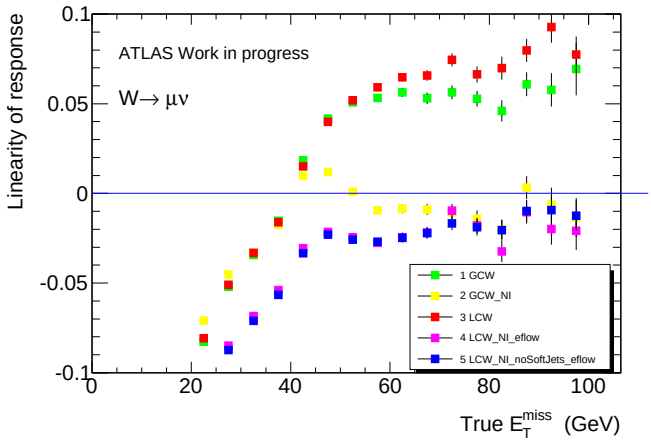

Figure 4.12: E_T^{miss} *linearity in Monte Carlo* $W \rightarrow \mu\nu$ *events. Results for different calibration configurations are compared.*

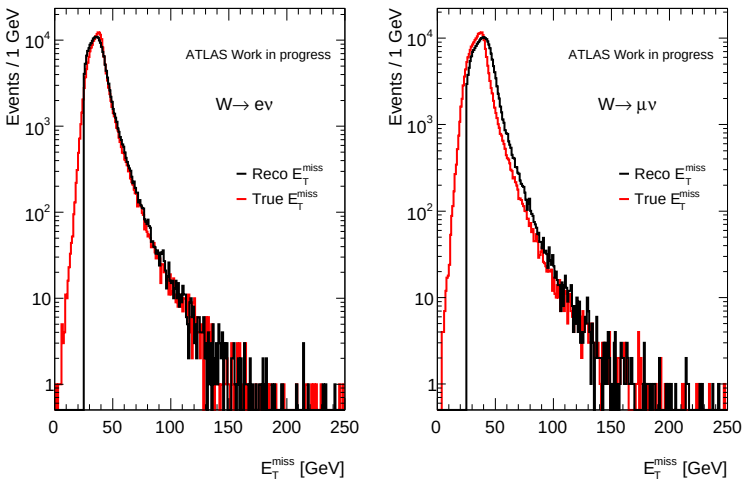

Figure 4.13: $E_{\mathrm{T}}^{miss,\mathrm{True}}$ *and reconstructed* E_T^{miss} *distributions in MC* $W \rightarrow e\nu$ *(left) and* $W \rightarrow \mu\nu$ *(right) events passing the analysis cuts.*

Firstly we have checked the agreement between the m_T distributions in data and simulation, when using simulated reconstructed E_T^{miss} in order to be able to rely on the Monte Carlo prediction. Figure 4.14 shows the m_T of

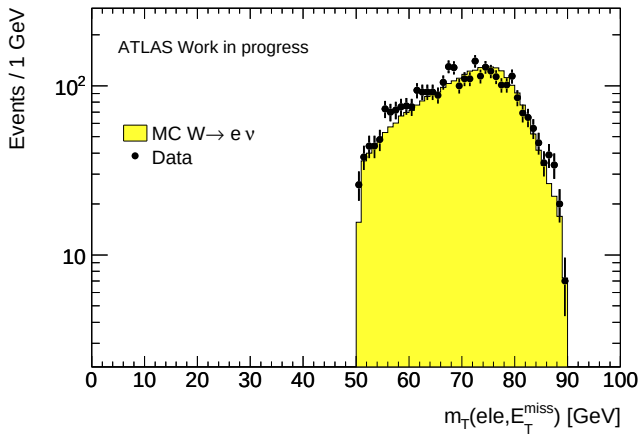

Figure 4.14: *Distributions of the transverse mass, m_T, of the electron-E_T^{miss} system in the mass range 50-90 GeV. The expectation from Monte Carlo simulation is superimposed (histogram) and normalised to the number of events in data in the range 65-90 GeV.*

the electron-E_T^{miss} system in the mass range 50-90 GeV where reconstructed E_T^{miss} has been used for $W \to e\nu$ simulated events and for data. Since from Figure 1.2, that has been obtained using a very similar event selection, it is evident that the $\sim 7\%$ background contamination found in the mass range 50-100 GeV is reduced to $\sim 2\%$ in the mass range 65-90 GeV. Therefore Monte Carlo simulation has been normalised to the number of events in data in the range 65-90 GeV to take into account that a signal-only Monte Carlo sample is used. The data-simulation agreement is very good: using a χ^2 test to compare the two distributions the reduced χ^2 is found to be equal to 0.75.

New m_T distributions have been generated smearing $E_{\mathrm{T}}^{miss,\mathrm{True}}$ as in Equation 4.3 with fixed $\sigma = 0.4$ taken from Equation 4.1 and using many different values for the scale factor α.

From Figure 4.1 it is evident that most of the neutrinos have p_T in the range 25-60 GeV, thus we have chosen to use a staring value $\alpha = 0.98$, independent on the E_T^{miss} value. This is based on the linearity of E_T^{miss} reconstruction in this neutrino p_T range, as shown in Figure 4.10. As an example of the many templates considered, Figure 4.15 shows some cases of m_T distributions in Monte Carlo events. Three different shapes are com-

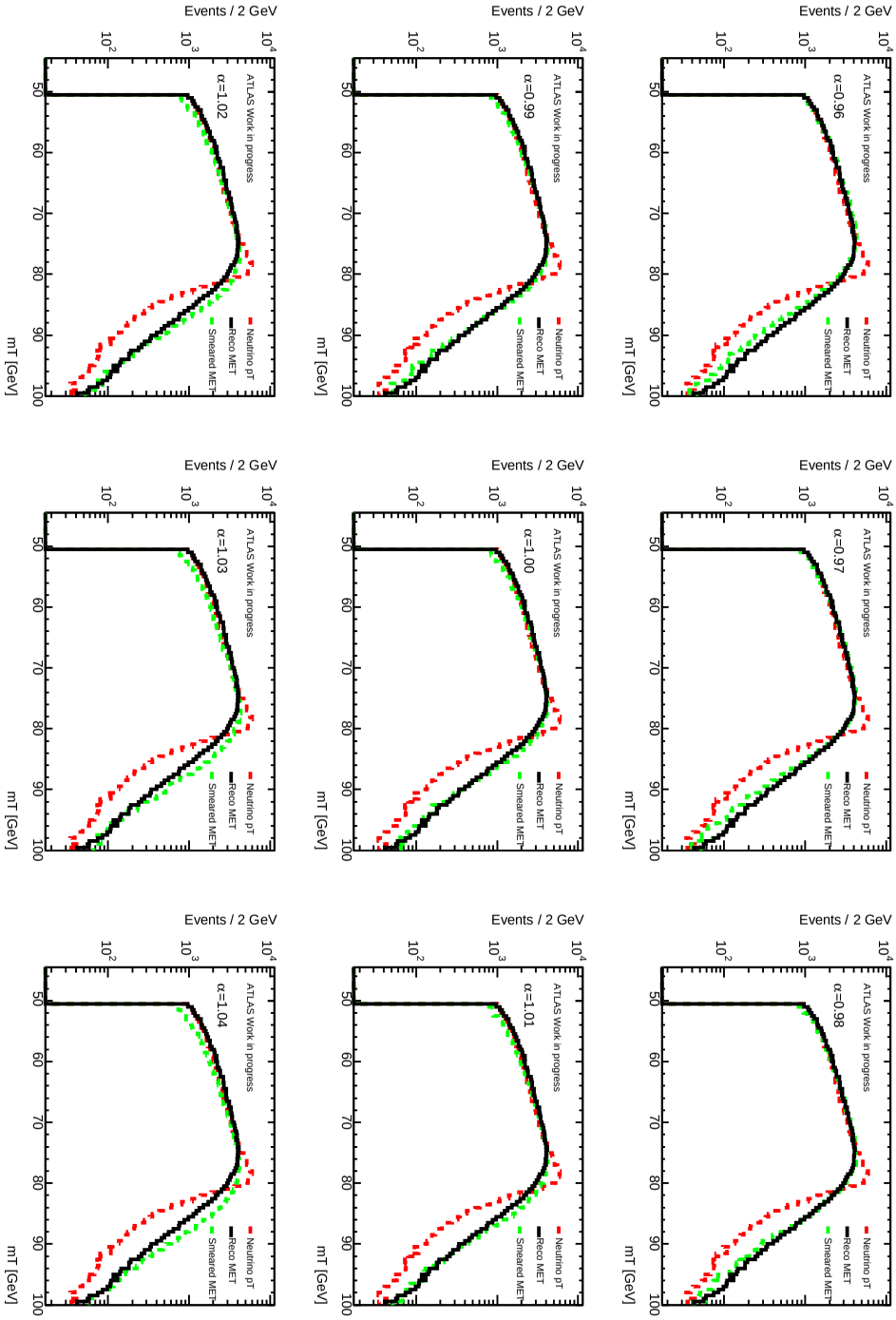

Figure 4.15: *Distributions of the transverse mass, m_T, of the electron-E_T^{miss} system in the mass range 50-100 GeV for MC $W \to e\nu$ events. m_T obtained with $E_{\mathrm{T}}^{miss,\mathrm{True}}$ (red), E_T^{miss}, smeared as in Equation 4.3 (green) and reconstructed $E_T^{miss,\mathrm{rec}}$ (black). Templates are obtained with α values from 0.96 to 1.4 with bin of 0.1.*

pared:

- red curve: $m_T(electron, E_{\mathrm{T}}^{miss,\mathrm{True}})$,
- black curve: $m_T(electron, E_T^{miss})$, where E_T^{miss} is the reconstructed E_T^{miss} calibrated with the LCW_NI_eflow configuration,
- green curve: $m_T(electron, E_T^{miss,\mathrm{smeared}})$, where $E_T^{miss,\mathrm{smeared}}$ is calculated from the two E_T^{miss} components defined in 4.3 where:
  - $\sigma = 0.4$,
  - α takes 9 different values in the range 0.96-1.04 with a step of 0.1.
- the electron p_T is the reconstructed p_T of the electron candidate.

A χ^2 test has been used to estimate the value of α that provides the $E_T^{miss,\mathrm{smeared}}$ which gives the $m_T(electron, E_T^{miss,\mathrm{smeared}})$ shape that best fits $m_T(electron, E_T^{miss})$. Figure 4.17 (left) shows the reduced χ^2 distribution as a function of the scale factor α in the range 0.95-1.45 with a step of 0.002. The minimum of the distribution identifies the best scale factor, i.e. the value entering in $E_T^{miss,\mathrm{smeared}}$ calculation which gives the best shape match. For Monte Carlo simulated events the best scale factor is $\alpha = 0.98 \pm 0.01$ which is fully compatible with results shown in Figure 4.10. The statistics available for this Monte Carlo based test would thus allow to set the E_T^{miss} scale with a precision of 1%, once the E_T^{miss} resolution is known.

The same technique has been repeated with real data using the same $m_T(electron, E_T^{miss,\mathrm{smeared}})$ templates. Figure 4.16 shows the same distributions as in Figure 4.15 for $m_T(electron, E_{\mathrm{T}}^{miss,\mathrm{True}})$ curve (red) and $m_T(electron, E_T^{miss,\mathrm{smeared}})$ (green), while the black curve is the $m_T(electron, E_T^{miss})$ obtained from data using the reconstructed electron p_T and E_T^{miss}.

Figure 4.17 shows the reduced χ^2 distributions as a function of the scale factor α. The scale factor providing the template that best fits data is $\alpha = 0.97 \pm 0.03$. Therefore with the statistics used in this study the precision reached on the E_T^{miss} scale is about 3%, considering statistical errors only and taking a fixed resolution from Monte Carlo.

$W \to \mu\nu$ analysis

The already discussed underestimation of the E_T^{miss} muon term in data and Monte Carlo leads to a non-linearity that does not allow to set the E_T^{miss} scale in this channel. Only a quick check of the method has been done on $W \to \mu\nu$ events.

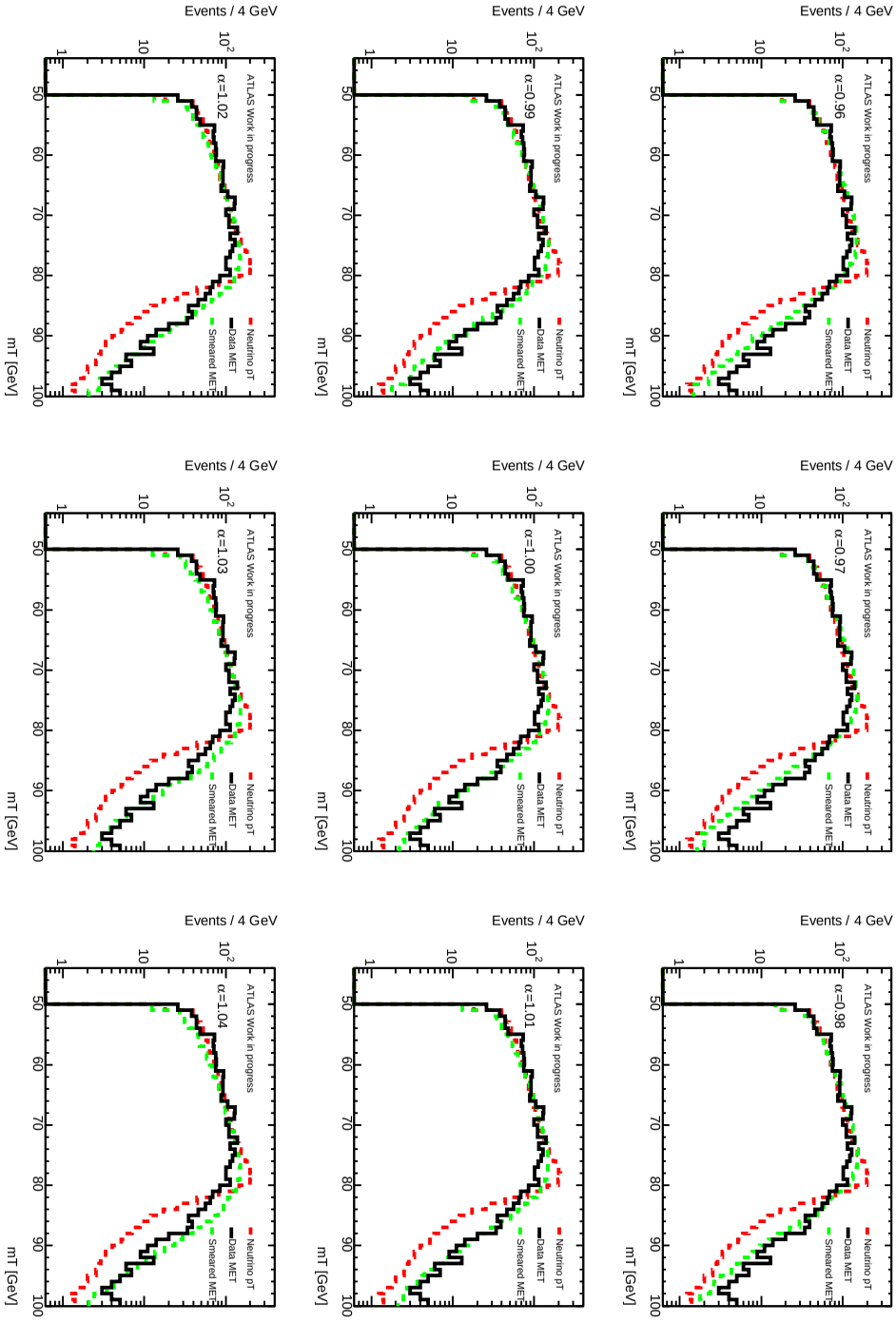

Figure 4.16: *Distributions of the transverse mass, m_T(electron-E_T^{miss}) in the mass range 50-100 GeV for MC $W \to e\nu$ events and data. m_T obtained with $E_{\mathrm{T}}^{miss,\mathrm{True}}$ (red),E_T^{miss}, smeared as in Equation 4.3 (green) and data E_T^{miss} (black). Templates are obtained with α values from 0.96 to 1.4 with bin of 0.1.*

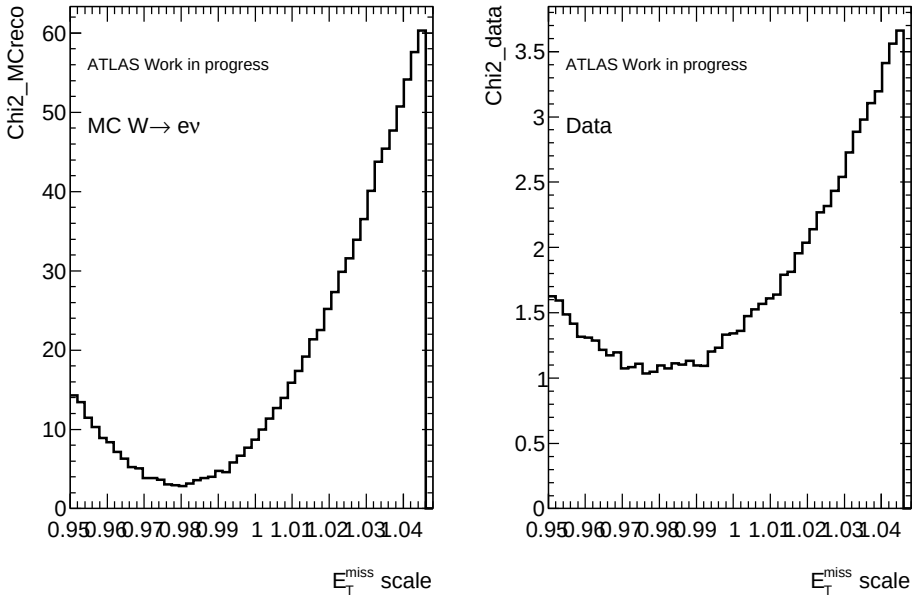

Figure 4.17: *Reduced χ^2 distributions as a function of the linearity scale factor in MC and data for $W \to e\nu$ events.*

For $W \rightarrow \mu\nu$ events a $m_T(muon, E_T^{miss,\text{smeared}})$ has been obtained where $E_T^{miss,\text{smeared}}$ is again calculated as described in Equation 4.3, with $\sigma = 0.5$ from Equation 4.2.

From the linearity curve shown in Figure 4.12 a simple function to described the scale factor α has been extracted, consisting in a linear function of $E_{\text{T}}^{miss,\text{True}}$ for $E_{\text{T}}^{miss,\text{True}} \leq 45$ GeV and in a constant for $E_{\text{T}}^{miss,\text{True}} > 45$ GeV, that is:

$$\left\{ \begin{array}{ll} \alpha = -0.035 \times E_{\text{T}}^{miss,\text{True}} + 1.2 & for\ E_{\text{T}}^{miss,\text{True}} \leq 45\ \text{GeV} \\ \alpha = 1.2 & for\ E_{\text{T}}^{miss,\text{True}} > 45\ \text{GeV} \end{array} \right\} \quad (4.4)$$

The results are shown for Monte Carlo and data E_T^{miss} in Figure 4.18 where three different distributions are compared:

- red curve: $m_T(muon, E_{\text{T}}^{miss,\text{True}})$,
- black curve: $m_T(muon, E_T^{miss})$, where E_T^{miss} is the reconstructed E_T^{miss} calibrated with the LCW_NI_eflow configuration,
- green curve: $m_T(muon, E_T^{miss,\text{smeared}})$, where $E_T^{miss,\text{smeared}}$ is calculated from the two E_T^{miss} components defined in 4.3 where:
  - $\sigma = 0.5$,
  - α is calculated from Equation 4.4.
- the muon p_T is the reconstructed p_T of the muon candidate.

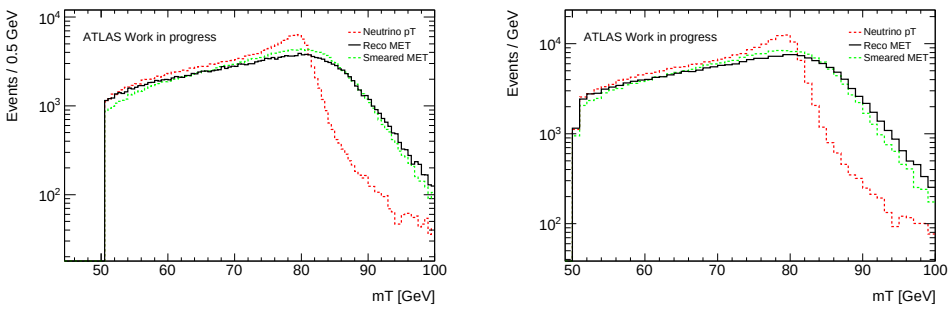

Figure 4.18: *Distributions of the transverse mass, m_T(muon-E_T^{miss}) in the mass range 50-100 GeV for MC $W \rightarrow \mu\nu$ events and data. m_T obtained with $E_{\text{T}}^{miss,\text{True}}$ (red),$E_T^{miss,\text{smeared}}$ as in Equation 4.3 (green) and reconstructed E_T^{miss} (black) from Monte Carlo (left) and data (right).*

The agreement between $m_T(muon, E_T^{miss,\text{smeared}})$ and $m_T(muon, E_T^{miss})$ is not perfect and using the former to fit the latter with a χ^2 test fit, the reduced χ^2 values are found to be $\chi^2 = 12(26)$ for Monte Carlo (data) $m_T(muon, E_T^{miss})$.

These values, faraway from unity, suggest that the scale factor applied must be better modelled and more studies are needed to find the best scale to be applied.

Further studies

This analysis can anyway be improved to reach a more precise measurement of the scale.

- the statistics can be increased using all available ATLAS data that at present corresponds to an integrated luminosity of 45 pb^{-1}. This full statistics can be used provided that the events with pileup can be considered if verified that the pileup does not distort the m_T shape.
- The background subtraction can eventually be performed using the Monte Carlo or data-driven estimations
- Templates can be generated using different resolution factor values together with different scale factor values.
- More refined statistics methods can be used to evaluate the best fit and possible systematics due to the used method.
- The systematics due to the Monte Carlo generator used can be checked using different generators.
- Finally both $W \to e\nu$ and $W \to \mu\nu$ events can be used, when the calculation of $E_T^{\text{miss,calo},\mu}$ will be improved in the E_T^{miss} reconstruction.

4.2 E_T^{miss} scale determination from $Z \to \tau\tau$ events

The $Z \to \tau\tau$ production channel is an important source of events with genuine E_T^{miss} as described in Section 1.2.2.

The decay channel considered in this study is $Z \to \tau\tau \to \ell\tau_h$, where one τ decays to leptons and the second one to a τ-jet and a ν_τ. With an integrated luminosity of 100 pb^{-1} at $\sqrt{s} = 10$ TeV, the $Z \to \tau\tau$ cross section is $\sigma_{Z\to\tau\tau} = 842$ pb^{-1} and the expected event yield for $Z \to \tau\tau \to \ell\tau_h$ is approximately 50 000 events.

However, to obtain a very pure signal sample that is needed for E_T^{miss} study, very severe cuts are necessary to suppress background processes from QCD jet production, $W \to l\nu$, $Z \to ll$, and $t\bar{t}$.

Monte Carlo samples were generated with the PYTHIA generator [49], except for the $t\bar{t}$ samples, where the MC@NLO generator [57] was used. Detector simulation for most samples was done with full GEANT simulation [50], while high statistics QCD jet samples simulated with ATLFAST-II [58] were used to cross check fully simulated lepton filtered QCD samples.

4.2.1 Object selection

The object selection is done in steps that are briefly described in the following.

- **Leptons pre- selection**
  A primary selection of the leptons is performed, with different requirements for electrons, muons and tau candidates:

  - **Muon selection**
    For muon candidates combined `Staco` muons are used (see Section 2.4.3 for details on muons reconstruction and identification). These muon candidates are required to have $p_T > 10$GeV and $|\eta| < 2.5$ and to satisfy $\chi^2_{\text{match}} < 8.0$.
    The efficiency of selecting muons with these criteria is approximately 85%.
  - **Electron selection**
    Electron candidates must fulfill medium cut-based criteria (see Section 2.4.2 for details), which have an approximate efficiency of 75%. These candidates are also required to have $p_T > 10$GeV and $|\eta| < 2.5$. Electrons must satisfy additional tight cut-based criteria with approximate efficiency of 65% for all electrons.
  - **Tau selection**
    Candidates for hadronically decaying τ leptons (see Section 2.4.4) are required to have a track and calorimeter seed and have $E_T^{\text{vis}} >$ 15 GeV and $|\eta| < 2.5$, where E_T^{vis} is the transverse energy of the visible decay products of the τ lepton (which does not include invisible particles such as ν_τ). The τ candidates must pass medium likelihood cuts [59] which is approximately 50% efficient in identifying τ leptons.

    τ candidates must also pass electron and muon vetoes [60].

    For the QCD di-jet samples, τ identification criteria are not applied, rather each τ candidate is weighted by its corresponding fake rate, artificially increasing the effective sample size of the samples. Each candidate is thus treated as an independent event, with its entries scaled by this fake rate weight [61].

- **Overlap removal**
  To avoid cases where the same physical object produces multiple reconstructed candidates, overlap removal is performed between the preselected candidates. Muon, electron, and τ lepton candidates are not permitted to be within a cone radius of $\Delta R < 0.2$ of each other. Should such overlaps exist, then only one candidate is kept, with the assignment of muon, electron, and τ lepton in order of decreasing precedence.

- **Trigger**
  Muons and electrons that are chosen in the preselection step are required to be matched to muon and electron trigger candidates at the event filter level within a cone of $\Delta R = 0.2$. Muon trigger candidates must be found by the event filter with $p_T > 10$ GeV. The electron trigger candidates that are considered are those passing event filter medium identification requirements, with $p_T > 10$ GeV. The triggers are assumed not to be prescaled. Unlike the full simulation samples, ATLFAST-II samples have no simulated trigger decision. In order to simulate the trigger requirement, the lepton trigger efficiency is parametrised as a function of the lepton p_T, using full simulation samples. The events are then weighted by the efficiency given by this parametrisation when running over ATLFAST-II samples [61].

- **Lepton isolation**
  Lepton isolation provides good discrimination between signal and the QCD background.

  Three types of isolation variables were defined equivalently for muons and electrons: `etcone`, `ptcone`, and `nucone`.

  The variables `etcone20` (`etcone30`, `etcone40`) refer to amount of additional calorimeter energy in a cone of $\Delta R < 0.2$ (0.3, 0.4) around the lepton candidate. The variables `ptcone20` (`ptcone30`, `ptcone40`) correspond to the sum of transverse momenta of additional tracks in a cone of $\Delta R < 0.2$ (0.3, 0.4) around the lepton candidate. The variables `nucone20` (`nucone30`, `nucone40`) refer to the number of additional tracks found in a cone of $\Delta R < 0.2$ (0.3, 0.4) around the lepton candidate.

  The isolation criteria chosen for muon candidates was `nucone40` < 1 and `etcone40`$/p_T(\mu) < 0.1$.

  Cuts on `nucone40` < 1 and `etcone30`$/p_T(e) < 0.12$ were chosen as the isolation criteria for electron candidates.

The highest p_T electron or muon candidate that satisfies isolation criteria is then chosen as the candidate lepton for the invariant mass analysis.

Despite applying fake rate weighting on τ candidates, the number of MC events remaining in di-jet background samples (both fully simulated and ATLFAST-II) is still very small. Thus, events were selected with looser isolation and then weighted by factors obtained when comparing loose and tight isolation as a function of the lepton candidate p_T [61].

4.2.2 Analysis cuts

Further cuts are applied to the selected events in order to reduce the background contamination:

- **Transverse mass cut**
  The transverse mass, defined in Equation 1.6, is required to be below 50 GeV ($m_{\mathrm{T}} < 50$ GeV) to discriminate W + jets from $Z \to \tau\tau$.

- **Dilepton veto**

  Another background process that must be suppressed is $Z \to \ell\ell$. These events can fake the $Z \to \tau\tau \to \ell\tau_h$ signature primarily in two ways: one lepton is correctly identified and the other lepton fakes a τ candidate, or one lepton is correctly identified and a hadronic jet fakes a τ candidate.

  Background events in the first case are suppressed by rejecting τ candidates that overlap with identified leptons, and applying dedicated e/μ vetoes in τ identification. Events for the second case can be rejected if the second lepton from $Z \to \ell\ell$ can be identified. A veto on the presence of two or more preselected leptons is applied.

- **Number of tracks and charge**
  Further suppression of background levels is achieved by requiring that the τ candidate be reconstructed with 1 or 3 tracks have unit charge. Then, the product of the charges of the chosen lepton and the chosen τ candidate is required to be negative, selecting opposite signed charges as is expected for the $Z \to \tau\tau$ signal (OS events).

4.2.3 Invariant mass reconstruction

$Z \to \tau\tau \to \ell\tau_h$events are produced with genuine E_T^{miss} typically of the order of 10–20 GeV. In these events, the reconstructed $\tau\tau$ invariant mass using the collinear approximation is a function of E_T^{miss} (see Section 1.2.2).

Therefore, after the lepton and τ-jet energy scales have been determined, the dependence of the invariant mass distribution on E_T^{miss} can be used to determine the E_T^{miss} scale.

For a good reconstruction of the invariant mass, two additional cuts are necessary:

- $E_T^{miss} > 20$ GeV, to select events only in the region where E_T^{miss} is linear (see Section 3.1.2).
- $\Delta\phi(\ell, \tau\text{-jet}) < 2.8$, because the system of the two equations, from the constraint that the momentum sum in the transverse plane is zero, becomes linearly dependent when the decay products are back-to-back.

The distributions of these variables before these cuts are shown in Figure 4.19 for signal and all backgrounds.

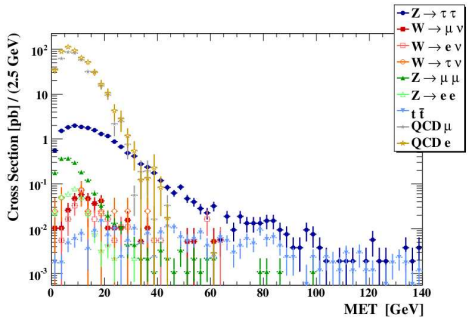

(a)

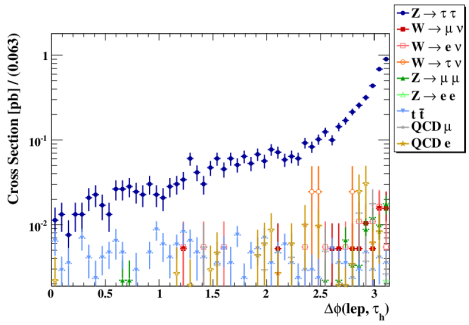

(b)

Figure 4.19: *(a) The distribution of E_T^{miss} for all events passing the selections before the E_T^{miss} cut. (b) The distribution of $\Delta\phi$ between the chosen lepton and chosen tau-jet for all events passing the selections before the cut $\Delta\phi$.*

Nevertheless the invariant mass cannot be reconstructed in all events after the cuts.

Furthermore, the invariant mass is required to be in the range [60,150] GeV.

Results

The accepted cross sections after each step of the selection are given in Figure 4.20 and Table 4.1. With 100 pb^{-1} of data, about 148 OS signal

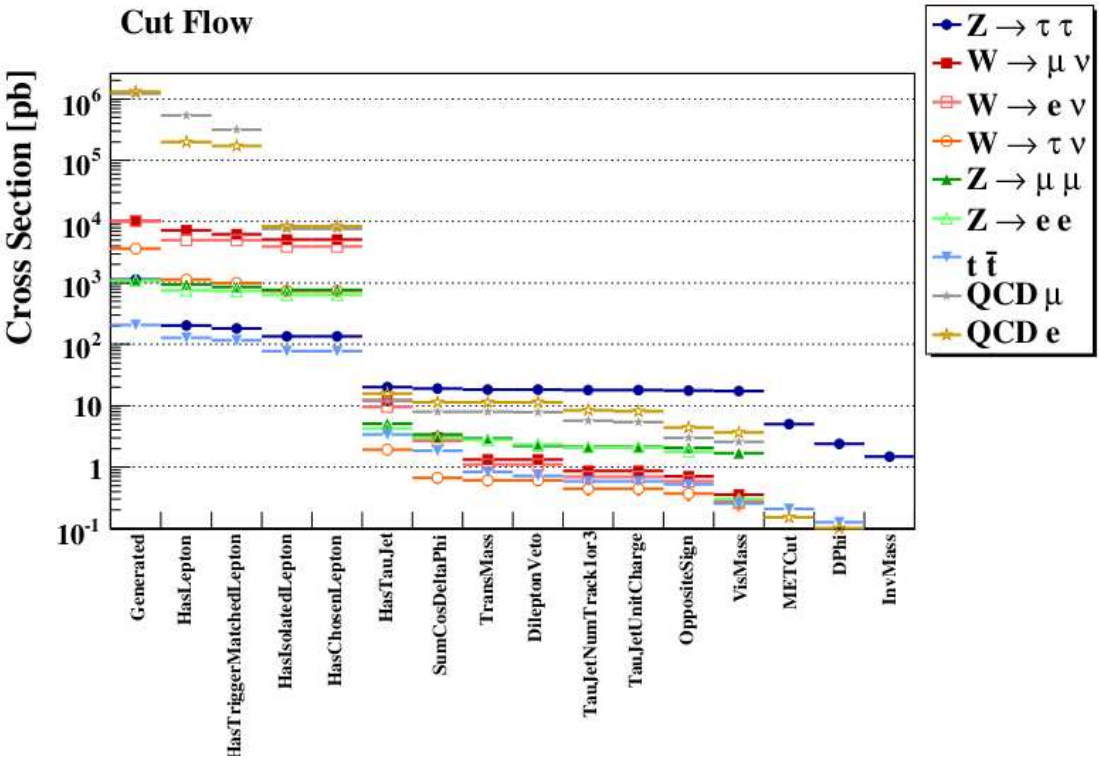

Figure 4.20: *The event selection for the invariant mass analysis.*

events are expected in the invariant mass range 60 GeV $< m_{\tau\tau} <$ 150 GeV, corresponding to an efficiency of 0.13% for the signal process. A total background of 6.1 events ($< 5\%$) is expected from SM channels (QCD excluded).

The QCD background is estimated here from full simulation lepton filtered events and ATLFAST-II events. The results of the two samples are in good agreement and they demonstrate that the QCD background is very well suppressed (6.5 events, corresponding to 4%). Events from $\gamma/Z^* \to ll$ processes contribute negligibly to the invariant mass window.

	$Z \to \tau\tau$	$W \to l\nu$	$Z \to ll$	$t\bar{t}$	QCD Full μ	QCD Full e	QCD AF-II
generated	1128(1)	24370(24)	2196(2)	205.5(4)	1212003(2790)	1302219(2710)	926090000(210000)
has lepton	204.1(6)	13398(16)	1694(2)	129.2(3)	534744(1580)	198137(1230)	815814(5700)
lepton passed trigger	181.6(6)	12188(16)	1613(2)	117.0(3)	313064(1460)	172612(1130)	91700(1110)
lepton passed isol	135.9(5)	9822(14)	1399(2)	77.2(2)	7662(88)	8376(101)	12712(211)
has tau-jet	20.0(2)	23.7(7)	9.4(1)	3.41(5)	12.0(2)	15.8(4)	27.6(9)
$\Sigma \cos \Delta\phi > -0.15$	19.0(2)	6.5(3)	6.4(1)	1.85(4)	7.9(2)	11.4(4)	19.4(7)
$m_{\mathrm{T}} < 50$ GeV	18.5(2)	3.0(3)	5.7(1)	0.83(3)	7.9(2)	11.4(4)	19.4(7)
dilepton veto	18.5(2)	3.0(3)	4.6(1)	0.72(2)	7.8(2)	11.4(4)	19.3(7)
$N_{\mathrm{tracks}}(\tau_{\mathrm{h}}) = 1$ or 3	17.9(2)	2.0(2)	4.2(1)	0.59(2)	5.7(2)	8.4(3)	14.1(7)
$\lvert\mathrm{Charge}(\tau_{\mathrm{h}})\rvert = 1$	17.9(2)	2.0(2)	4.2(1)	0.59(2)	5.5(2)	8.0(3)	13.6(7)
opposite sign	17.8(2)	1.7(2)	3.82(9)	0.53(2)	3.0(1)	4.5(2)	6.5(5)
$m_{\mathrm{vis}} = 25 - 85$ GeV	17.3(2)	0.9(2)	1.99(6)	0.26(1)	2.6(1)	3.7(2)	5.2(5)
$E_T^{miss} > 20$ GeV	5.0(1)	0.23(8)	0.09(1)	0.21(1)	0.08(2)	0.15(3)	0.28(7)
$\Delta\phi(\ell, \tau_{\mathrm{h}}) = 1 - 2.9$	2.40(7)	0.14(7)	0.033(8)	0.13(1)	0.05(1)	0.10(3)	0.14(3)
$m_{\mathrm{inv}} = 60 - 150$ GeV	1.48(5)	0.02(1)	0.007(4)	0.038(6)	0.03(1)	0.04(1)	0.05(1)

Table 4.1: *The invariant mass analysis event selection. The numbers are accepted cross sections in pb. The MC statistical uncertainty on the last digit(s) is shown in parentheses.*

Figure 4.21 shows the reconstructed invariant mass for the $Z \to \tau\tau$ and all the backgrounds after the invariant mass analysis cuts (in OS events) for full simulation QCD samples (top plot) and ATLFAST-II (bottom plot).

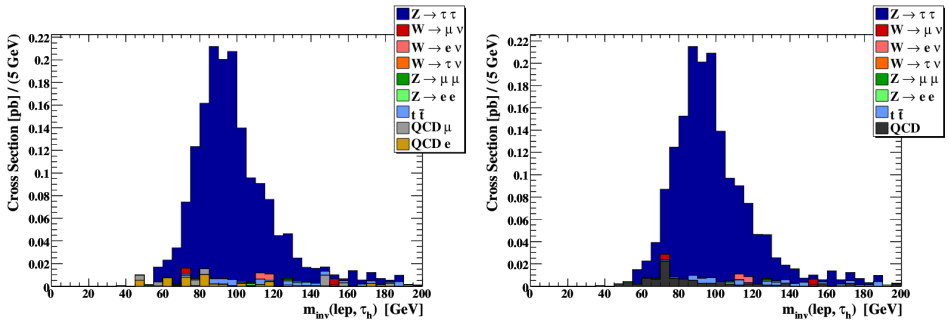

Figure 4.21: *Reconstructed invariant mass of the pair of τ leptons for $Z \to \tau\tau$ decays and all backgrounds . (top) QCD from Full Simulation, (bottom) QCD from ATLFAST-II.*

The total background is extremely small (8% of the signal in total, including QCD).

This is due to the hard cuts applied, moreover, the requirement to have a reconstructed invariant mass is very strong and while it reduces the signal, it suppresses strongly all the backgrounds as well since it can be reconstructed only in a small fraction of the background events.

4.2.4 Reconstructed $\tau\tau$ invariant mass vs E_T^{miss} scale

Because the amount of background at the end of the event selection is small, the invariant mass reconstructed from all the selected OS events can be used for the measurement of the E_T^{miss} scale, without subtracting the background. The reconstructed $\tau\tau$ invariant mass is shown in Figure 4.22(a). The mass peak position value, obtained by a Gaussian fit in the range [65, 115] GeV, is found to be 91.9 $\pm$ 1.4

Figure 4.22(b) shows that the peak position of the measured Z mass reconstructed from τ-pairs has a very good sensitivity to the absolute E_T^{miss} scale. This figure is obtained using OS events for signal and background (QCD included). Each point is obtained reconstructing the invariant $\tau\tau$ mass after applying a correction factor to the E_T^{miss} energy scale, and fitting the peak value with a Gaussian shape in the range [65, 115] GeV. The error bars account for the statistical errors of the fitted peak values, and are correlated for all points.

The systematics that can affect the mass peak position are:

- The addition of background: it has been checked that the mass peak position obtained using only OS signal events is 91.8 ± 1.4 GeV ($\sim 1‰$ different from signal plus background result).
- The stability of the fit: the fit range [65,115] GeV has been shifted of 2% to lower and higher mass regions with no difference in the fitted peak values. The fit range has also been widened to [60,120] GeV resulting in a fitted peak value of $91.5\pm$ 1.4 GeV ($\sim 4‰$ different from standar range result).
- The error on the MC prediction of the nominal Z mass value is found negligible.

Therefore the systematics errors on the mass peak value are negligible compared to the statistical one of 1.5%. This error reflects on the E_T^{miss} scale determination that with 100 pb^{-1} of data at 10 TeV it can be obtained with a precision of $\sim 6\%$. This method has still to be tested on 7 TeV Monte Carlo events. Since the precision is limited only by the statistics, it can surely be improved using more data. To understand the integrated luminosity needed for this analysis it will be necessary to evaluate the eventual mass distribution distortion due to pileup.

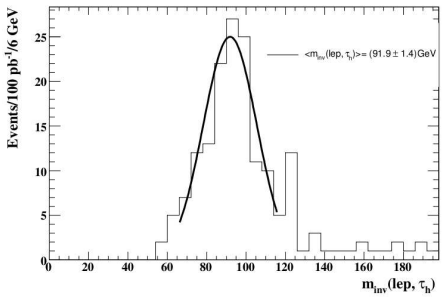

(a)

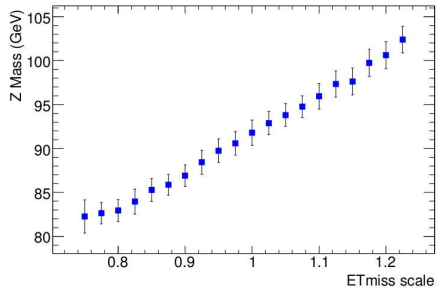

(b)

Figure 4.22: *Distributions for OS events for signal and SM samples summed up (QCD included). The results were obtained using the statistics as expected in 100 pb^{-1} for all the samples with the exception of QCD for which we used the available statistics (* 1.5 *million events for full simulated events and* $\sim$ 130 *million events for ATLFAST-II events). (a) The reconstructed invariant mass distribution in 100 pb^{-1}. (b) Reconstructed invariant mass of the pair of* τ *leptons for* $Z \rightarrow \tau\tau$ *decays as a function of the* E_T^{miss} *for signal and SM events: proportionality is evident. All points are obtained by the same sample of events, therefore errors, that are statistical only, are correlated.*

Chapter 5

Conclusions

In experimental physics at hadronic colliders an accurate measurement of the missing transverse energy is crucial for the study of many physics channel in the contest of the Standard Model and beyond.

In this thesis the first measurement of E_T^{miss} in ATLAS with real data has been presented. Events both at a center-of-mass energy of 900 GeV and at 7 TeV have been studied.

In 900 GeV data the performance of the reconstruction algorithm for the E_T^{miss} has been tested in minimum bias events at the electromagnetic scale, and it has been found a good agreement with the expectation from Monte Carlo simulation.

With 7 TeV data minimum bias and di-jets events have been studied and E_T^{miss} performance has been tested using different calibrations algorithms, from the most simple to the most refined one, confirming the good agreement between data and simulation found at the EM scale.

At both energies the few events in the tail of the E_T^{miss} distribution in data are well understood.

In particular a detailed study of different E_T^{miss} calibration configurations has been performed to find the best calibration to be applied to the different objects entering in E_T^{miss} calculation as well as to cells outside objects. The best calibration scheme found is based on the Local Hadronic calibration with the addition of a Jet Energy Scale correction for the jets and a calibration using reconstructed tracks (called Eflow) for cells outside physics object, while for leptons the proper calibration is applied.

A dedicated study has also been devoted to understand the $\sum E_T$ data-simulation disagreement and the ϕ distribution of E_T^{miss}.

The effect due to the pileup has also been studied and it results in larger E_x^{miss} and E_y^{miss} distributions.

A preliminary study on the determination of E_T^{miss} scale from $W \rightarrow l\nu$ data and Monte Carlo events has been presented, resulting in a precision of 3%, statistical only, in the E_T^{miss} scale determination with the data used for this thesis.

A more complete and detailed 10 TeV Monte Carlo based study on the method to determine the E_T^{miss} scale from $Z \rightarrow \tau\tau$ events, that can be used with an integrated luminosity of at least 100 pb^{-1} obtaing a precision of $\sim$ 6%, has also been described. This measurement is weakly affected by systematics, and can then be improved with statistics.

Acknowledgements

The work described in this thesis would not have been possible without the help and support of many people I am grateful to.

First I want to thank Donatella for all the time she has dedicated to me, for everything she has taught me and for her immense love for her work that she trasmits to everyone and that fascinates so much young people like her students. I am proud to have been one of them.

Then I am very grateful to Silvia, not only for her precious help and patience, and for teaching me all Etmiss details many many times, but also for the friendship and the company she has kept for me in these years.

I want to thank Peter Loch for having read, corrected and commented this thesis word by word, and because he accepted to come from Arizona to attend my defense. Many thanks also to have given to me the opportunity to go to Tucson!

Thanks to Leonardo for giving me his useful scripts for free (I know I promised to find some undergrad students for you... I am still looking for them!) and for being so earnest in his work and his life.

Many thanks also to Laura, Adele and Sandra that agreed on being members of the final exam committee despite the troubles this causes to all of them.

I would also like to thank Chiara and all Milano ATLAS group, in particular I want to thank Lidia, with whom I have shared joys and sorrows of this university adventure, Ilaria, Andrea, Rosa and finally Sofia, who deserves a special thank for having read and corrected 2 chapters of this thesis.

Thanks also to my non-Milano-living friends: Stan and Betty and Susanne from Freiburg whose friendship is a great present that the ATLAS tau group has given me, and finally Will, my second (australian) young brother, thanks for everything.

I want now to thank my parents, my brother, my sister and all my friends that have come along with me in these years and that help me to look at

what I have in front of me.

Finally I could not be what I am without my family: Michele, Lucia and the new-coming baby Agnese. Thanks because you make clear the meaning of such a hard job.

Bibliography

[1] A. Grau, G. Pancheri, Y.N. Srivastava, *Hadronic Total Cross-sections Through Soft Gluon Summation in Impact Parameter Space* , Phys.Rev. D60 (1999) 114020.

[2] A. Moraes, C. Buttar and I. Dawson. *Prediction for minimum bias and the underlying event at LHC energies*, European Physics Journal C, 50 (2007) 435.

[3] C. Giunti, C. W. Kim, *Fundamentals of Neutrino Physics and Astrophysics*, Oxford University Press, Oxford, UK, 2007.

[4] D0 Collaboration, Conference Note 5893-CONF, 2009.

[5] The ATLAS Collaboration, *Measurement of the* $W \to l\nu$ *and* $Z/\gamma* \to ll$ *production cross sections in proton-proton collisions at* $\sqrt{s} = 7$ *TeV with the ATLAS detector*, CERN-PH-EP-2010-037.

[6] The ATLAS Collaboration, *Observation of top quark pair production in ATLAS at* $\sqrt{s} = 7$ *TeV*, in preparation.

[7] G. Altarelli *Status of the Standard Model and Beyond* Nucl.Instrum.Meth.A518:1-8 (2004).

[8] R. Barate *et al.* [LEP Working Group for Higgs boson searches and ALEPH Collaboration and and], *Search for the standard model Higgs boson at LEP*, Phys. Lett. B **565** (2003) 61 [arXiv:hep-ex/0306033].

[9] K. Nakamura et al. (Particle Data Group), J. Phys. G 37, 075021 (2010).

[10] A. Dedes, S. Heinemeyer, S. Su, G. Weiglein, *The lightest Higgs boson of mSUGRA, mGMSB and mAMSB at present and future colliders:*

observability and precision analyses. Nuclear Physics B 674: 271-305 (2003).

[11] The ATLAS Collaboration, *Expected Performance of the ATLAS Experiment - Detector, Trigger and Physics*, arXiv:0901.0512 [hep-ex].

[12] The ATLAS Collaboration, *ATLAS Detector and Physics Performance Technical Design Report*, CERN/LHCC/99-14 and CERN/LHCC/99-15, 1999.

[13] M. S. Carena, S. Heinemeyer, C. E. M. Wagner and G. Weiglein, Eur. Phys. J. 26 (2003) 601.

[14] D. Cavalli and G. Negri, *Extension of the Study of A/H to tau-tau to lepton-hadron in the high mA region*, ATL-PHYS-2003-009.

[15] J. Thomas, *Study of heavy MSSM-Higgs bosons A/H in hadronic tau-decays in ATLAS*, ATL-PHYS-2003-003.

[16] The ATLAS collaboration, *Discovery Potential of* $A/H \to \tau^+\tau^- \to lh$ *in ATLAS*, ATL-PHYS-PUB-2010-011.

[17] J. Campbell *et al.*,*Hard interactions of quarks and gluons: a primer for LHC physics*, Reports on Progress in Physics, arXiv:hep-ph/0611148, 2007.

[18] L. Evans and P. Bryant, *LHC Machine*, JINST **3** (2008) S08001.

[19] The ATLAS Collaboration, *The ATLAS Experiment at the CERN Large Hadron Collider*, JINST **3** (2008) S08003.

[20] The ATLAS Collaboration, *The ATLAS Inner Detector commissioning and calibration*, arXiv:1004.5293.

[21] The ATLAS Collaboration, *Readiness of the ATLAS Liquid Argon Calorimeter for LHC Collisions*, arXiv:0912.2642.

[22] The ATLAS Collaboration, *Readiness of the ATLAS Tile Calorimeter for LHC collisions*, ATLAS-TCAL-2010-01-006; CERN-PH-EP-2010-024.

[23] The ATLAS Collaboration, *Commissioning of the ATLAS Muon Spectrometer with Cosmic Rays*, arXiv:1006.4384 ; ATLAS-MUON-2010-01-006. - 2010.

[24] The ATLAS Collaboration, *Charged particle multiplicities in pp interactions for track* p_T¿ *100 MeV at* $\sqrt{s}$= *0.9 and 7 TeV measured with the ATLAS detector at the LHC*, ATLAS-CONF-2010-046.

[25] The ATLAS Collaboration, *Luminosity Determination Using the ATLAS Detector*, ATLAS-CONF-2010-060.

[26] ATLAS Luminosity and Run Statistics Plots for 2010 Beam Data, https://twiki.cern.ch/twiki/bin/view/Atlas/RunStatsPublicResults2010

[27] The ATLAS Collaboration, *Properties of tracks in jets observed in proton-proton collisions at* $\sqrt{s} = 7$ *TeV in the ATLAS detector*, ATLAS-CONF-2010-061.

[28] T. Cornelissen, M. Elsing, I. Gavrilenko, W. Liebig, E. Moyse and A. Salzburger, *The New Atlas Track Reconstruction (Newt)*, J. Phys. Conf. Ser. **119** (2008) 032014.

[29] The ATLAS Collaboration, *Performance of primary vertex reconstruction in proton-proton collisions at* $\sqrt{s} = 7$ *TeV in the ATLAS experiment*, ATLAS-CONF-2010-069.

[30] The ATLAS Collaboration, *Observation of prompt inclusive electrons in the ATLAS experiment at* $\sqrt{(}s) = 7$ *TeV*, ATLAS-COM-CONF-2010-074.

[31] W. Lampl *et al. Calorimeter Clustering Algorithms : Description and Performance*, ATL-LARG-PUB-2008-002.

[32] D. Banfi, L. Carminati, L. Mandelli, *Calibration of the ATLAS electromagnetic calorimeter using calibration hits*, ATL-LARG-PUB-2007-012.

[33] D.Banfi *et al.*, *The determination of the energy of electrons and photons in the ATLAS electromagnetic calorimeters*, ATL-PHYS-INT-2010-038.

[34] N. Kerschen *et al.*, *Plots for Electron performance of the ATLAS detector using the* $J/\Psi \to e^+e^-$ *decays*, ATL-PHYS-2010-518.

[35] M. Donega and L. Serin,*Calibrated* $Z \to e^+e^-$ *invariant mass*, ATL-PHYS-2010-734.

[36] S. Hassani, L. Chevalier, E. Lancon, J. F. Laporte, R. Nicolaidou and A. Ouraou, *A muon identification and combined reconstruction procedure for the ATLAS detector at the LHC using the (MUONBOY, STACO, MuTag) reconstruction packages*, Nucl. Instrum. Meth. A **572** (2007) 77.

[37] T. Lagouri *et al.*, *A muon identification and combined reconstruction procedure for the ATLAS detector at the LHC at CERN*, IEEE Trans. Nucl. Sci. **51** (2004) 3030.

[38] ATLAS Muon combined performance public plots, https://twiki.cern.ch/twiki/bin/view/Atlas/MuonPerformancePublicPlots

[39] The ATLAS Collaboration, *Muon Performance in Minimum Bias pp Collision Data at* $\sqrt{s}$ *= 7 TeV with ATLAS*, ATLAS-CONF-2010-036.

[40] The ATLAS Collaboration, *Muon Reconstruction Performance*, ATLAS-CONF-2010-064.

[41] G.C. Blazey *et al.*, *Run II jet physics*, hep-ex/0005012.

[42] S. Catani, Y. L. Dokshitzer, M. H. Seymour and B. R. Webber, *Longitudinally invariant K(t) clustering algorithms for hadron hadron collisions*, Nucl. Phys. B 406 (1993) 187
S.D. Ellis and D.E. Soper, *Successive combination jet algorithm for hadron collisions*, Phys. Rev. D 48 (1993) 3160 [hep-ph/9305266].

[43] Y.L. Dokshitzer, G.D. Leder, S. Moretti and B.R. Webber, *Better jet clustering algorithms*, JHEP 08 (1997) 001 [hep-ph/9707323];
M. Wobisch and T. Wengler, *Hadronization corrections to jet cross sections in deep-inelastic scattering*, hep-ph/9907280.

[44] M. Cacciari, G. P. Salam and G. Soyez, *The anti-kt jet clustering algorithm*, JHEP **0804** (2008) 063 [arXiv:0802.1189 [hep-ph]].

[45] The ATLAS Collaboration, *Properties of Jets and Inputs to Jet Reconstruction and Calibration with the ATLAS Detector Using Proton-Proton Collisions at* $\sqrt{s}$ *= 7 TeV*, ATLAS-CONF-2010-055.

[46] The ATLAS Collaboration, *Reconstruction of hadronic tau candidates in QCD events at ATLAS with 7 TeV proton-proton collisions*, ATLAS-CONF-2010-061.

[47] The ATLAS Collaboration, *Commissioning of the ATLAS Tau-Lepton Reconstruction Using 7 TeV data*, ATL-PHYS-2010-392.

[48] ATLAS Collaboration, *Data-Quality Requirements and Event Cleaning for Jets and Missing Transverse Energy Reconstruction with the ATLAS Detector in Proton-Proton Collisions at a Center of Mass Energy* $\sqrt{s}$ *=* 7 *TeV*, ATLAS conference note.

[49] T. Sjostrand, S. Mrenna and P. Z. Skands, *PYTHIA 6.4 Physics and Manual*, JHEP **0605** (2006) 026 [arXiv:hep-ph/0603175].

[50] S. Agostinelli *et al.* [GEANT4 Collaboration], *GEANT4: A simulation toolkit*, Nucl. Instrum. Meth. A **506** (2003) 250.

[51] The ATLAS Collaboration, *Measurement of the missing transverse momentum based on tracks in proton-proton collisions at* $\sqrt{s} = 900$ *GeV centre-of-mass energy with the ATLAS detector*, ATLAS-CONF-2010-020.

[52] The ATLAS Collaboration, *Performance of the missing transverse energy reconstruction in proton-proton collisions at center-of-mass energy of* $\sqrt{s} = 7$ *TeV with the ATLAS detector*, ATLAS-CONF-2010-039.

[53] The ATLAS Collaboration, *Performance of the Missing Transverse Energy Reconstruction and Calibration in Proton-Proton Collisions at a Center-of-Mass Energy of 7 TeV with the ATLAS Detector*, ATLAS-CONF-2010-057.

[54] The ATLAS Collaboration, *Jet energy scale and its systematic uncertainty for jets produced in proton-proton collisions at* $\sqrt{s} = 7$ *TeV and measured with the ATLAS detector*, ATLAS-CONF-2010-056.

[55] M. Antonelli, M.Testa, *An energy-flow algorithm for the reconstruction and calibration of the low-*p_T *contribution to* E_T^{miss}, ATL-COM-PHYS-2010-184.

[56] The ATLAS Collaboration, *ATLAS Monte Carlo tunes for MC09*, ATL-PHYS-PUB-2010-002.

[57] S. Frixione and B. R. Webber, *The MC@NLO Event Generator*, arXiv:hep-ph/0207182, 2002.

[58] K. Assamagan *et al.*, *The ATLAS Monte Carlo Project*, ATL-COM-SOFT-2008-024.

[59] A. Kalinowski and K. Benslama, *Tau identification with the logarithmic likelihood method*, ATL-PHYS-INT-2008-037.

[60] Z. Czyczula and M. Dam, *Cut-based electron veto algorithm for the track-seeded part of tauRec*, ATL-PHYS-2009-023.

[61] P. Betchle *et al*, *Benchmark Analysis for Z to tau tau to lepton hadron with the First 100 pbâ1* , ATL-PHYS-INT-2010-075.